Few Layers of Graphene and Carbon Nanoscrolls by Wedge Based Mechanical Exfoliation

R.A.P.B.Jayasena

SCHOOL OF MECHANICAL AND AEROSPACE ENGINEERING

A thesis submitted to the Nanyang Technological University
in fulfillment of the requirements for the degree of
Doctor of Philosophy

2014

Acknowledgments

First and foremost, I would like to acknowledge the help and support I received from Prof. Sathyan Subbiah, my PhD supervisor, without whom this thesis wouldn't have been possible. His continuous support, useful discussions and guidance provided me the confidence to delve deep into my research problem. He is one of the best teachers I ever met and I must say I am very lucky to meet such a friendly, understanding, and humble person in my life. Next, I would like to convey my sincere gratitude to my co-supervisor Dr. Chilla Damodara Reddy-Institute of High Performance Computing, who accepted me as one of his students and provided extensive support.

Many thanks to the NTU research scholarship for financially supporting me during the course of my study.

I would like to thank Professor Murukeshan Vadakke Matham for his support during the teaching assignment and all other NTU faculty members who helped me during various stages of my studies.

I am also grateful to Professor Shiv G. Kapoor and Professor Gehan Amaratunga for having useful discussions during my PhD candidature.

I cannot forget the help and support I received from all lab technicians from the Materials Lab 1 and the Precision Engineering Lab at the School of Mechanical and Aerospace Engineering and the FACTS lab at the school of Materials that provided

tremendous support in many ways.

I must acknowledge the tremendous help and support I received from my dearest friends, Kumudu, Dr.Chatura, Dr. Chandana, Dr.Diluka, Namal, Dr. Gamini, Dr. Shinoj, Dr. Kush, Dr.Hammed and all my lab mates. Without them, my continuation this work would have been difficult.

Finally, I would like to thank my dearest parents, my wife Erandi, my sister Jeevani and all other family members for their love and support through the years; nothing would have been possible without them.

Abstract

Two-dimensional flat carbon sheets, commonly seen in graphite, are a much sought after material with interesting electronic and mechanical characteristics. It is expected to be used in the next generation microchips in lieu of silicon and also expected to first enter the commercial market in the form of conducting plastics and composites. Due to the increase in the number of such applications along with business opportunities, producing or isolating this layer of graphite cost-effectively is an urgent challenge to be addressed. Widespread efforts in this direction are focusing more on chemical methods to separate (from bulk graphite) or deposit (using epitaxial methods) this two-dimensional layer; such chemical methods not only are environmentally unfriendly, but also produce poor yield and can result in graphene layers with undesirable functional groups attached. One of the early methods, and still sometimes used today for research, of separating graphene from bulk graphite is by mechanical cleavage using a scotch tape. This method is known to produce high quality of graphene layers. However, this method is not reliable for mass manufacturing of graphene; the full potential for such mechanical methods remain to be explored.

In this study, a novel method to synthesize carbon nano-sheets specially few layers of graphene from bulk graphite by mechanical exfoliation is presented. The method involves the use of an ultra-sharp single crystal diamond wedge to cleave highly or-

dered pyrolytic graphite parallel to the basal plane to generate carbon nanosheets. Characterization of the cleaved layers shows that the process is able to synthesize carbon nano-sheets with a thickness of a few nanometers and with an area of hundreds of micrometers. Further examination of sheets made by such sectioning showed the presence of flat, rolled and sheared graphitic thin layers with nano-scale dimensions. The rolled structures observed are of various types: partially rolled, fully rolled and axially slid out nano-scrolls. In addition, two types of kink bands are also observed in the sectioned layers. Microscopic analysis of the as received starting material (prior to sectioning) showed the presence of defects such as discontinuous layers, kink bands and edge folds. The sectioning forces are measured and used to correlate with the structural characteristics of the layers. The possibility of enhancing the cleaving process by the use of ultrasonic oscillations along the wedge is also studied. In order to understand the wedge-graphene interactions under controlled conditions this thesis investigates the micro-nano indentation of highly oriented pyrolytic graphite parallel to the basal plane. Such indentation allows control over the depth and load leading to an understanding of the various stages of layer separation and edge structure formation. Depending on how far we indent from a free edge various types of load-displacement curves have been observed. Interesting kinks/steps are also observed during unloading stage signifying structural changes.

The thesis explores, using molecular simulations, how and under what conditions graphene layers separate, fold and shear during the wedge-based mechanical exfoliation machining technique. Molecular simulations of initial wedge engagement show that the entry location of the wedge tip vis-a-vis the nearest graphene layer plays a key role in determining whether layers separate or fold and which layers and how many of them fold. It is also noticed that depending on this entry location several successive layers beneath the wedge undergo significant elastic bending, consuming

energies requiring large vertical forces to be imposed by the moving wedge. The layer separation force itself is seen to be minimal and consistent with breaking up of van der Waals interactions. In addition, shearing of layers occurs mainly during wedge exit and depends largely on the wedge speed and also its depth of insertion. Understanding the conditions at which this separation, folding and shearing of the graphene layers takes place, one can control or tune the wedge-based exfoliation technique for particular kinds of graphene layers. Molecular simulations also show that the multiple spikes in sectioning forces observed in experiments could be explained as the interactions of discontinuous layer pre-existing in the starting material with the moving wedge. The effect of wedge radius on initial wedge material engagement reveals various layer initiation modes in relation to the depth of insertion. The obtained forces significantly increase with an increase in the wedge radius.

Molecular simulations are further used to understand the formation of carbon nanoscrolls and the study presents two hypotheses of how such scrolls form. The first hypothesis is based on microscopic evidence of pre-existing folds in layer edges of the HOPG. The moving wedge upon interaction with certain fold geometries can trigger scroll formation. The second hypothesis is based on literature evidence that graphene sheets when subject to deformation can result in defects on the torn edges and such defects are induced in the HOPG layers during sample preparation. The layers with such defects, upon interacting with the moving wedge, can also form scrolls.

This thesis, by a combination of experimental and simulation studies, convincingly shows the capability of producing both planar and rolled carbon nano structures with the wedge-based mechanical exfoliation technique. Understanding of this oriented sectioning technique provides useful control methods employing which this technique has potential to be used as a technique to fabricate thin graphitic layers and rolled

structures for potential industrial applications.

List of Acronyms

AFM	Atomic Force Microscope
AIREBO	Adaptive Intermolecular Reactive Empirical Bond Order
BFS	Bottom Fixed System
CNT	Carbon NanoTube
CNS	Carbon NanoSCrolls
DOI/R	Depth of Insersion to Wedge Radius Ratio
fs	Femto-second
FES	Fixed End System
FESEM	Field Emission Scanning Microscope
HOPG	Highly Ordered Pyrolytic Graphite
LAMMPS	Highly Ordered Pyrolytic Graphite
MD	Molecular Simulations
ps	Pico-second
TEM	Transmisson Electron Microscope
WBME	Wedge Based Mechanical Exfoliation

Contents

Acknowledgements **i**

Abstract **iii**

List of Acronyms **vii**

Contents **viii**

List of Figures **xii**

List of Tables **xviii**

1 INTRODUCTION **1**

1.1 Background and Motivation 1

1.2 Alternative Mechanical Cleaving Method 7

1.3 Objectives and Scope of the Thesis 8

1.4 Research Approach and Thesis Outline 9

2 LITERATURE REVIEW **10**

2.1 Carbon Nanosheet Structure and Its Variations 11

2.2 Carbon Nanosheet Fabrication Techniques 14

2.2.1 Epitaxial Growth 15

2.2.2 Unconventional Methods 16

2.3 Exfoliation Techniques 21

2.3.1 Chemical Exfoliation 21

2.3.2 Thermal Exfoliation Methods 23

2.3.3 Mechanical Exfoliation 24

2.4 Mechanical Cleaving Using a Cutting Tool 26

2.4.1 Mechanical Machining 27

2.4.2 Microtome Sectioning 30

2.5 Graphene Processing Methods 35

2.6 Molecular Simulations 36

2.7 Summary 39

3 WEDGE BASED MECHANICAL EXFOLIATION (WBME) 41

3.1 WBME Technique 42

3.2 Material Preparation 42

3.3 Preliminary Cleaving Results 48

3.4 Detailed Characterization of Carbon Nanosheets 55

3.4.1 Qualitative Analysis of Sectioned Layers with Optical Microscope, FESEM and TEM 59

3.5 Sectioning Force Signature 66

3.6 Summary 67

4 FACTORS AFFECTING WBME - A MOLECULAR SIMULATION STUDY 69

4.1 Background 69

4.2 Simulation Model 70

4.3 Separation, Folding and Shearing of Graphene Layers 76

4.3.1 Layer Separation 76

4.3.2 Layer Folding 77

4.3.3 Layer Shearing 82

4.4 Correlation of Structural Defects and Intermittent Force Spikes . . . 85

4.5 Effect of the Larger Wedge Radius 87

4.6 Effect of Ultrasonic Vibration 99

4.7 Summary 102

5 FORMATION OF CARBON NANOSCROLLS 105

5.1 Background of Carbon Nanoscrolls 106

5.2 Experimental Observations of Scroll Formation 109

5.3 Summary 123

6 INDENTATION OF HOPG PARALLEL TO BASAL PLANE 124

6.1 Motivation 125

6.2 Experimental Setup 128

6.3 Results and Discussion 129

6.3.1 Raman Observations 137

6.4 Summary 140

7 CONCLUSION AND FUTURE WORK 141

7.1 Main Conclusions 141

7.2 Future Work 147

Publications 150

Appendix 153

Bibliography 156

Vita 173

List of Figures

1.1 Carbon nanostructures 2

1.2 Future graphene road map 3

1.3 Comparison of price and quality of current manufacturing methods . 6

1.4 The scotch-tape method 7

1.5 The research road map 9

2.1 Crystalline arrangement under high temperature processing 12

2.2 Graphene structure 13

2.3 Stacking modes of AA, AB and ABC on multilayer graphene 13

2.4 Carbon nanosheet variations 14

2.5 Carbon nanostructures and current graphene manufacturing methods 15

2.6 Epitaxial growth of graphene 16

2.7 Graphene nanoribbons from unzipping multi-wall carbon nanotube . 17

2.8 Unzipping carbon nanotube with palladium particles 18

2.9 A schematic diagram of gradual unzipping of one wall of a CNT to form a nanoribbon 19

2.10 Unzipping multi-wall carbon nanotube with Li catalist 19

2.11 Colloidal suspension process to produce graphene 22

2.12 Schematic diagram for graphite intercalation and exfoliation 23

2.13 Thermal exfoliation process 24

2.14 Mechanical exfoliation methods 25

2.15 Orthogonal cutting process 28

2.16 Ultramicrotome and cutting operation 31

2.17 Ultra-sharp diamond wedge 32

2.18 Chemical approach of graphene transferring 35

2.19 Roller assisted graphene transferring 36

3.1 The schematic diagram of the WBME 42

3.2 Concept converts to a experimental set-up 43

3.3 Material preparation 44

3.4 Specimen trimming process 45

3.5 Experimental set-up 46

3.6 Alignment process of wedge and the specimen 47

3.7 Layer separation process 49

3.8 Optical microscope images of preliminary layers 50

3.9 Thickness measurement with AFM 50

3.10 TEM images without ultrasonic oscillation 52

3.11 TEM images with ultrasonic oscillation 52

3.12 Raman spectroscopy data 53

3.13 Calculation of *La* using experimentally obtained values 55

3.14 Pre-existing defects in HOPG prior to sectioning 57

3.15 The experimental setup for force measurement 58

3.16 Optical microscope images of thin section layer morphologies 59

3.17 Optical microscope images of thick sections 61

3.18 FESEM images of sectioned layers 62

3.19 TEM Images of sectioned layer morphologies 64

3.20 The specimen surface of HOPG after sectioning 65

3.21 Sectioning and normal force trends with time 66

4.1 Wedge based mechanical exfoliation of few layers of graphene 71

4.2 Graphene unit cell and atom positions 71

4.3 Model single layer graphene sheet 72

4.4 Simulation model 73

4.5 Conditions at which layer separation was seen in simulations 77

4.6 Folding of layers ahead of the wedge edge at various depths of indentations 78

4.7 Deflection of the immediate layer below the wedge with respect to the wedge position 79

4.8 Forces acting on the wedge during the cleaving process for various wedge positions 80

4.9 Shearing of graphene layers as the wedge exits 82

4.10 Forces acting on the wedge extracted from the BFS model simulations 84

4.11 Molecular dynamics simulation model and results 86

4.12 Investigation of critical value of DOI with respect to wedge radius . . 89

4.13 Variation of $DOI_{critical}$ and the size of buckling 90

4.14 Effect of wedge radius on layer initiation at various DOI 91

4.15 Cleaved layer behavior after significant penetration inside the material 92

4.16 The cleaving and vertical forces acting on the wedge 93

4.17 Wedge-material engagement 94

4.18 Forces profiles under larger wedge radius 96

4.19 Force variation with wedge radius 97

4.20 Cutting energy variation 99

4.21 Oscillating wedge material system 100

4.22 Wedge-material engagement with ultrasonic vibration 101

4.23 Forces profiles under ultrasonic vibration 102

5.1 Experimental set-up of wedge based mechanical exfoliation 108

5.2 Experimentally observed nanoscrolls formation in layers synthesized using wedge-based mechanical exfoliation 109

5.3 Investigation of scroll formation with various factors 112

5.4 Hypotheses for scroll formation 113

5.5 Molecular layered structure with pre-existing initial scroll and a rigid wedge 114

5.6 Effect of the initial fold 116

5.7 Effect of wedge position on scroll formation 117

5.8 Graphene sheets with defect edge structures 118

5.9 Variation of potential energy and development of scroll formation after inducing 5-6 defects 119

5.10 Effect of 5-6 type of defects during the exfoliation process 120

5.11 Comparison of cleaving force 121

5.12 Comparison of without (pre-defined) and with defect scrolling 122

6.1 Wedge based mechanical exfoliation vs Indentation 125

6.2 Comparison of machining and indentation 126

6.3 Indented positions on the HOPG surface parallel to the basal plane . 128

6.4 Micro indentation parallel to the basal plane with a micro hardness tester 130

6.5 Load vs Displacement profiles 132

6.6 Indentation Marks on the surface signifies the depth control 133

6.7 Load vs. Displacement curves at various loading conditions 134

6.8 Indentation marks on the surface under load control 136

6.9 Effects of the heavy indentation 137

6.10 Load vs displacement with multiple indents 138

6.11 Raman peaks under indenter positions 139

7.1 Preparation of micro-pillar specimen 148

List of Tables

2.1 Summary of the gaps identified prior reported other mechanical exfoliation and sectioning techniques 33

3.1 Comparison of I_D/I_G ratios of of CVD, scotch and WBME graphene . 54

4.1 Young's modulus value of graphene reported in the literature 73

4.2 MD simulation model parameters 75

4.3 Factors affecting the nature of the exfoliation-though molecular simulations 103

4.4 Summary of the parameter and model results validation 104

5.1 Effects of various factors on scroll formation 111

7.1 Factors affecting the nature of the exfoliation-though molecular simulations 146

7.2 Effects of various factors on scroll formation 146

Chapter 1

INTRODUCTION

1.1 Background and Motivation

The discovery of different forms of carbon structures such as fullerene, nanotubes, and graphene (fig.1.1 [1]) have led to increases in research and development of carbon based materials science. Graphene is the most recent addition to this group. Graphene is a two dimensional sp^2-bonded layer of atoms arranged in a honeycomb lattice. The two-dimensional layer serves as the basic building block of all other graphitic forms. From physicists interested in studying its properties to materials and electronics engineers eager to use of it to make novel devices and materials, it is a much sought-after substance both in the academic world and in the industry. Once thought not to exist by themselves these 2-D carbon sheets were discovered in 2004 [2], causing earlier theories of thermodynamic equilibrium of 2-D crystals to be revised [3]. Graphene, like other carbon nanostructures, is equally vital for a wide range of applications.

Graphene displays remarkable properties that are useful in many applications. These include exceptional quantum hall effects [4], high electron mobility at room temper-

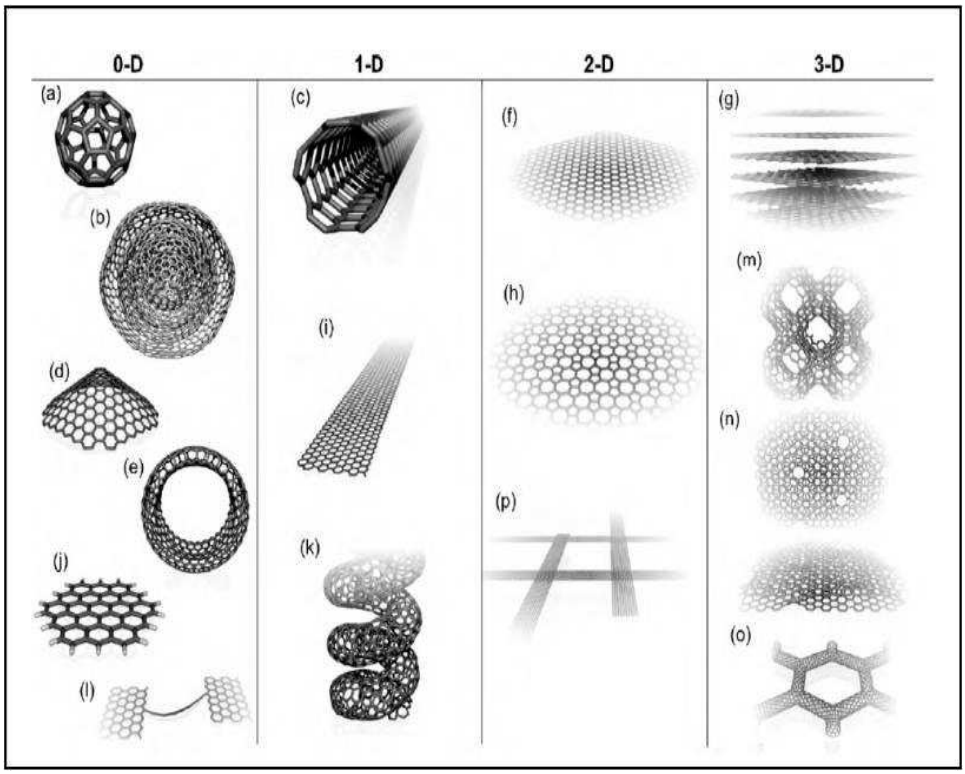

Figure 1.1: Carbon nanostructures; (a) C_{60}: Buckminsterfullerene; (b) nested giant fullerenes or graphitic onions; (c) carbon nanotube; (d) nanocones or nanohorns; (e) nanotoroids; (f) graphene surface; (g) 3D graphite crystal; (h) Haeckelite surface; (i) graphene nanoribbons; (j) graphene clusters; (k) helicoidal carbon nanotube; (l) short carbon chains; (m) 3D Schwarzite crystals; (n) carbon nanofoams (interconnected graphene surfaces with channels); (o) 3D nanotube networks, and (p) nanoribbons 2D networks[1].

ature of 2.5x10^5 cm^{2}V^{-1}s^{-1}, large Young's modulus of 1 TPa, high thermal conductivity above 3,000 WmK^{-1}, optical absorption of 2.3%, ability to conduct high densities of electric current, and the ability of decorating with other molecules (chemically functionality).

The electrical properties of graphene trigger many applications in transparent conductive coatings such as touch screen, e-paper, organic light-emitting diodes (OLEDs), high frequency transistors, and logic transistors (which have tremendous potential to replace silicon). A number of potential photonic applications show its great potential - photodetectors, optical modulators, turntable fiber and solid-state mode locked

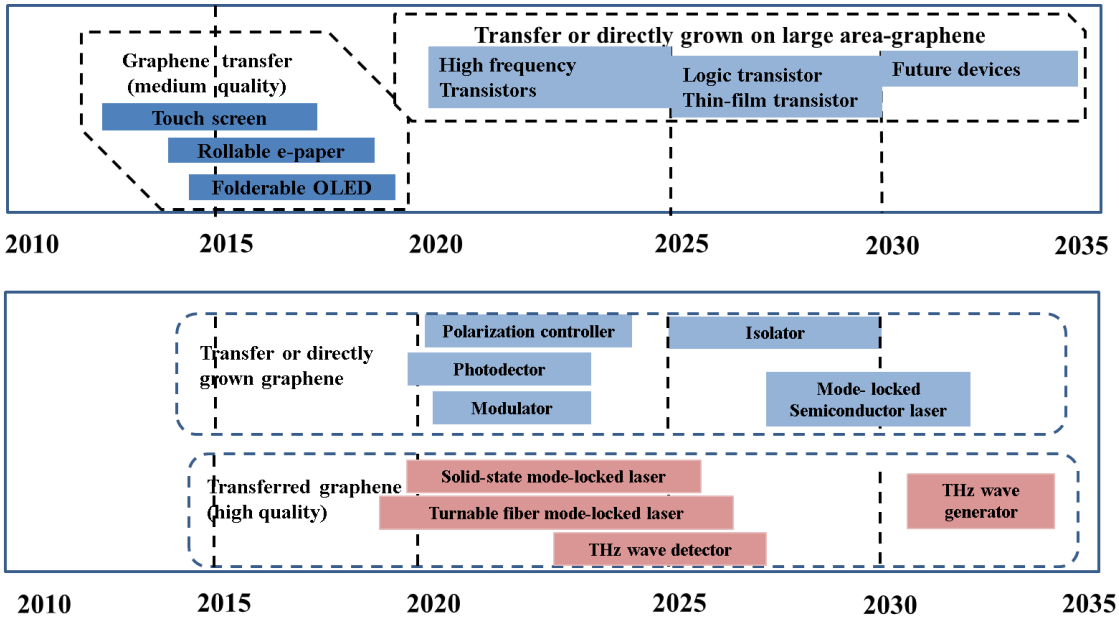

Figure 1.2: Future graphene road map [6]

lasers, and optical polarization controllers. Graphene-based paints are widely used as conductive ink and gas barrier applications. Graphene-attached composite materials have also been developed for a wide range of applications. Graphene research is increasingly targeting energy-storing applications such as solar cells, electrode materials, super capacitors, batteries and fuel cells. Extreme sensitivity to the environment prompts graphene to be a remarkable candidate for sensor applications and measurements. There is also much research interest in bio-applications such as drug delivery, tissue engineering and regenerative medicine [5]. Graphene also displays potential as a viable candidate for nano-electro mechanical systems (NEMS) [6]. This has led to expectations of new graphene-based products in the next 20 years that were not even deemed possible a few years ago (fig.1.2 [5]).

Due to the challenge of separating single graphne layers from bulk graphite at a larger scale, there is a significant amount of research being conducted on other graphitic variations such as bi layers and few layers of graphene (FLG). All carbon structures, single to 3-D, exhibit different band structures and electronic properties.

Graphitic variations such as nanoribbons and nanoclusters have attracted considerable attention in terms of their applications [1]. Extensive investigations on thin films of graphite and nanographene platelets (NGP - thickness of NGP is less than 100 nm) report their potential in many applications [7].

In order to make use of the carbon nano-sheet structure and its properties, good-quality sheets have to be mass-produced reliably and economically. In many occasions, it has been highlighted that the applications of graphene largely depends on the unique properties of graphene [8, 9] and the properties are strongly affected by the method of synthesis [10]. Current graphene synthesis methods can be classified into several groups such as epitaxial growth, unconventional methods, and exfoliation techniques. In the epitaxial growth technique, graphene is grown on top of a substrate using chemical vapor deposition techniques [10–12]. Unconventional methods include unzipping CNTs, arc discharge, and detonation of chemicals. The unzipping of CNTs taken place in the longitudinal direction and is accomplished by several methods [13]. The arc discharge method involves the use of a high-current arc discharge between a graphite anode and cathode under a hydrogen and helium gaseous atmosphere [14]. In the detonation of chemicals, a mixture of natural graphite, nitric acid, and CH_3NO_2 is allowed to explode in a vessel and the graphene sheets were detected in the soot obtained [15]. All these methods suffer from various limitations such as poor yield, use of hazardous chemicals, contamination of graphene with impurities and functional groups, and long processing time. The exfoliation technique, the method of focus in this thesis, involves the separation of graphene layers from bulk graphite using thermal, chemical, and mechanical routines.

In the thermal exfoliation process the bulk graphite is oxidized, centrifuged, and ultrasonicated to achieve a single layer of graphene [16]. Chemical exfoliation is

performed at high temperatures and involves several processing steps and chemical combinations [17]. Mechanical exfoliation is largely performed using the simple scotch-tape method [18]. Repeated peelings are needed to achieve a single layer graphene and it is difficult to predict the number of peelings required. Several other micro-mechanical cleaving methods involve the use of an atomic force microscope (AFM) tip. In one method, the tip scratches on the material (HOPG islands) surface [19]. Another similar method involves attaching the HOPG material islands to the AFM tip, which then scratches on a silicon substrate [20]. In general, it is difficult to control the number of cleaved graphene layers using these micro-mechanical techniques.

There are differences in the graphene layers exfoliated chemically and mechanically. In terms of dimension, mechanically exfoliated layers are in the range of a few hundred micrometers. However, other chemical exfoliation techniques are able to produce much larger sizes. For example, chemical vapor deposition technique can grow graphene to approximately 1m in size. However, mechanically exfoliated layers are much cleaner and easy to separate, while chemically exfoliate layers overlap and this causes difficulties in separating the layers. Mechanically exfoliated layers exhibit extremely high carrier mobility values close to the theoretical predictions. All other methods produce graphene with carrier mobility values lower by few orders of magnitude. Chemically exfoliated layers are adequate for coating paints, composites, transparent conductive layers, energy storages, etc. While CVD graphene layers are sufficient for applications such as photonics, nanoelectronics, sensors and bio-applications. Despite the higher quality, mechanically exfoliated layers are largely restricted only to research investigations.

None of these methods have been established as a capable and reliable fabrication technique for industrial applications [8, 21–23]. As shown in fig.1.3 [5], the quality

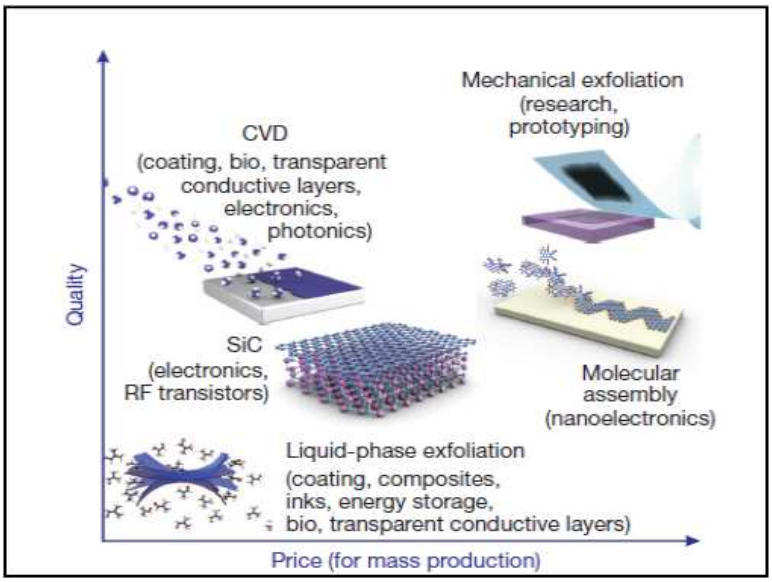

Figure 1.3: Comparison of price and quality of current manufacturing methods [6]

of the graphene layers are related to the cost and application requirements. Hence, this is an area of opportunity for research and commercialization, if one can come up with a solution for reliable mass production of quality graphene. There are several challenges to be addressed in developing a new fabrication technique for this novel material such as preserving uniform sheet thickness, producing them faster in the case of deposition and exfoliation (separation from bulk), ensuring higher yield at fast production rates, ensuring scalability to high volumes, and producing it in a pure state without any attached functional groups. As will be explained in chapter 2, the current methods explored by researchers today are predominantly chemical in nature and suffer from environmental problems (when scaled up), low yield, and poor scalability. There is thus a compelling need to reconsider methods such as mechanical cleavage technique to produce this material. There is extensive scope in exploring the mechanical exfoliation technique for graphene synthesis with potential for low chemical usage and better process controllability. Application areas where ultra-thin sectioning is routinely performed offer some ideas for the mechanical exfoliation of layers from a bulk substrate.

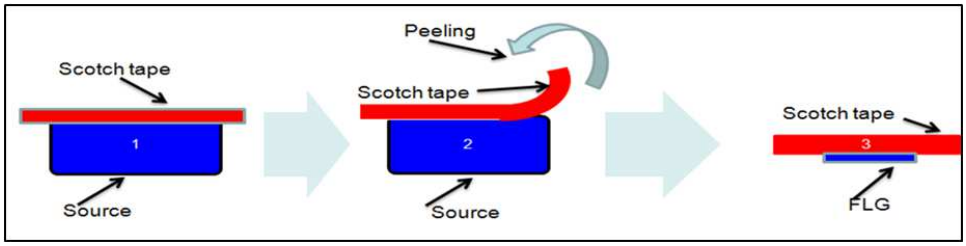

Figure 1.4: The scotch-tape method

1.2 Alternative Mechanical Cleaving Method

The scotch-tape method (fig.1.4 [5]) is a traditional mechanical cleavage method for producing graphene since its discovery [18] and currently used for research purposes. This is not a suitable technique to use as a mass-production method due to the difficulty of controlling the number of peelings required to obtain graphene. The conventional machining technique is a possible alternative method to use as a controlled mechanical cleaving technique. To use this technique, scaling it down to a few nanometers is necessary and to achieve this, special equipment is required that can provide the resolution iat this scale. Ultramicrotome techniques used for Transmission Electron Microscope sample preparation are applicable to nano scale cleaving and their general applications can be seen in the fields of biology and medicine [24, 25]. Under normal conditions, the mechanical separation of the material by machining at all levels-meso, micro and nano- results in chips (layers) that are severely deformed in the case of ductile metals and fractured in the case of brittle materials. The deformed and fractured chip behave very differently from that of the substrate material from which it is removed. The question then arises whether one can remove the material by machining in such a way that the chip has a structure not very different from the substrate material. Some of the factors that can help reduce the deformation in the chip are: a very high rake angle, a sharp cutting tool, and application of vibrations to the tool. Under such special conditions, the machined chip itself can be the ultra-thin layer or the film desired. Hence, the technique has

potential to produce ultra-thin layers such as few layers of graphene.

1.3 Objectives and Scope of the Thesis

The main objective of this thesis is to study the potential of applying a novel wedge-based mechanical exfoliation technique (WBME) to produce few layers of graphene sheets via both experiments and molecular simulations.

The investigations are carried out in several stages to achieve the above objective. The potential of the wedge-based exfoliation technique in producing few layers of graphene is tested via cleaving experiments. The exfoliation or cleaving setup consists of a feeding stage (an ultra-microtome), an ultra-sharp single crystal diamond wedge and a highly ordered pyrolytic graphite as the starting material. The exfoliated few layers of graphene are characterized by various microscopic techniques such as optical microscope, Raman spectroscope, atomic force microscope, scanning electron microscope, and transmission electron microscope for quantitative and qualitative analysis.

Detailed investigations are conducted to understand the effect of various factors through experiments and molecular simulations. These analyses include the studies on various process parameters that affect cleaving and a number of key features such as folds, rolled and sheared geometries on exfoliated layers. Further to the cleving experiments, nanoindentation experiments are used to investigate the wedge-material interaction. Molecular simulations are also performed to understand qualititatively and quantitatively the dynamics of the exfoliation technique at the atomic scale using the Large-scale Atomic/Molecular Massively Parallel Simulator (LAMMPS) package. The reserach road map is shown in fig.1.5.

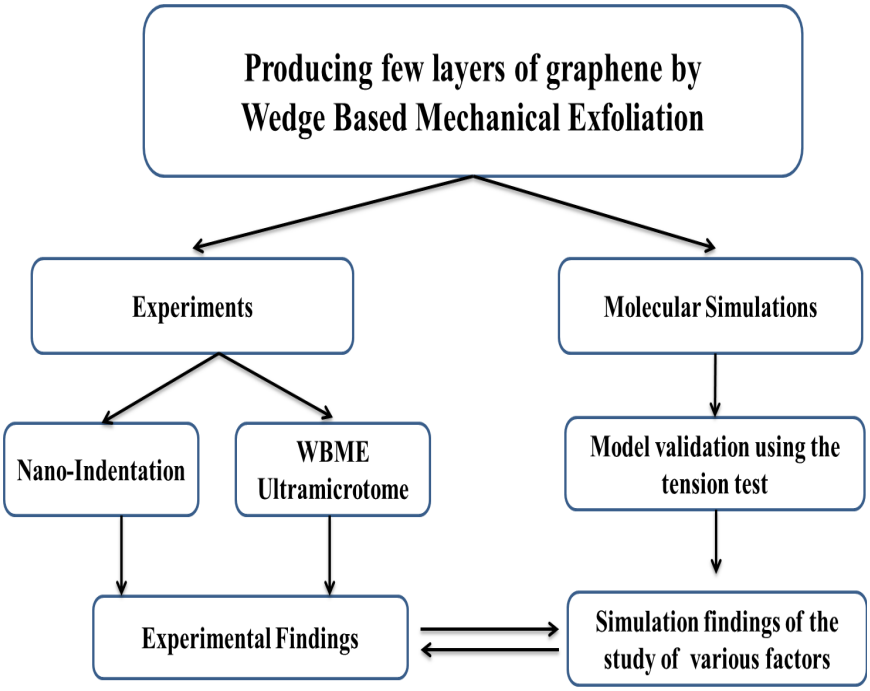

Figure 1.5: The research road map

1.4 Research Approach and Thesis Outline

The thesis consists of seven chapters. The second chapter highlights the existing graphene fabrication techniques, especially focusing on their advantages and disadvantages. A review of various graphene mechanical exfoliation techniques is also presented in this chapter. Following this, Chapter 3 describes the experimental setup used for the proposed cleaving technique. It further details experimental parameters and the characterization results. Chapter 4 includes the qualitative study of molecular dynamic simulations on the separation, folding and shearing of graphene and FLG during WBME. The effects of the wedge radius are also discussed in this chapter. Chapter 5 describes the experimental observation of carbon nanoscrolls and the cleaving mechanism using molecular dynamic simulations. Chapter 6 investigates wedge-material engagement via the indentation process. The thesis concludes with Chapter 7 highlighting the conclusions and outlining areas for further research.

Chapter 2

LITERATURE REVIEW

As observed in chapter 1 carbon nanosheets have great potential in a wide range of applications, because of the remarkable properties of thin carbon nanosheets. The previous chapter also briefly described existing fabrication graphene techniques. It reported that mechanical exfoliation technique can be developed further and that other methods have a number of drawbacks. It identified opportunities for developing the mechanical exfoliation technique to produce carbon nanosheets. This chapter elaborates further on the current trends in graphene synthesis and the challenges in existing carbon nanosheet fabrication techniques especially that of graphene that motivated the present study.

Section 2.1 presents the detailed structure and variations in carbon nanosheets. The following section describes current carbon nanosheets fabrication techniques presenting a broad classification. Section 2.3 discusses the existing exfoliation techniques and section 2.4 presents the tool-based mechanical exfoliation focusing on trends and applications at the nanometer level. It is then followed by a discussion related to large-scale processing methods of carbon nanosheets. Section 2.6 introduces a molecular simulation technique that is widely employed to investigate the

nanometric machining process.

2.1 Carbon Nanosheet Structure and Its Variations

Graphite is one of the materials that has been under scientific investigation for a long period. Graphite is in the form of a stack of graphene sheets. The distance between two adjacent layers is 3.35 A^0 while their in-plane (with layer) carbon-carbon bond length is 1.42 A^0 [26]. Graphite has weak van der Waals interaction between its sheets and a strong carbon-carbon covalent bond (sp^2) within the sheet. The weak bonds allow decoupling of the adjacent layers under an external stress. Naturally occurring graphite is generally mined and is typically contaminated with many impurities and is polycrystalline in nature. Flake, amorphous, and vein are considered as naturally occurring variations of graphite. Synthetic graphite can be produced through extrusion or pressing and these have displayed larger crystallite sizes compared to natural graphite with significant improvements in properties such as electrical resistivity; there are also remarkable differences in properties in the parallel and vertical directions [27, 28]. Synthetic graphite can also be made by pyrolysis or thermal decomposition of polyvinyldene chloride at 1000 ^{0}C [29] and the resulting graphite has a mixture of ordered and disordered structures. The process of graphitization depends on the less strong cross-linking and near parallel orientation of neighboring crystallites [30]. The crystal orientations of the ordered graphite can be improved further by applying uniform pressure on deposited pyro-carbon1 at high temperatures (3000^0C); the resulting graphite is called highly ordered pyrolytic graphite. Highly oriented pyrolytic graphite is a popular synthetic form preserves a high degree of layered structure even at high temperatures. The process of graphiti-

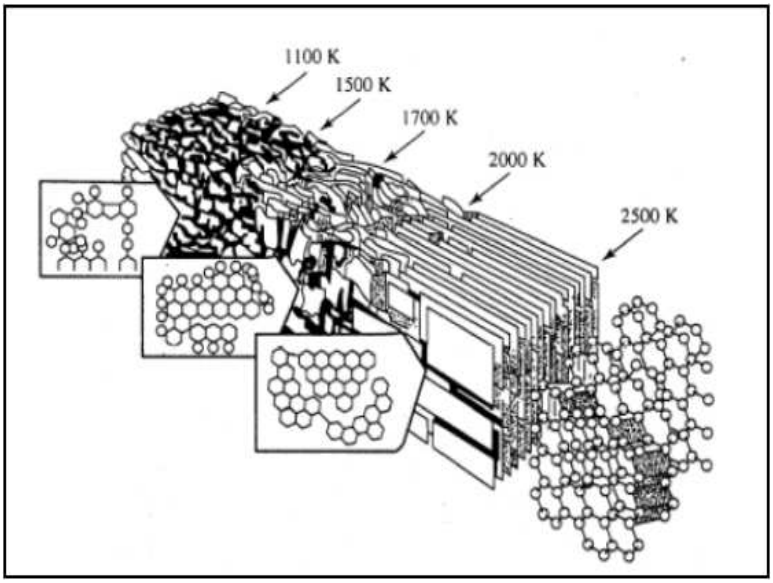

Figure 2.1: Crystalline arrangement under high temperature processing [31]

zation involves providing graphite with various degrees of crystallinity (fig.2.1 [31]) under different stage of elevated temperatures.

The graphene sheet structure is called as the honeycomb lattice. The graphene unit cell consists of two equivalent carbon atoms (fig.2.2 [32, 33]). Graphene sheets have two interesting edge structures named as armchair and zigzag edges. Graphene stacking modes are of three types: AA, AB, and ABC also called hexagonal, Bernal, and rhombohedral respectively (fig.2.3 [32]). The Bernal mode is the most popular naturally available stacking type out of these three [32]. The single sheet of graphene is considered as the basic building block of all other graphitic materials [3]. A fully wrapped sheet of graphene is called 0D fullerene and when it rolled up along an axis it is refereed to as nanotube. A 2-D structure is considered as a sheet and the 3-D form referred as the graphite.

Not only are single graphene sheets important, several layers of graphene are also proving useful for applications. These are referred as graphitic thin films. The literature reports a variety graphitic thin films such as flake graphite, graphite nanosheets,

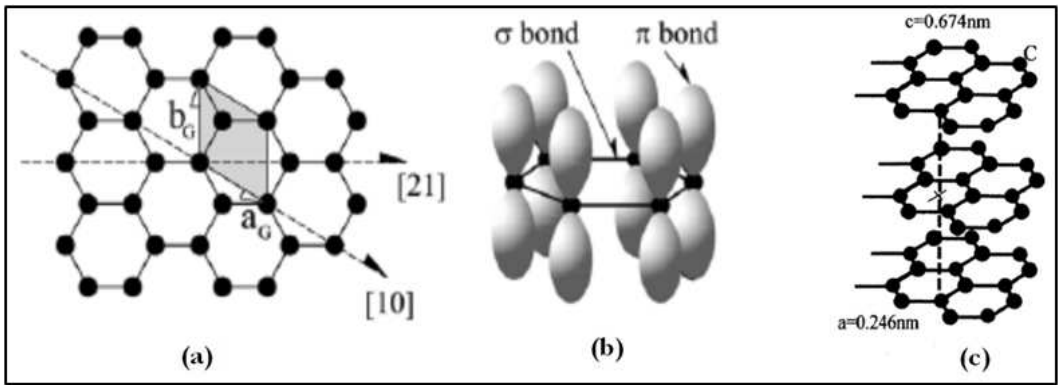

Figure 2.2: (a) Graphene hexagonal structure of identical carbon atoms. The unit cell (shaded) containing two carbon atoms is shown along with standard unit cell vectors aG and bG. b) schematic of in plane bonds and orbitals perpendicular to the plane of the sheets, (c) Graphite structure [31,32]

Nano Graphene platelets (NGP), xGNP, and few layers of graphene. These graphitic thin films also exhibit many unique properties and display potential in numerous applications [7]. The commercially available forms belong to various categories based on layer thickness. All graphite thin films below 100 nanometer thickness are generally called Graphene Nano Platelets (GNP). The xGNP, a commercially available form, has a thickness range of 1 to 20 nm (fig.2.4 [18, 34]). Flake graphite is in the thickness range of 30-80 nm and mainly exfoliated through graphite intercalation. Graphite nanosheets are also reported to be in the same thickness in the same range but are less dense than other variations such as flake graphite, xGNP, graphdiyne,

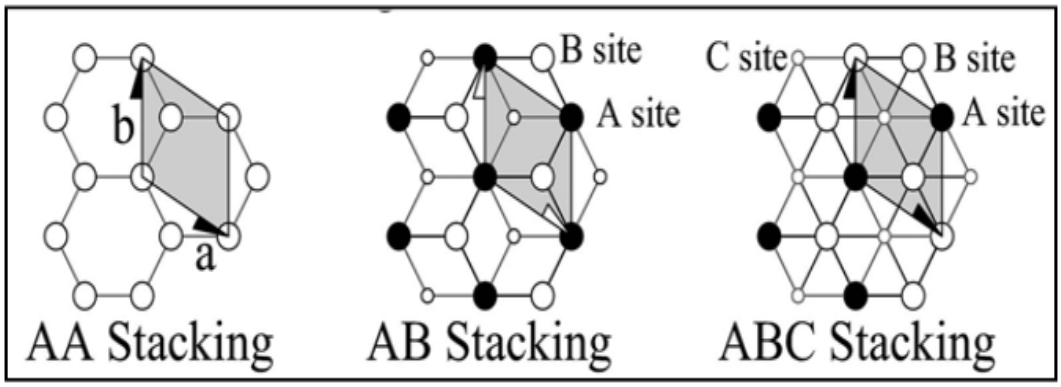

Figure 2.3: Stacking modes of AA, AB and ABC on multilayer graphene [32]

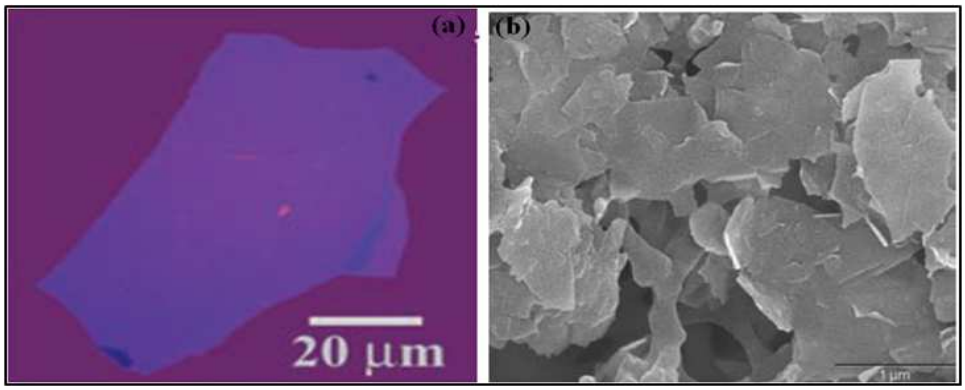

Figure 2.4: Carbon Nanosheet Variations: (a) Single sheet of graphene, (b) xGNP [18,34]

or NGP [7,35]. Additions of these graphite thin films change barrier properties and thus improve the electrical and thermal conductivities. They can also elevate mechanical properties in considerable extent. The applications of graphite thin films include ultra-capacitor electrodes, anode materials for lithium-ion batteries, additive for battery electrodes, electrically-conductive inks, thermally-conductive films and coatings, additive for light-weighting composites, films or coatings for EMI shielding, substrate for chemical or biochemical sensors, barrier material for packaging, additive for super-strong concrete, and additive for metal-matrix composites [34].

2.2 Carbon Nanosheet Fabrication Techniques

There have been many attempts to isolate graphene and after its various forms after its initial ground breaking discovery. Many reports have been published exploring varied production techniques. The properties of graphene largely depend on the manufacturing method [10]. The reported techniques can broadly be classified as epitaxial growth, unconventional methods, and exfoliation technique; these are elaborated in this section. As highlighted in chapter 1, this thesis focuses on exfoliation techniques. The exfoliation techniques itself can further be categorized into mechan-

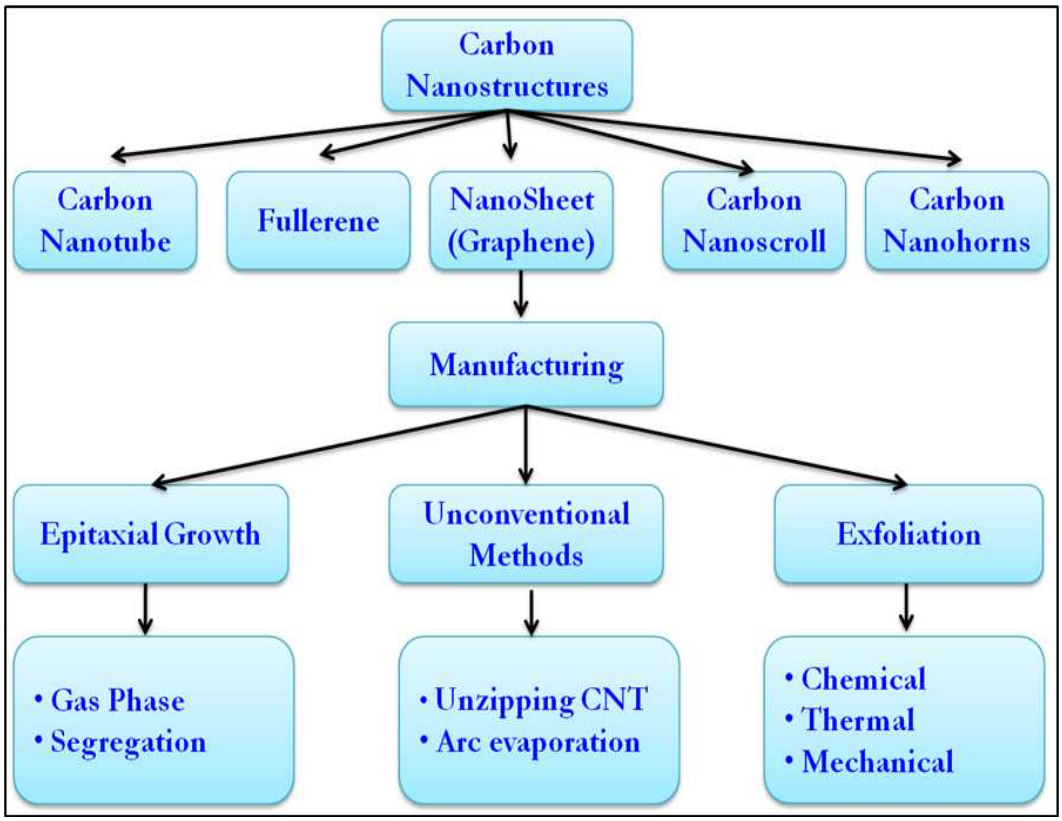

Figure 2.5: Carbon nanostructures and current graphene manufacturing methods

ical, thermal, and chemical categories and is discussed in the next section. Figure 2.5 presents an overview of various graphene manufacturing methods reported in the literature.

2.2.1 Epitaxial Growth

In the epitaxial growth technique, the graphene is grown on top of a substrate material such as metals (Ru, Ir, Co, Pt, Ni etc.) or insulators (silicon carbide-SiC) using physical vapor deposition (PVD) and chemical vapor depositions (CVD) methods [36–38]. The technique can roughly be divided into two types based on the supply of the carbon atoms. In one type, carbon is provided through the gaseous phase. In the other type, carbon atoms are segregated from the substrate to the

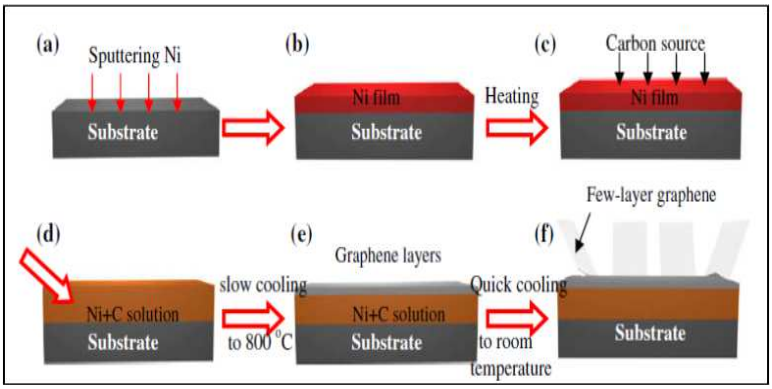

Figure 2.6: Epitaxial Growth graphene on a Ni film which placed on the substrate [41]

surface. The bonding between the substrate and the bottom layer decides the quality of the graphene layer [33]. A ultra-thin vacuum (10^5 Torr) and high temperatures (1250 -1450 ^{0}C) are applied during these processes [39]. Epitaxially grown graphene is treated as a new class of material due to complexity of its electronic structure. Generally, this process results in a final product that is a combination of single and multiple layers (4-100) [40]. High quality substrates are required for good quality graphene to be produced; all surface scratch marks have to be removed before the growth process begins [32]. An example of such epitaxial grown few layers of graphene is demonstrated by Zhang et al. (2010) [41] on a Ni substrate (fig.2.6 [41]). An additional sputtering technique is used to deposit the Ni layer before the epitaxial growth is initiated. Slow growth, non-uniform thickness, and maintaining high temperatures are challenges with this method. Many physical properties differ between graphene that is epitaxially grown and that is mechanically exfoliated [40].

2.2.2 Unconventional Methods

The methods other than exfoliation technique and epitaxial growth can be grouped as unconventional methods. These methods include unzipping carbon nanotubes,

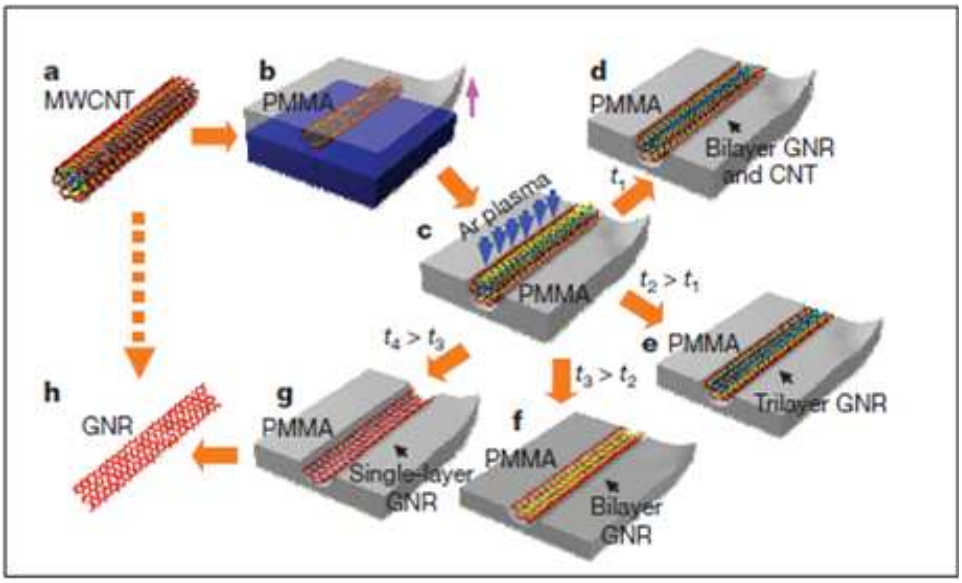

Figure 2.7: Graphene nanoribbons from unzipping multi-wall carbon nanotube [43]

application of arc discharge, detonation of chemicals, atomic layer deposition, and reduction from carbon monoxide. These methods are largely suitable for laboratory use and are still in their primary stages of development.

2.2.2.1 Unzipping carbon nanotubes

Unzipping CNT mainly focuses on achieving graphene by tearing through the carbon nanotubes longitudinal direction. The process of unzipping involves breaking up of rolled CNT that can results in various edge structures of the resulting graphene. Depending on the edge pattern, graphene behaves like a metal or a semiconductor [42]. There are four methods of unzipping CNT described in the literature. These techniques are: plasma cutting, chemical oxidizing, inserting an impurity atom, and microwave assisted cutting.

In the plasma cutting technique, the process starts with embedding mult-walled carbon nanotubes (MWNT) in a poly methyl methacrylate (PMMA) substrate. An Argon (Ar)plasma is applied to MWNT until the CNTs get separated (fig.2.7 [43]).

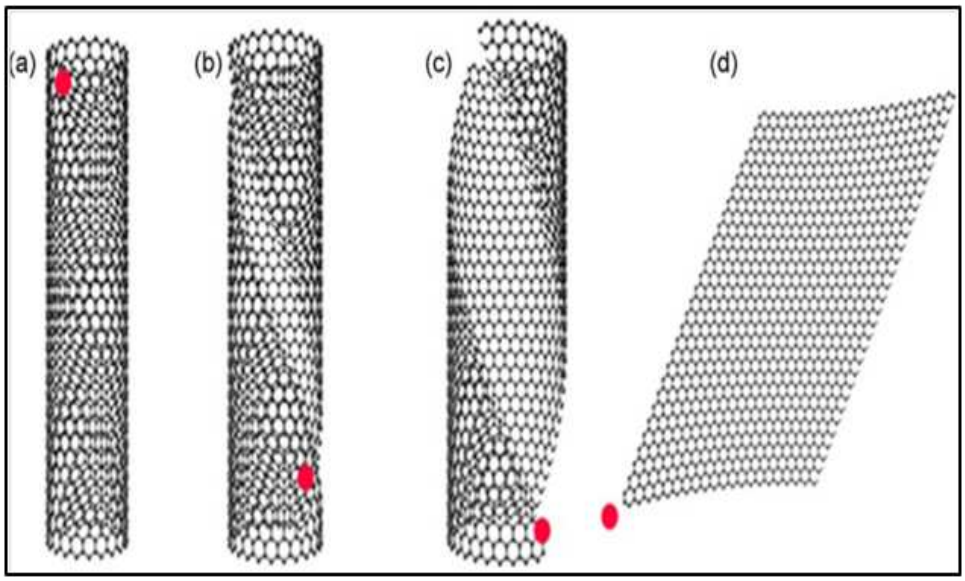

Figure 2.8: Different stage of unzipping carbon nanotube with palladium particles [13]

A potassium hydroxide (KOH) solution is used to peel off the multi-wall carbon nanotubes. The single, bi-layer and multi-layer graphene nanoribbons are separated by controlling the etching time. In this method, microwave irradiation (to provide heat) was applied under specific conditions such as 300 W, at 200 ^{0}C for 60-120 minutes inside a water bath. Palladium nanoparticles are mixed as a catalyst for the process and act as cutting edges.The decantation or toluenewater system is used to separate the FLG from the residuals. Figure 2.8 [13] represents the different stages of the CNT unzipping with the palladium particle as the catalyst . The microwave-assisted cutting technique is also capable of producing few layers of graphene.

Explain in another multi-walled carbon nanotube tearing method [42, 44], MWCNT is oxidized with the sulfuric (H_2SO_4) acid and potassium permanganate ($KMNO_4$) at room temperature. After one hour of treatment, the MWCNTs were seen to open out and consisted of 1-30 layers of graphene nanoribbons (fig.2.9 [44]). With this process, the opening of a SWCNT is difficult due to entanglements.

Another CNT unzipping method is reported to produce graphene nanoribbons as-

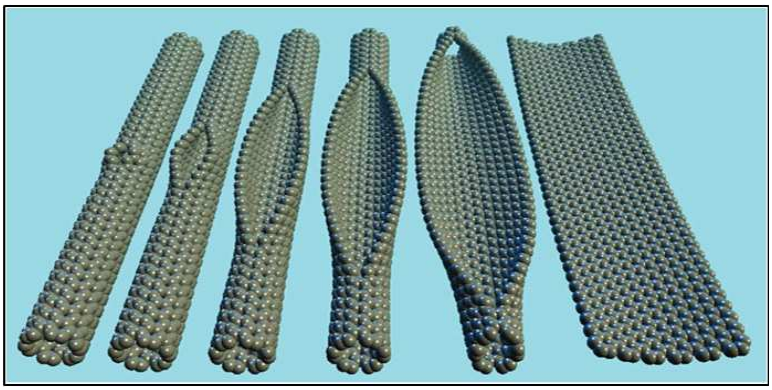

Figure 2.9: A schematic diagram of gradual unzipping of one wall of a CNT to form a nanoribbon [44]

sisted with Li as a catalyst [45]. A metal atom (Li) is inserted with ammonia followed by a thermal treatment. This process starts with the MWCNT and is subjected to sonication in a dry tetrahydrofluran environment. Then, it is mixed with liquid ammonia, liquid nitrogen and acetone. Granule form of Li is added and kept for a few hours to settle. Finally, hydrochloric acid is added and the residuals are collected through a micro fabrication membrane [45]. Intercalation increases the inter-layer spacing by expanding and it ultimately fails with a rupture (fig.2.10 [45]).Use of harmful chemicals, smaller size of nanotubes, low yield, and high cost of initial materials do not suit this method for large-scale production of graphene except for a few limited applications.

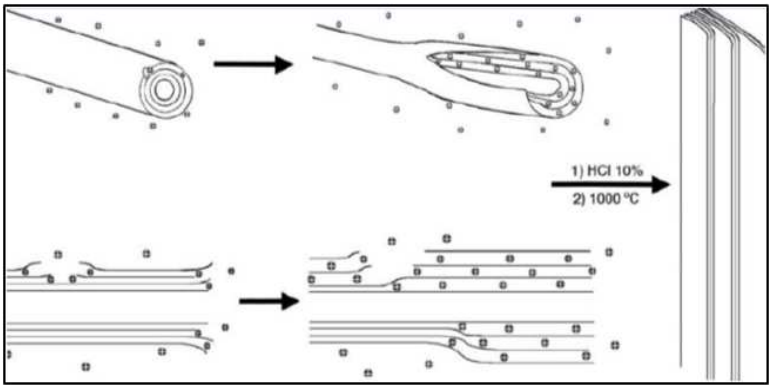

Figure 2.10: Unzipping multi-wall carbon nanotube with Li catalist [45]

2.2.2.2 Arc Discharge Method

Discharging an arc between two graphite electrodes method has also been tested to find the suitability of the process to produce graphene [46]. Experiments were conducted in a helium atmosphere with different pressures. Graphite rods are used both as anode and cathode. The gap between the electrodes is maintained at 2mm and a high current (100 A) is provided. The cathode's black soot is collected and examined for graphene. It is reported that soot contain a combination of single, bi, and multi layer graphene [47]. Low throughput, contamination of graphene with impurities and poor control prevent implementing this process as a large scale industrial process.

In addition to the above processes, there are several other techniques tested to fabricate carbon nanosheets. Detonation using chemicals is one technique that has been tested. Natural graphite, a concentrated nitric, and CH_3NO_2 are used as the raw materials [48]. The explosive nature of the experiment, hazardous chemicals, combination with impurities, low yield hinders the use of this route to be established as a large-scale industrial process. The atomic layer deposition is also demonstrated as a graphene manufacturing process [49, 50]. However, the high initial equipment cost, risk of impurities and time-consuming process has become significant barriers to its progress. A catalyst assisted cutting method termed as Nano cutting reported in the literature as another multi-stage technique to fabricate carbon nanosheets [51, 52]. This process uses a nickel particle as a catalyst. The size of the metal particle is a key parameter in this process and largely it reported achieving the nanoribbons. Overall, these methods involve looming issues such as high cost, time consuming, and low yield. Therefor, it is very hard to imagine their applications on larger scale at this moment.

2.3 Exfoliation Techniques

Exfoliation is a technique that removes or separates a layer of material from its stacked bulk. This can be performed in several ways and in graphene, these methods broadly classified into chemical, thermal, and mechanical. The properties of the exfoliated material largely depend on the technique that is used. Following sections describe the existing exfoliation techniques reported in the literature for fabricating these carbon nanosheets.

2.3.1 Chemical Exfoliation

Chemical exfoliation is a popular method to produce carbon nanosheets. In one method, colloidal suspension are used and in the other, a compound is inserted between graphene layers to exfoliate. The colloidal suspension method uses a liquid solution to suspend the graphene (fig.2.11 [53]). This method utilizes surfactants or stabilizers, though there are recent attempts to remove the surfactants from the process [54]. Graphite oxide, the starting material, is mixed with an aqueous or organic solvent with the aid of sonication [12, 55]. A number of solvents such as water, methanol, acetone, ethanol, dimethylformaide (DMF), tetrahydrofuran (THF) are employed to dissolve the graphite oxide. The derived graphene oxide sheets is electrically insulating and require another separate process (chemical, thermal, or UV-assisted) to convert them into electrically conducting graphene oxide [53]. Graphene oxide sheets display negative charges when dispersed in water and this provides a stable suspension. Generally, graphitic layers produced by this method are composed of hundreds of layers (average 30 nm to 100 nm). The lateral sizes of the obtained sheets vary less than 1 micro-meters [12]. A number of draw backs are involved with this method: poor yield, less quantity, low quality, attach of functional

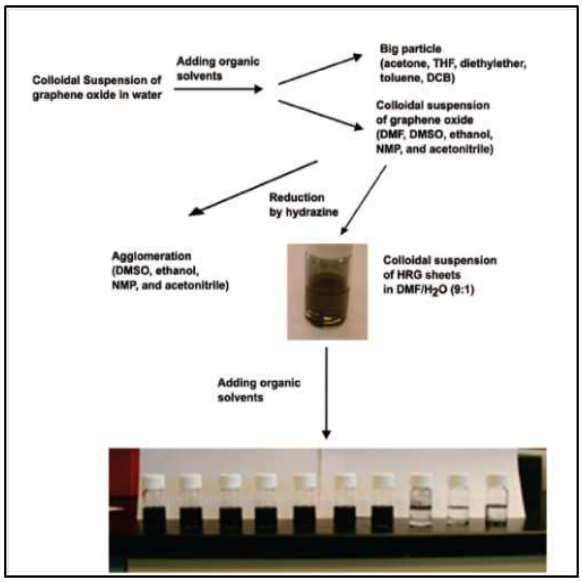

Figure 2.11: Colloidal suspension process to produce graphene [53]

groups, high cost, safety of solvent, removing residual from solvent, length of time to stabilize, use of chemicals, and significant number of defects, etc. [12].

In another method, intercalation compounds are used to exfoliate the graphene (fig.2.12 [56]). Graphite intercalation has been known to scientists for more than a century but in the last four decades it has become a very active field of research [57, 58]. The intercalate is expected to move between the layers and as a results inter-layer spacing is increased. The van der Waals bonds strength are also depleted and exfoliation yields the carbon nanosheets including the single layers of graphene. Various intercalation compounds such as Te Potassium (KC_8), the Cesium (C_8Cs), and the Ferrous ($FeCl_3$) have been tested [56, 59]. In several experimental investigations intercalation is undertaken twice before achieving the desired layers. Poor the controllability, use of hazardous chemicals, and poor yield have become a barrier to these types of methods in progressing to an industrial scale.

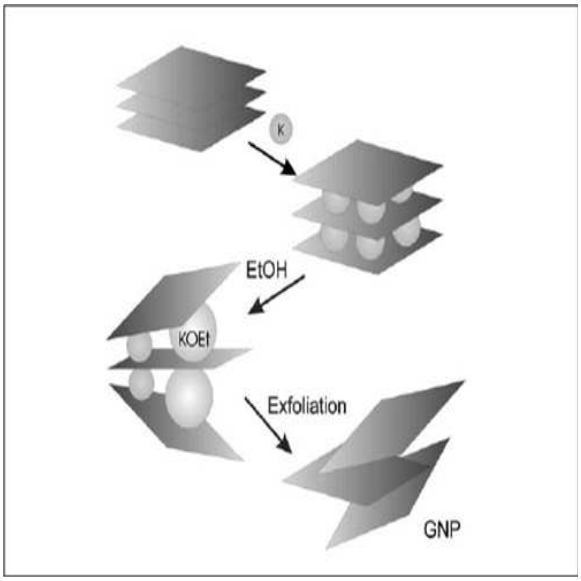

Figure 2.12: Schematic diagram for graphite intercalation and exfoliation [56]

2.3.2 Thermal Exfoliation Methods

Thermal exfoliation is a combination of several processes (fig.2.13 [16]). The process initiates with graphite (natural or graphite oxide) as the raw material and oxidization is first carried out. This is followed by thermal expansion, centrifugation and ultra-sonication [16, 46]. A number of toxic chemicals and high temperatures are used in this process to produce carbon nanosheets. The hazardous chemicals used such as the Potassium Permanganate ($KMNO_4$), nitric, and sulfuric acids at high temperatures resulting violent chemical reactions. The intercalation and oxidization take place over a long period of time. Thermal exfoliation is also associated with many of the previously explained de-merits. Therefore, implementing this method as a large scale graphene manufacturing method is questionable [60].

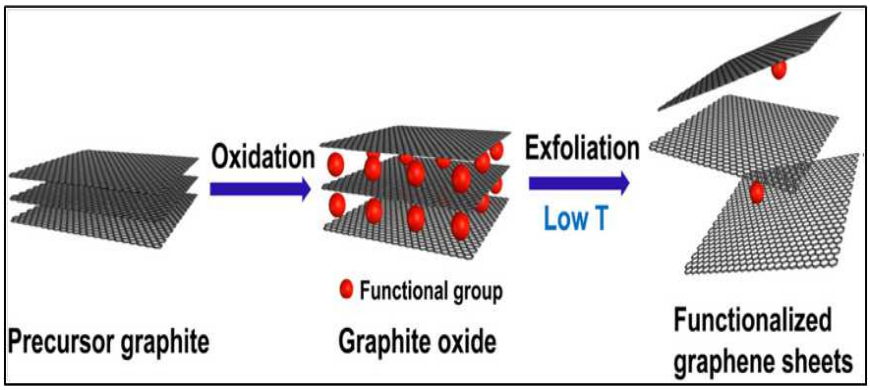

Figure 2.13: Thermal exfoliation under low temperature [16]

2.3.3 Mechanical Exfoliation

As we highlighted in an earlier section (chapter 1.1), a number of techniques have been reported for exfoliating graphitic layers mechanically. The very first separation and isolation of single layer of graphite was performed with a simple mechanical exfoliation technique using an adhesive tape (fig.2.14a) [18]. The process was initiated by creating islands of protrusions on the HOPG sample surface. These mesas were prepared by oxygen plasma etching. Then, a scotch tape was used to peel repeatedly to produce several layers of thin films ending up with graphene among the few layers. These single layers were found as patches. Such peeling-induced mechanical exfoliation (fig.2.14a), while producing high quality graphene, has limitations of low yield and poor process control. This scotch- tape method has been largely restricted to laboratory based sample preparation. Several other mechanical techniques have also been exploited to separate thin layers of graphite (fig.2.14b) [19, 20]. One such technique involves manipulating an island of HOPG by sliding it on a Si substrate using the tip of an Atomic Force Microscope (AFM) [19, 20]. Another technique involves microtome sectioning (fig.2.14c) using a wedge; this is a simple and versatile method to produce thin sections of various materials. This technique more popular in biological sample preparation and use either glass or diamond cutting

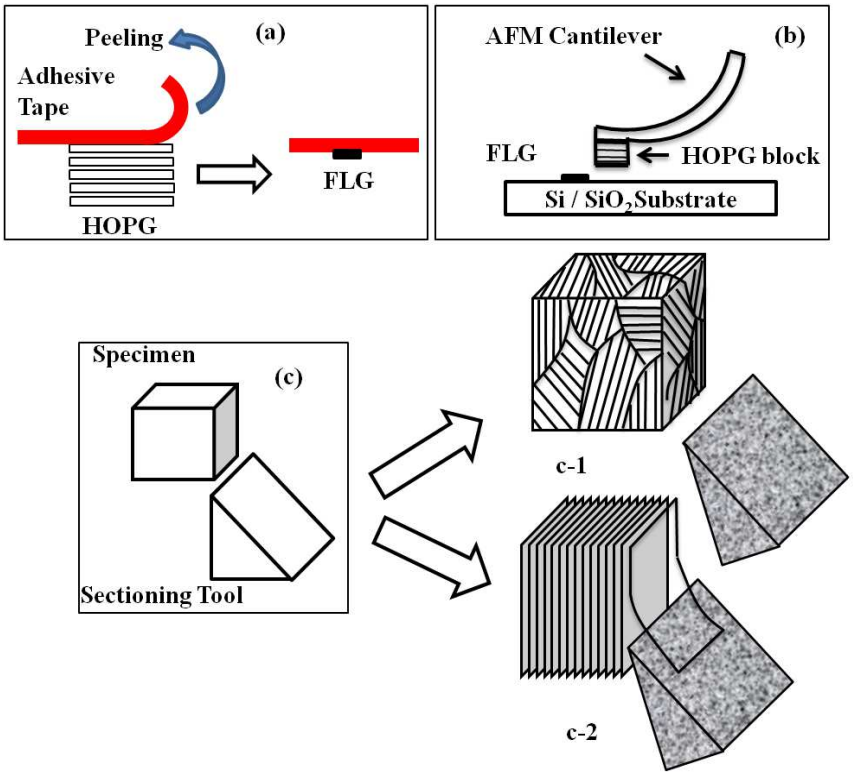

Figure 2.14: Mechanical exfoliation methods; (a) Scotch tape method, (b)Scratching HOPG islands with Atomic Force Microscope tip,(c) Microtome sectioning: (c-1) Un-oriented sectioning of graphite and (c-2) Oriented sectioning of HOPG.

tool [24,61–63]. Mica, a layered material, was cleaved using a glass wedge indicating the possibility of layer separation as early as in 1930 [64]. Brittle and hard materials such as germanium, aluminum etc have also been sectioned to nanometer scale using this technique with thicknesses in the range of three to five nanometers [65]. Microtome sectioning has been applied to graphite not as a exfoliation technique but predominantly to study the characteristics of graphite such as stacking faults and crystallite sizes of synthetic graphite [66]. In another study, the structure of industrial carbon is determined during graphitization by sectioning bonded and natural carbon [67,68] at various stages. A recent work reported micrometer-thick graphitic sectioning of highly ordered pyrolytic graphite using a microtome and showed the imperfections and defects on the sections obtained [69].

None of the studies that used microtome sectioning focused on the orientation of

the graphitic layer arrangement during sectioning. Directionally sectioning the thin graphitic layers parallel to the basal plane is intuitively the best way to overcome the weak van der Waals forces between the layers. Directional sectioning may have a high potential to produce defect free layers particularly with HOPG; aligning the tool parallel to the layers may also require less energy for sectioning leading to less damage being induced in the sectioned layers. Hence, in this study our focus is on sectioning of HOPG parallel to the basal plane using a microtome wedge.

2.4 Mechanical Cleaving Using a Cutting Tool

Mechanical exfoliation or mechanical cleaving can be performed with the aid of a tool to separate the part of a material from its base material. This technique exists from the Stone Age. Mechanical exfoliation has been a part of human life and is evolved from scraping fur from animals, chopping wood, cutting metals to current facial scrubs and peeling several atomic layers from base material. However, this technique requires cleaver manipulation of process and tools to adapt it in various applications. In the era of industrial revolution, there has been high demand for finished products and it leads to mass production technology. The conventional machining technique played a vital role in the development of automatic machine tools for highly reliable processes. The fundamental studies were started to understand basic mechanisms of machining and simultaneously the theories were developed to enhance the processing techniques. In the era of miniaturizing the products, new avenues are opened and posts many challenges in the process reliability. Micro and nanometer level applications seek new methods to produce their feature sizes and leads to high demands for chemical free, low cost and fabrication techniques with short lead-times. The mechanical cleaving has shown a great potential as a fabrication method in this micro and nanoscale applications especially avoiding high cost

clean room techniques. Varieties of terminologies were presented such as nanoskiving, nanotomy, and controlled chatting for mechanical cleaving process in nanoscale. The equipment microtome is the basis for all these techniques.

2.4.1 Mechanical Machining

The nano/micro machining process focuses on mechanically removing a small amount of material (usually discarded later) leaving behind micro-nanostructures on the base material. This has attracted significant interest in many disciplines during the past decade [70]. This technique is applicable to use for a wide range of materials. The process is more similar to the conventional machining except for the scale at which it is operating. An earlier study reported 1 nm thickness layers [71]. The nanomachining technique has been used to remove one nanometer thick layers from the copper and 10 nm layers from the aluminum by diamond turning [72]. The process of nanomachining divides into four categories; deterministic mechanical nanometric machining, loose abrasive machining, non-mechanical nanometric machining, and lithographic methods [73]. In this study, we focus on the first group where control tools are applied in nanomachining process. In this domain, parameter measurements are much difficult and required high degree of precision instruments.

Orthogonal machining is defined as the cutting edge perpendicular to the direction of motion of the tool [74]. A model for orthogonal cutting was defined based on the several assumptions and the shearing is considered as the main mechanism of material removal. A number of significant parameters and regions are identified which influence the cutting process. As shown in (fig.2.15 [75, 76]), rake angle , cutting velocity, unreformed chip thickness, and chip thickness are the most important parameters. There are two shear zones-primary (A) and secondary (B)-where the chip undergoes deformation due to shearing and sliding. Merchant describes

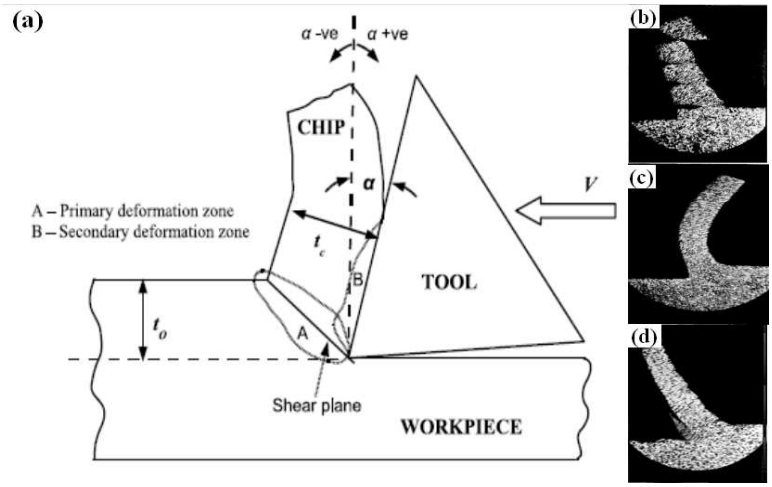

Figure 2.15: Orthogonal Cutting process [75], (a) Process parameters, (b)-(d) Basic chip types [76]

a model called Merchants circle for force calculation considering the forces acting on tool and chip [77]. In conventional machining, the focus is mainly on the newly generated surface. However, in this study, the focus is on the generated chips.

It is well known that the higher rake angle reduce chip thickness and the associated deformation [78]. It is also reported that the sharp cutting tool reduce the plowing effect and the deformation induced in the machining process [79]. As reported, the vibration assisted machining (VAM) also shrink chip thickness variation, tool forces, surface roughness, and damage. It improves the accuracy and tool life against the conventional machining. There are several ways to apply the vibration. In conventional practice, oscillation is applied along the cutting direction or maintain either linear or circular/elliptical tool path [80]. Recently, it was also shown that the application of ultrasonic oscillation along the cutting edge perpendicular to the machining direction has considerably reduce variation of chip thickness in micro-scale [81].

Merchantet et al. [76] reported mainly three types of chips using the conventional orthogonal machining (fig.2.15b-d). These are named as discontinuous or segmented

chips, continuous chip without built-up edge, and continuous chips with build-up edge [82]. The chip formation mechanisms, flow, and chip curling have been investigated extensively [83]. The orthogonal cutting process expects chips to move long the tool face. However, due to the uneven velocity distributions there is a possibility to move them sideways [84]. Generally, brittle material machining expects to break the chips without plastic deform due to propagation of fracture. There is no clear description for material removal mechanism in nanoscale. According to Komanduri et al. [85], researchers still assume the macro-scale predictions of material removal taking place ahead of the tool by the formation of chips even for nanometer regime. In this domain tool radius plays a significant role. They investigated the nanoscale ductile material machining with an AFM tip and concluded that material removal mechanism largely due to the tool ploughing.

The brittle material machining is also a segment of interest during this study due to the use of the brittle material HOPG. Atkins et al. investigated a wide range of factors that influence the brittle material machining. His research group reported a method to drive fracture toughness by obtaining the forces during the brittle material machining [86]. Atkins use the term floppy Offcuts to introduce microtome cutting. He performed a comprehensive analysis on cutting and frictional forces [87]. Williams et al. [88] presented an numerical analysis of wedge splitting which is the action more similar to the cleaving mechanism. Patel et al [89] presented a detailed analysis on cutting a polymer sample with the aim of finding the fracture toughness. Wyeth et al. [90] discussed machining of Polymethyl Methacrylate (PMMA) material under various conditions with respect to the type of chips generated.

2.4.2 Microtome Sectioning

A microtome technique is a tool-based cutting technique to produce desired features or sectioned of materials. The application of microtome technique is mainly in the field of material science. This technique is frequently use in the biological sample preparations for microscopic analysis. Recent advancement of serial sectioning using microtome opens new avenues in 3-D reconstruction (especially anatomical information) of images which heavily used in medicine related studies [91, 92]. The technique has the potential of studying the nano-scale crack propagation processes, the chip forming process, characterization of molecular anisotropy, and determination of cell wall fraction in cellular solids due to nanometer regime sectioning [93]. Two or three dimensional metallic nanostructures provide numerous applications such as optical filtering, substrates for optical detection of chemical and biological analysis, surface-enhanced Raman scattering ,substrates for enhanced luminosity, materials to augment absorption in thin-film photovoltaic devices, meta-materials with negative magnetic permeability, and negative refractive indices, surfaces for perfect lenses, and invisibility cloaking are examples of possible and realized applications [94]. A large number of materials: metals, semiconductors, metal-oxides, conjugated polymers (semiconducting and conducting), and films of semiconductor nanocrystals, can be sectioned by cleverly manipulating the material during the preparation [95]. Such sectioned nanostructures can also be used as the magnetic particles for digital storage patterning functional, surfaces for biology and devices for energy conversion and storage [96]. Material sectioning has emerged as one of the ways to make these nanostructures. This sectioning technique has developed as a nanoscale fabrication method that avoids expensive clean room techniques that use for nanofabrication. The ultramicrotome process has a capability of replacement for polishing, focus iron beam (FIB), and iron thinning for several applications [97].

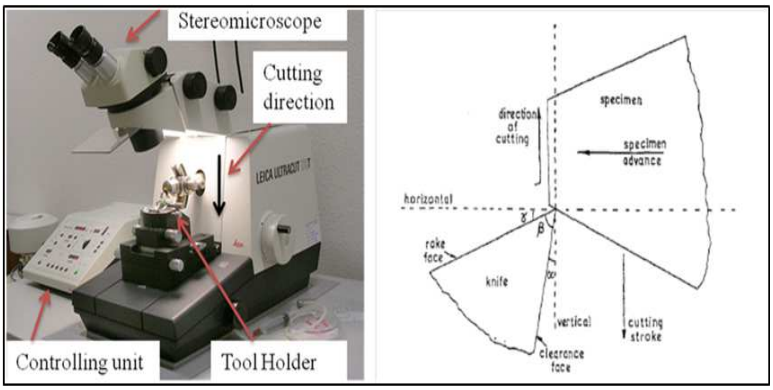

Figure 2.16: Ultramicrotome and cutting operation (a) A Commercial ultramicrotome, (b) Orthogonal cutting process with ultramicrotome [62]

Mica, another layered material, was cleaved using a glass wedge indicating the possibility of layers separation as early as in 1930 [64]. Brittle and hard materials such as germanium, aluminum etc have also been sectioned to nanometer scale using this technique with thicknesses in the range of three to five nanometers [65].

The feeding system of ultramicrotome can be classified into either thermal or mechanical, the former being more accurate for generating a layer thicknesses less than 100 nm. Interference color can be used as a rough guide to ensure that the thicknesses in the nanometer regime during cleaving process [98]. The sectioning can be carried out either at room or low (cryo) temperature conditions. Figure 2.16 shows an ultramicrotome that available commercially. The orthogonal cutting action is employed in the ultramicrotome cleaving technique (fig.2.16b [62]). The chip or the desired thin-layer is moved along the rake face and floats on to the water boat that attached to cutting edge. Distilled water is used as a liquid due to its surface tension, low viscosity and low rate of evaporation [62]. There are number of process parameters considered in the course of the ultramicrotome. The parameters such as cutting speed, slicing thickness, and rake angle play a dominant role in achieving defect free chips. Defects are one of the major concerns of this technique; instrumental faults, stress during cutting, and chatter are identified as the main causes.

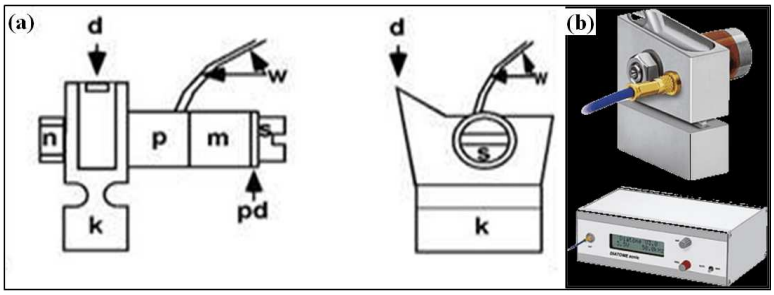

Figure 2.17: Ultra-sharp diamond wedge (a) Schematic diagram of a oscillating diamond wedge (b)Commercially available diamond wedge [61]

The tool is kept fixed while the work material is moved during the slicing. The process parameters are decided based on the material of the cutting specimen.

A notable feature of the sectioning technique using a microtome is the use of ultrasonic oscillating diamond knife. (fig.2.17 [61]) describes the components of an oscillating diamond wedge. The self-containing unit consists of a diamond wedge (d), a stage (k), an oscillating piezo translator (p), a washer (pd), a metal rod (m), a nut (n), and connecting wires. The wedge is oscillated in a direction parallel to its cutting edge. Amplitude and frequency can be altered independently [61]. A commercially available oscillating diamond wedge is shown in (fig.2.17b). Change in the geometry of the ultra-thin layers in the cutting direction is called compression and this is a critical factor for success of these ultra-thin sections [24]. It is reported that oscillation reduces the compression by nearly a factor of two. In conventional machining, chips are removed by shearing. However, in nanoscale is not clear the mechanism that removes the material.

The following table 2.1 summarized the identified gaps in earlier attempts on mechanical exfoliation and reported sectioning methods. It also identifies the major characteristics of the proposed wedge-based mechanical exfoliation techniques to overcome those limitations.

Table 2.1: Summary of the gaps identified prior reported other mechanical exfoliation and sectioning techniques

Description	**Prior work of mechanical exfoliation**	**Prior work of sectioning technique**
Critical requirement for mechanical exfoliation	To establish mechanical exfoliation as a manufacturing process, it is required to have a reliable, repeatable, high yielded and controllable process less sample preparation and minimum damages to the sample	Controlling of the thickness of the layers removed Controlling defects by directional sectioning Aligning the tool parallel to the layers may also require less energy for sectioning
Issues not addressed in the literature	Difficulty of controlling this process Poor yield The small size of the exfoliated layers [10] To avoid the significant initial sample preparation technique (lithographic) that used in AFM based exfoliation [19, 20] Minimum attempt on understanding the process mechanisms	No attempt has been made to control the removed material (chips) such that to obtain very thin layers Focused was not on the orientation of the graphitic layer arrangement during sectioning
Challenge in the addressing these issues	Scotch tape was only restricted to laboratory based research work	Predominantly the focus was to study the characteristics of graphite such as stacking faults and crystallite sizes of synthetic graphite [66]

	Significant trend to develop various chemical methods for graphene production over the mechanical exfoliation The size of the available highly ordered pyrolytic graphite might have a significant deciding factor; though the intercalation techniques [57] use HOPG as a starting material the CVD techniques developed use gases as the starting material Quality of graphene can be a trade-off with certain applications [5]	Determining the structure of industrial carbon by sectioning bonded and natural carbon [67] Not intend to section very thin layers [68]
How this thesis attempts to address these issues	The discussed sectioning method used a wedge to penetrate inside the material and peel a thin layer of graphite Introducing a controlling mechanism by precise positioning of the wedge to have a repeatable process Avoiding chemical contaminates Increasing the yield and the size of exfoliate sheets Understanding the process mechanism when the wedge is interacting with the material via molecular simulations	To control and understand the removed material (chips) such that to obtain very thin layers Directionally sectioning for thin graphite layers parallel to the basal plane Aligning the tool parallel to the layers for sectioning may lead to less damage being induced in the sectioned layers.

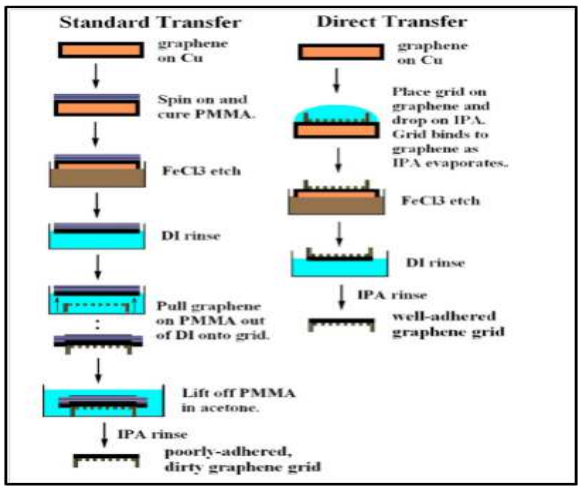

Figure 2.18: Chemical approach of graphene transferring; Comparison of standard polymer-based and propose (direct) methods [100]

2.5 Graphene Processing Methods

Handling of the carbon nanosheets especially graphene is an important during the processing. Transferring graphene from one substrate to another opens an avenue for device fabrication and characterization. Due its fine thickness, great care has to be taken to avoid additional damages on inducing stresses that may cause alteration of its properties. As explained earlier in section 2.3, various substrates are used for graphene processing. During very first isolation of graphene, the scotch-tape peeled flakes were attached to a photo-resist and they were released in acetone before collecting on to a Si/SiO_2 substrate [18]. Another method for transferring mono-layer graphene was introduced using a combination of chemicals [99]. Regan and coauthors [100] reported another transfer method for large area processing. It avoids adapting wet chemical and other conventional steps that cause additional mechanical stresses. They compared the technique with the standard method based on polymer as in fig.2.18. The standard method uses PMMA, by spin coating it anduse it as a rigid support for the graphene layer. The proposed new method (direct method) applies isoproponoal (IPA) to strengthen the bond between graphene and

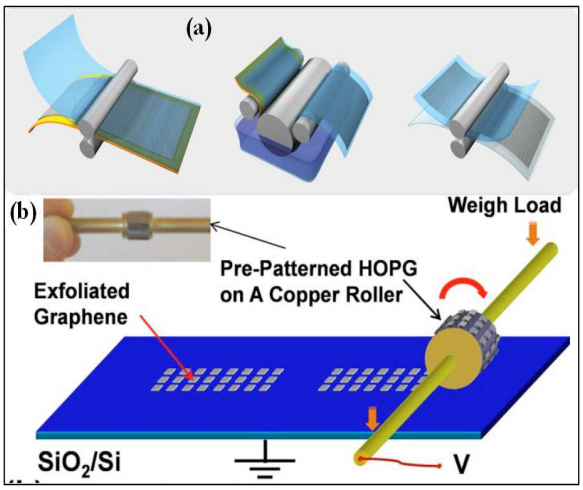

Figure 2.19: Roller assisted graphene transferring (a) Schematic diagram of Roll to Roll Production [103], (b) Schematic diagram for roller-style EFEG - fabricated roller-style HOPG template [104]

Cu grid [100]. Reina et al. (2008) [101] reported a method that used PMMA to transfer graphene from one substrate to another. A number of research groups selected PDMS as a supporting substrate due to the low surface energy that makes it easier to transfer graphene to a substrate [102]. Bae et al, [103] presented a large area transferring technique for CVD grown graphene on a copper foil (fig.2.18a [103]). In this method, the support (polymer) substrate is attached on the graphene grown copper foil and then the foil is removed by an etchant. Following this, the graphene layer is released on to the target substrate. Another similar attempt [104] was made with an electrostatic force applied to the exfoliated layers of graphene using a roller technique (fig.2.18b).

2.6 Molecular Simulations

The nanomanufacturing processes can be better controlled if the process mechanisms are well understood. Especially a process like nanomachining is not amenable to observation in-situ during the process. The use of computer-simulation provide

an efficient and alternative solution. The choice of simulation technique depends on the conditions it is executed. Density functional based calculations such as local-density approximation (LDA) and generalized gradient approximation (GGA) are not suitable for application at such finite temperatures [105]; they are only suitable at ground state (0 K). DFT based methods are currently being extended for finite temperature conditions [106] though there are significant challenges to be overcome. Molecular Dynamic simulation is one technique that can be used to obtain the dynamics of the system. It predicts macroscopic properties through microscopic states at the molecular level. It is able to simulate the system in atomistic (molecular) scales. Molecular dynamic models incorporate the classical equation of motion and numerical integration for time steps. In MD, several critical parameters such as the potential function, the time-step, and the boundary conditions contribute to the accuracy of the simulated results. The potential function is an empirical formulation. The potential energy calculates the forces acting on the atoms. Numerous potential functions such as the Lenard Jones (LJ), the Adaptive Intermolecular reactive empirical bond-order (AIREBO), the Tersoff etc, are developed to represent the bonding nature of the various materials.Although, there are developed potentials such as registry-dependent potentials (RDP) to overcome some of the draw backs associated with LJ, the performance of these two potentials are similar at finite temperatures. It is particularly pointed out [107] that dynamic effects dominate at finite temperatures; phenomenon such as rotational corrugation dependence on circumferential periodicity in DWCNTs, observed at 0 K (using molecular mechanics calculations) are not displayed at finite temperatures (when simulated using RDP based potentials incorporated in molecular dynamic computations). These authors argue that dynamic effects at finite temperatures (300 K) dominate and thus these effects are not observed. It is also reported [108] that LJ potential shows similar performance to RDP based potentials at temperatures in the range of 16-298 K,

when both are compared in a molecular dynamic framework to simulate peeling and exfoliation of graphene layers using nanoasperities, a process that involves both separation and some shearing. Only at temperatures in the range of 2-16 K significant differences are reported.

A large number of commercial and open-source software packages namely, Large-scale Atomic/Molecular Massively Parallel Simulator (LAMMPS), AMBER, COSMOS, CHARMM etc., are currently available to develop an MD model. Packages like Visual Molecular Dynamics (VMD), AtomEye, PyMol etc, support the visualization of atom trajectories during the simulation steps. The LAMMPS is developed by Sandia National Laboratory [109]. The literature publishes many reports that use LAMMPS to investigate the various research problems [110–112].

However, this method has improved to test a larger system using the coarse grain technique [113]. The conditions used in an MD model are far from that use in actual experiments. For example, the number of atoms at the macroscopic level is in the order of 10^{23} ($1cm^2$) but the models use only a few millions (maximum) of atoms due to the computational restrictions. The atomistic simulations are still computationally intensive [114]. Despite these limitations insights drawn from these simulations such as deformation mechanisms [115–117], reveal very important details that are extremely difficult or impossible to observe with the experiments to study at macroscopic level [118]. This well established method has been using in a wide range of fields to study various phenomena such as material removal mechanisms, effects of tool geometry, the temperature effects, the process parameters such as cutting speed and cutting forces [119–123]. The simulation of machining process is one such problem that investigated through a molecular dynamic model. Komanduri and coauthors applied MD to predict the wear mechanism of nanometric cutting using LAMMPS [118]. Cheng et al. (2003) [35] used simulation dynamic to investigate

the nanometric cutting tool wear in silicon. The simulations have also been used to study the properties of graphene such as nanoscale peeling process of monolayer graphene [124], edge stresses calculations [125], and frictional behavior of mono and few layers of graphene [126, 127].

The simulation studies reported the dynamics of the graphene sheets covering diverse aspects of nanoscale peeling process [124], edge stress calculations of graphene sheets [128], and frictional behavior of carbon nanosheets [126, 127]. Selection of a suitable potential is crucial for carbon related materials due to their bonding nature. The AIREBO and the Tersoff potential functions are widely used to simulate the bonding interaction between the carbon atoms. A large number of molecular dynamics studies used the LAMMPS package with the AIREBO potential for the carbon related materials [109, 110, 125]. The LJ potential has also been used to estimate the adhesion energy between the graphene layers [115] and to predict the diffusion behavior of ad-particle on graphene [129]. Hence, proper study using the simulation technique may provide useful insights that may helpful to control the experimental process.

2.7 Summary

Benchmarking existing graphene manufacturing processes revealed that techniques such as epitaxial growth, unconventional methods-unzipping carbon nanotubes, arc discharge, atomic layer deposition and exfoliation techniques are used predominantly for synthesis of carbon nanosheets. There is very little work in the literature exploring the potential of the mechanical exfoliation to produce carbon nanosheets; this method is restricted only to the laboratory scale synthesis. Given its potential to produce high quality graphene, there are plenty of opportunities to develop it into

an industrial scale method. The nanomachining process is capable of producing ultra-thin layers and this tool based machining technique can be used to fabricate graphene. Molecular dynamic simulations can be used to obtain insights into the mechanical exfoliation process. In the following chapter, a tool based mechanical exfoliation machining process is introduced and the molecular dynamic simulation technique is later applied to understand the mechanics of the process.

Chapter 3

WEDGE BASED MECHANICAL EXFOLIATION (WBME)

As pointed out in the previous chapter, there is an urgent need to develop a reliable fabrication technique to produce carbon nanosheets to realize promising applications that are rapidly being developed. A study of current graphene fabrication techniques highlighted that mechanical exfoliation has been largely ignored as a common fabrication technique and restricted only to laboratory-based research. Earlier published reports indicated that mechanically exfoliated graphene is of better quality compared with graphene obtained using other fabrication techniques. Simultaneously, the field of mechanical machining is being developed as a fabrication method at the nanoscale. The focus of this study is to develop a mechanical exfoliation technique to fabricate the carbon nanosheets with better process control. This study further investigates the detailed morphologies of the cleaved carbon nanosheets obtained using a new mechanical exfoliation technique.

Section 3.1 introduces the proposed wedge-based mechanical exfoliation (WBME) technique. Following this a discussion about material preparation used and the

cleaving process is presented in section 3.2. Section 3.3 presents preliminary characterization results. The following section presents a detailed analysis of the morphologies of the carbon nanosheets, and measured force signatures.

3.1 WBME Technique

Graphite being a layered material, a sharp tool that moves through the inter-layer spacing should be able to separate layers from its bulk. Theoretically, if the tool is sharp enough to initiate a crack, an applied external force will cause the crack to propagate through the layers. As shown in (fig.3.1), it is possible to make use of the inter-layer spacing and complete the cleaving. This process is more similar to a slicing technique. The thickness of the cleaved layers can be controlled by precisely controlling the tool position.

3.2 Material Preparation

Converting the concept idea into a real experimental set-up requires accurate equipment that support the various dedicated functions (fig.3.2). The experimental set-up

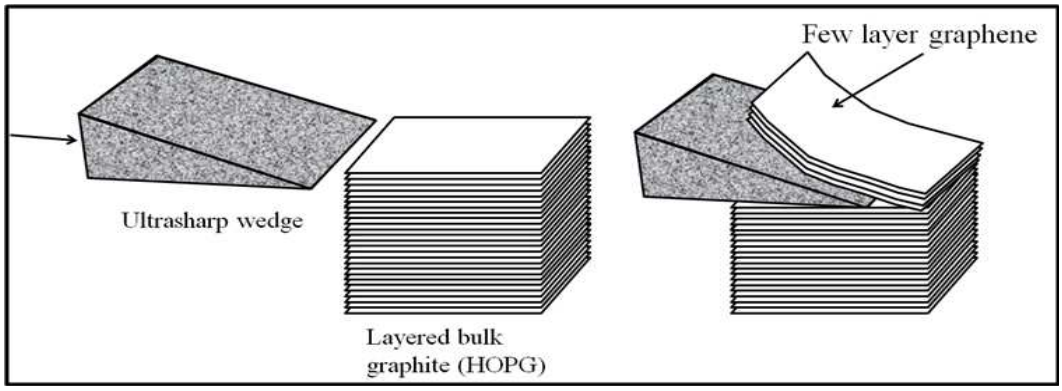

Figure 3.1: The schematic diagram of the WBME

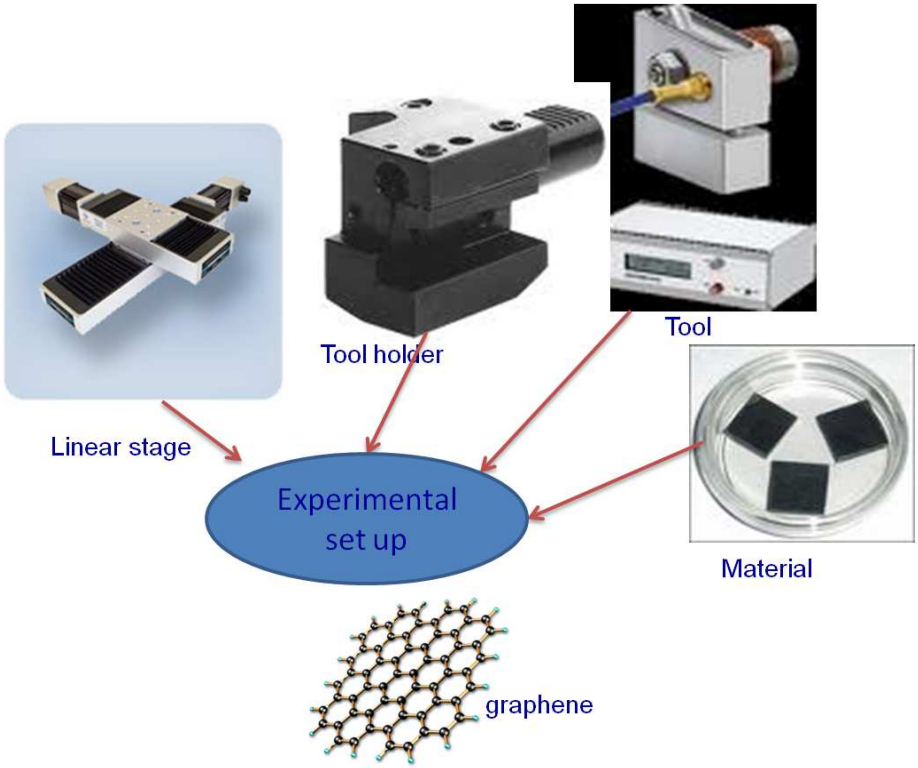

Figure 3.2: Concept converts to a experimental set-up

consists of a piece of HOPG material, a sharp cutting wedge, a wedge holder, and a precision linear stage for positioning of the wedge or the material. Highly ordered pyrolytic graphite is selected as the raw material with dimensions of 2 x 12 x 12 mm. The HOPG is purchased commercially from Structure Probe Inc (SPI- [130]-ZYH grade) and Electron Microscopy Sciences (EMS [131]). As reported in the literature, the HOPG structure (layered) is more closer to natural graphite. The selected sharp cutting wedge is 3 mm in length and is made of single crystal diamond. It has a sharpness of 2 nm which is relatively sharper compared with other commercially available tools. The included angle of the wedge is 35 degrees. A special boat to house a bath of liquid is attached to the wedge. The diamond wedge is mounted on an ultrasonic oscillation system with a capability of providing tunable frequencies in the range 25 to 45 kHz with an amplitude of vibration ranging within a few tens of nanometers. An ultramicrotome is selected as the material holder as well as to

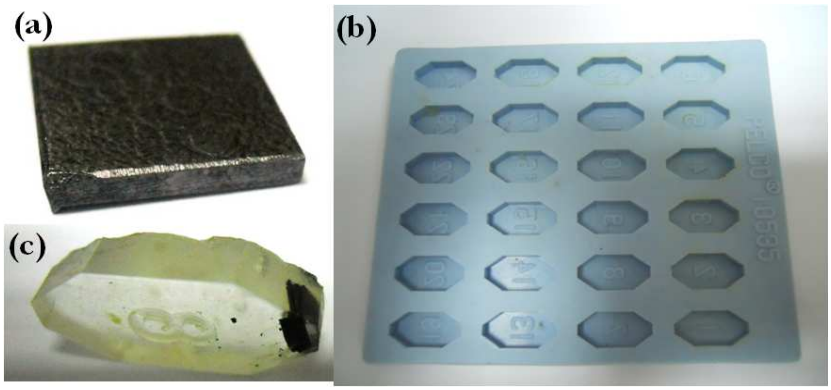

Figure 3.3: Material preparation: (a) HOPG material before processing, (b) Embedding Silicon carbide mold, (c) Material after embedding

provide feed motion. The capability of advancing the cantilever arm with nanometer precision range is a crucial factor in selection of this machine. A separate stage is used to hold the cutting wedge.

The HOPG material (fig.3.3a) is cut into smaller pieces with dimension of 1 x 1 x 2 mm^3 using a sharp blade with extreme care. These smaller pieces are brittle and hence not reliable to fixture directly on the spindle of the ultramicrotome for further processing. Thus, the prepared work material was embedded in an Epofix medium inside a silicon carbide mold (fig.3.3b). The embedding medium is prepared by mixing a resin (Bisphenol-A-Diglycidylether) and a hardener (Triethylenetetramine) in appropriate proportions. The prepared material is placed at the room temperature for 8 hours to cure. The specimen is shown in fig.3.3c.

Next, these prepared work materials are further trimmed as shown in fig.3.4a [63] into a pyramid shape using a trimming (Leica) machine. This machine is used with a diamond-rotating miller. There are several intentions in this trimming action. One is further to reduce the area of the material surface that suits for the sectioning process. The other is to remove the embedded material around the HOPG specimen. Figure 3.4b shows the schematic of the expected pyramid shape and trimmed sample is shown in fig.3.4c. The area of the pyramid surface is controllable. Approximately,

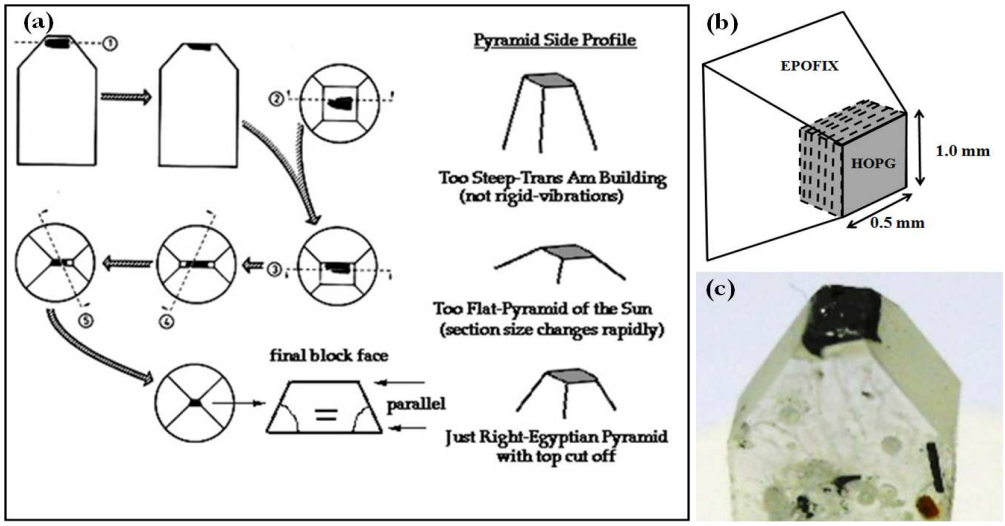

Figure 3.4: Specimen trimming process (a) Trimming process [63], (b) Schematic shape of the trimmed pyramid, (c) Trimmed pyramid-shape sample

the surface area is maintained at 0.5 x 1.0 mm^2. It is possible to extent the material in the direction of length but width has a dependency on the width of the diamond wedge. The next step is to mount the HOPG specimen onto the ultramicrotome holder (fig.3.5a). A special type of spindle head is used and it is capable of rotating within the ultramicrotome cantilever arm. The 90 ^{0} positions are marked (click stop) and spindle can be accurately positioned. Then, the diamond wedge is securely mounted onto the wedge holder (fig.3.5b). A tool setting (clearance angle) is also set during this process. This angle is vital because there should adequate space between the newly generated surface of the specimen and the bottom face of the wedge to avoid any damage to newly generated surface due to the rubbing. The specimen and the wedge mounted setup on the Leica Ultra Cut is shown in fig.3.5c.

Then, the boat is filled with the de-ionized water until a positive meniscus is formed. A syringe is used to control the water level of the boat and level is maintained very close to the edge of the diamond wedge. Soon after, the alignment of the specimen block and the edge of the wedge is carried out. This is an important step to avoid many difficulties later on. At the beginning of this process, the wedge is hold back

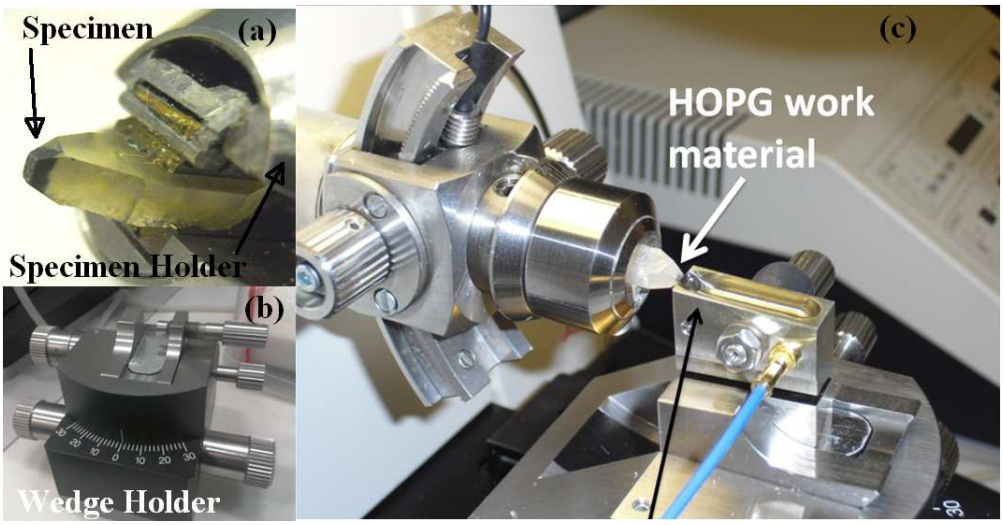

Figure 3.5: Experimental set-up: (a) specimen mounted on the specimen holder after trimming into pyramid shape, (b) wedge holder and (c) specimen and wedge mounted set up.

to avoid the damages to the diamond edge due to any accidental or unexpected movements. Careful advancement of wedge stage projects the edge of the wedge reflection on the specimen surface. The back-light of the ultramicrotome provides this reflection. This reflection can easily be observed through the stereo microscopes attached to the ultramicrotome. The alignment steps are schematically indicated in fig.3.6 [132]. The critical indicator is the knife-edge reflection on the specimen. Figure 3.6a and b, show the correct specimen alignment. The specimen tilt can easily be recognized by the movement of the cantilever arm up and down. When it moves down manually, the space between the edge of the wedge and specimen must be kept constant. This provides the evidence for proper specimen mounting. If there is any specimen tilt, a gap is indicated as seen in fig.3.6c and d. When the specimen gap getting smaller, the specimen should rotate in the clockwise direction or vise-versa, then it should rotate to the anti-clockwise direction. This procedure aligns the vertical plane and surface of the specimen. For a proper alignment, the specimen and the edge of the wedge must be horizontal. If not, the reflection will indicate disorientation as illustrated in fig.3.6e-h. If the left side of the specimen

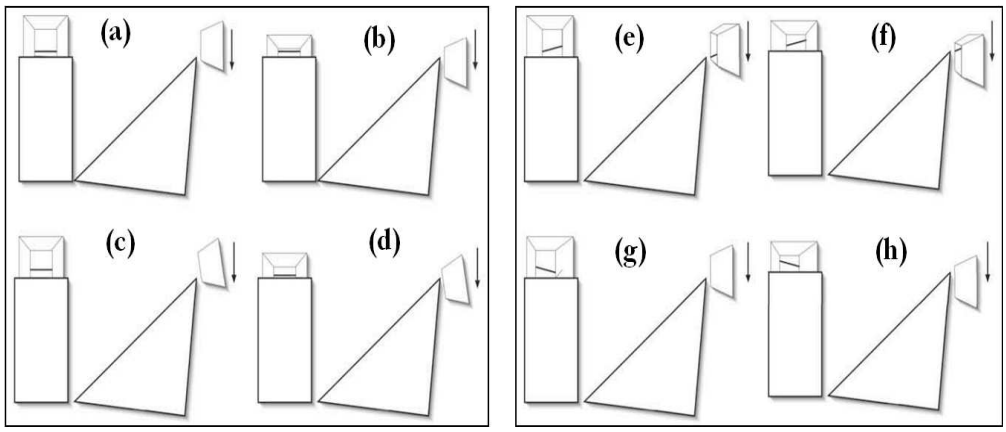

Figure 3.6: Alignment process of wedge and the specimen ; a, b- proper specimen mounting, c, d- specimen tilt, e-h- wedge misorientation [131]

is closer to the wedge (fig.3.6 e and f), then the wedge should be rotated to right side using the wedge holder. If it is vise-versa (fig.3.6g-h), then the wedge must be rotated in the other direction [132]. After performing the proper alignment, the system is ready for cleaving operation. Before beginning of the operation, several parameters such as cutting speeds, and thickness of the cleaved layers have to be set. The control knobs to control the parameters are provided in a separate panel. Then, the sectioning process can be started.

As a practice, first, a larger thickness is set until whole block face is removed. Then, the setting is changed to the required thickness on the section and continued with sectioning. Every experimental run involved a series of 20 cleaving passes. During every pass, a layer is generated. As the wedge retracts and is ready for the next pass, the layer just generated remains adhered to the wedge surface. The subsequent cut generates another layer which pushes the previous layer further onto the wedge and subsequently on to the water bath. When the new layer goes underneath the previous layer or when the layer reaches the water surface, then in some cases curling of the layers is observed. More often than not a series of layers are observed floating on the water bath. Next, the challenging task is to remove them from this water bath. They must be transferred to a substrate for further processing. The floated

layers are first separated by eye lash (fig.3.7a & b [34]). The stereo-microscopes are immensely useful to separate them. The eye-lash is made by an epoxy gluing a piece of hair. A loop attached with a handle (3 mm in diameter) hold over the floating layers as shown in fig.3.7c-f [131]. Due to the surface tension of the water these layers are attached to the water droplets. With this technique, the separated layers can easily be transferred to any substrate. We use different substrate materials. One is a Si substrate coated with 300 nm SiO_2 epi-layer and the other is a copper grid (3.05 diameter and 400 mesh size). The Si substrate provides a better visibility during the optical microscope characterization. The copper grid is essential for transmission electron microscope observations.

3.3 Preliminary Cleaving Results

The initial experiments were performed with the technique demonstrated in the previous section. The ultra-sharp wedge is held fixed while the work material was fed slowly downwards at a controlled speed (0.6 mm/s) towards the wedge. The overlap between the diamond wedge and the HOPG surface was set to 40 nm at this stage. A wedge setting angle of $6\ ^{0}$ were adjusted. Preliminary experiments were performed with and without oscillation on the wedge. Application of oscillation set the parameters of frequency to 33 kHz and voltage to 2.1 V. This particular frequency is very close to the resonance frequency of the wedge system. The cleaved layers slide off the diamond wedge surface, are floated on to a water bath, collected and then transferred to a copper grids for AFM and TEM observations. Raman characterizations are performed on six samples prepared using identical process parameters with a Renishaw Raman microscope (633 nm wavelength).

Under perfect cleaving conditions, we can expect the layer size to be comparable to

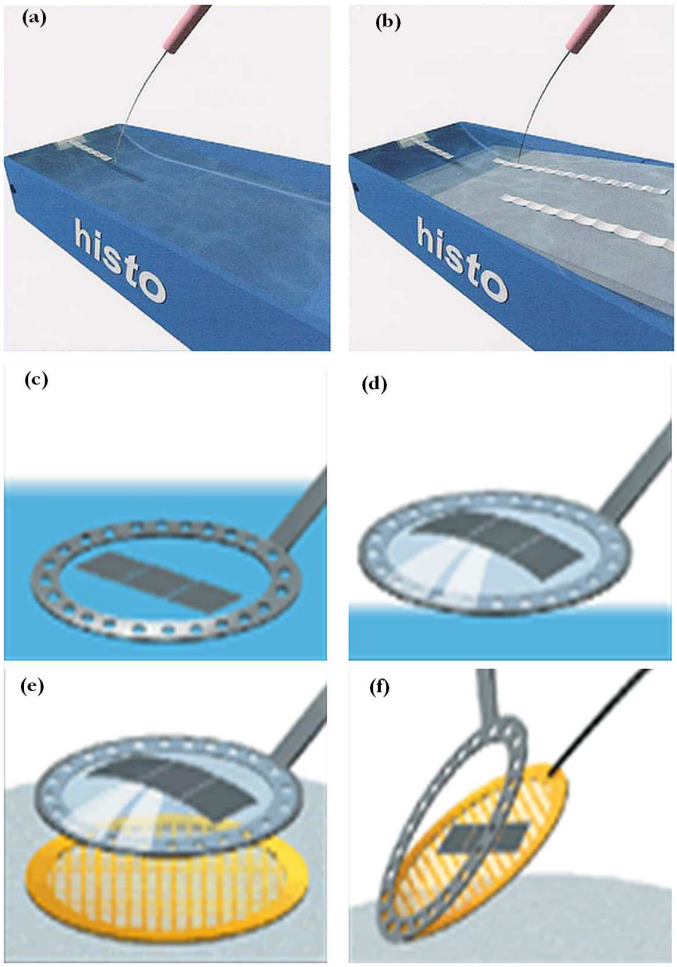

Figure 3.7: Floating layers and separation; (a) Cleave layers floating on the water bath, (b) Floating layers are separated by eye lash [33], (c)-(f) separation of layers and deposited to copper grid [130]

the dimensions of the face of the pyramid (1 x 0.5 mm^2). We were able to observe layers with area of approximately of 900 x 300 μ^2 with a repeatability of more than 50%. The observed layers through the optical microscope are shown in fig.3.8. Layers placed on Si substrate show a inference color (fig.3.8a-c) scheme which is an indication of very thin layers. Small particles are attached on some of the layers as in fig.3.8a. A proper cleaning after the trimming process can considerably avoids this issue. Edge distortions such as tearing and edge folding are clearly visible. The layers placed on top of copper grids do not provide clear appearance (fig.3.8d).

Atomic force microscope operated in the tapping mode is used to determine the

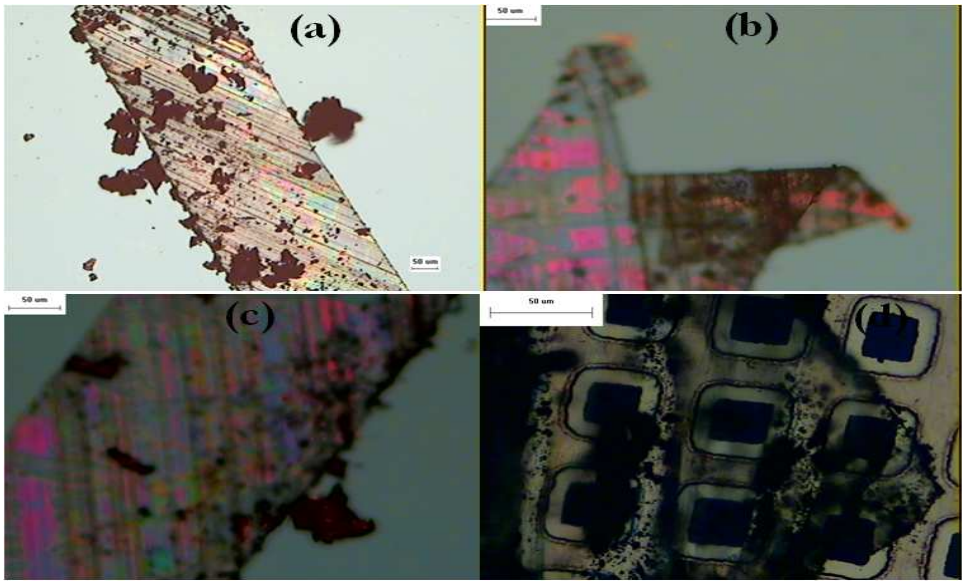

Figure 3.8: Optical microscope images of preliminary layers; (a), (b) and (c) on Si/SiO_2 substrate, (d) on copper grids.

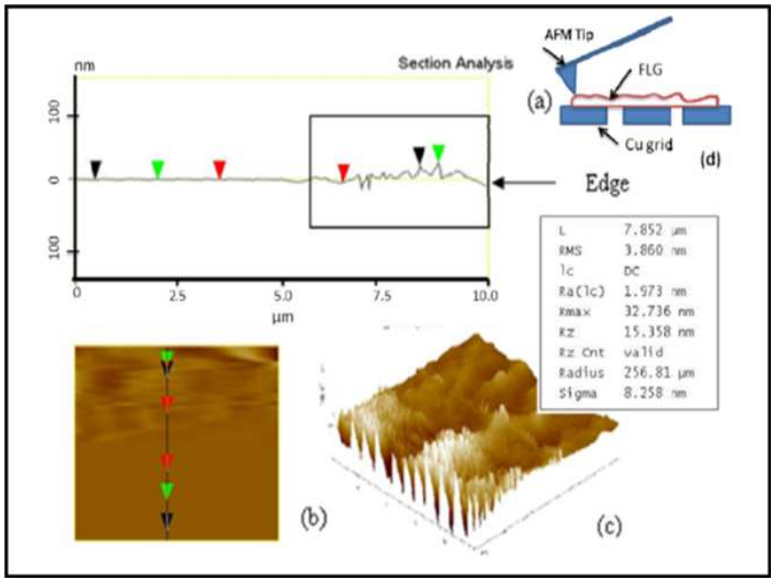

Figure 3.9: Thickness measurement with AFM (a) Sectional analysis of edge, (b) Plane view of edge (c) 3-D topography (d) AFM tip position

thickness of the layers obtained. The sectional analysis (fig.3.9) of this data shows that the layer thickness is in the range of tens of nanometers. It is also seen that the edges of the layers have uneven thickness as shown in fig.3.9a. Figure 3.9b represents the plan view and fig.3.9c shows the topography of a measured area. The focus is given to select the appropriate area on the copper grid. The AFM measurements were taken on both the suspended and non-suspended areas; the edge thickness measurements were made on the non-suspended area as shown in fig.3.9d. The observed crumpling and folding layers on top of each other made much difficult for thickness measurement.

Observations using TEM of the few layers of graphene obtained with and without oscillations are shown in fig.3.10 and fig.3.11 respectively. In the micrographs, of layers without application of oscillations, the folded graphene sheet is clearly visible (marked as 1 & 2). Fig.3.10 shows an area where the sheet appears to be heavily crumpled. In the micrographs of layers obtained with application of oscillations, folded graphene sheets, and smooth areas of the sheets are also clearly observed. In this case several distorted areas are seen and these structures that seem to resemble other nanostructures (like nanoscrolls) can be observed (marked as 3 in the enlarged area), which needs further investigation.

The Raman spectroscopy data of the cleaved layers, produced with and without oscillation indicates several features such as the D band (information about defects), G band (in plane vibration) and 2D band (stacking order); these correlated well with reported data in the literature [9]. There are no differences in the D band positions (1,332 cm^{-1}) with and without oscillations. However, this D band position observed is different from that of bulk graphite (1,355 cm^{-1}). The G band position was 1,577 cm^{-1} with oscillation and 1,578 cm^{-1} without. The Raman data is further analyzed using a curve fitting method involving deconvolution and fitting two Lorentzian

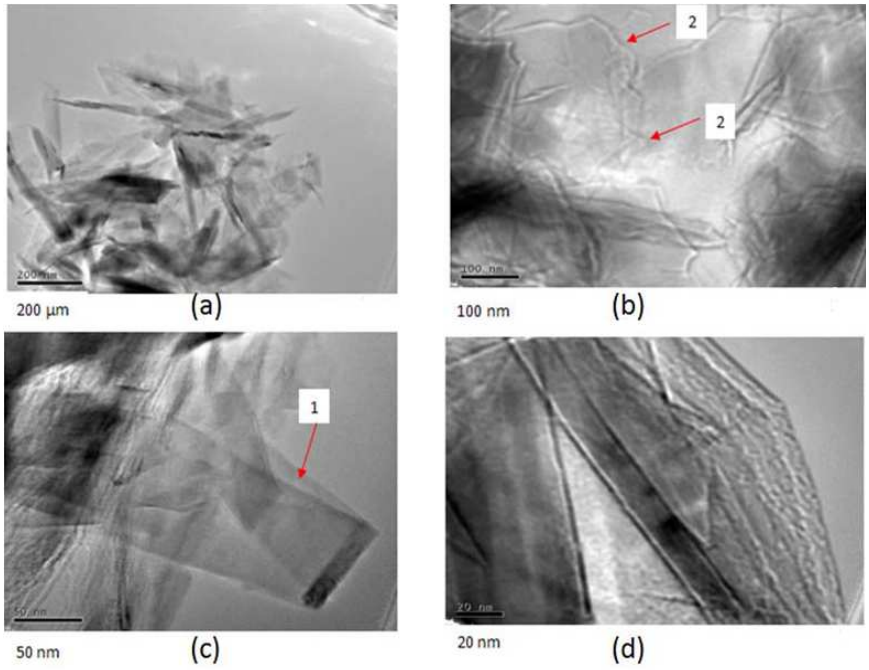

Figure 3.10: TEM images without ultrasonic oscillation (a) Large FLG edges, (b) and (d) folded FLG, (c) large graphene sheet with rolled edge.

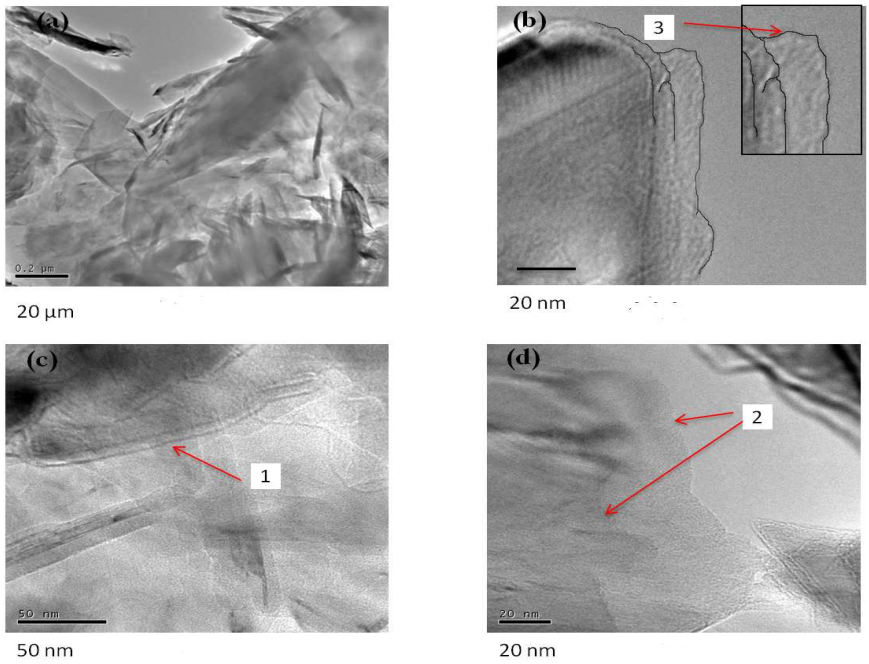

Figure 3.11: TEM images with ultrasonic oscillation (a) Low magnificent image of FLG, (b) Edge of few layers of graphene, (c) and (d) Folded FLG

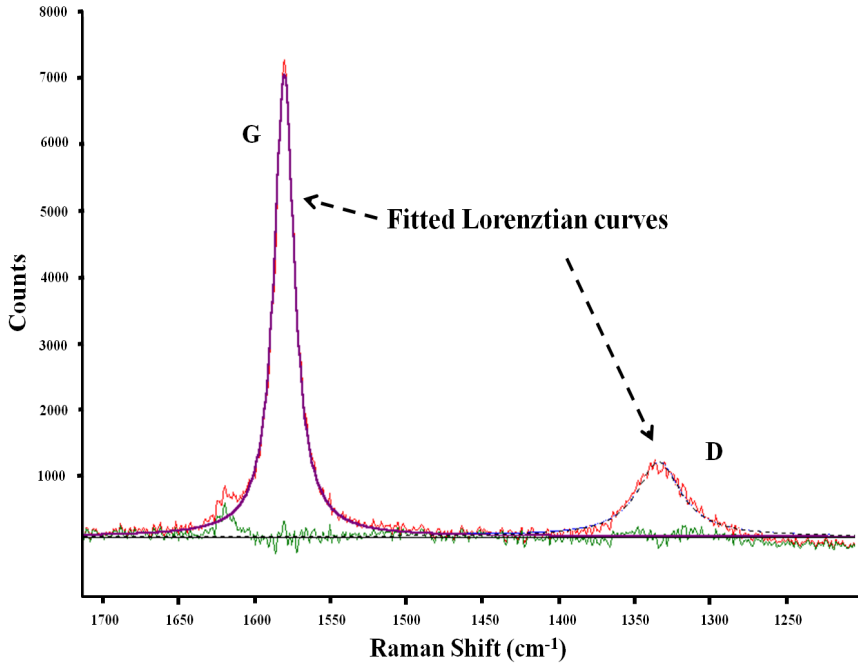

Figure 3.12: Raman spectroscopy data

functions, HOPG being a polycrystalline material [133].

Fig.3.12 shows the fitted curves obtained, from which the ratio of D and G band peak intensities (I_D/I_G) can be obtained. There are two different ways to calculate this I_D/I_G ratio. One method is to obtain it directly from the peak height [134, 135, 135, 136] and the other way is to use the integrated area of the fitted curves [137–139]. Here, both methods are used to analyze the Raman data. The I_D/I_G ratio obtained using both peak height and integrated intensity methods are plotted in fig.3.13a for the six samples. A statistical two-sample t-test conducted on the samples showed that the I_D/I_G ratios for the layers obtained with and without oscillation, calculated using the direct peak height method, were statistically different (p value = 0.031 at 95% confidence); thus oscillation has some distinct effect on the process and the layers obtained.The I_D/I_G ratio of CVD grown and scotch tape exfoliated graphene are compared with the WBME graphne in the table 3.1. The values reported in the literature vary between 0.3 1.4, while our values are in the

Table 3.1: Comparison of I_D/I_G ratios of of CVD, scotch and WBME graphene

Reference	Description	I_D/I_G	Laser (nm)	Calculated Method
Wood .J.D. et al. [140]	CVD,1000 ^{0}C	0.67-0.69	633	Unknown
Zhao . P et al. [141]	CVD,700 ^{0}C	1.4	633	Unknown
Ismach. A.et al. [142]	CVD,1000 ^{0}C	0.3 -0.9	532	I. Intensity
	HOPG	0.25	514	Unknown
Ni. Z. H et. al. [143]	Scotch Tape Graphene	0.3	532	Unknown
Thesis	WBME	0.2-0.35 0.6-1.2	633 633	Peak Height I. Intensity

range of 0.2 1.2, depending on how the ratio is determined. It can thus be concluded that our graphene layers and that grown using CVD grown have comparable values.

The I_D/I_G ratios can also be used to calculate the crystallite size. The average crystallite size (La) and excitation laser energy both are correlated with I_D/I_G ratio. There are different equations reported in the literature to estimate La. The original equation determined by Tuinstra and Koenig [134] is said to be not appropriate for all graphite forms. Hence, a general formula for La involving any excitation energy, E, was proposed by Canado et al. [137] as shown in equation 3.1.

$$La = \frac{560 \times \left(\frac{I_G}{I_D}\right)}{E^4} \tag{3.1}$$

The values of La calculated using this equation and experimentally obtained values of I_D/I_G are plotted as shown in fig.3.13b. It appears that La is smaller when ultrasonic oscillation is applied to the wedge. The value of La is inversely proportional to amount of crystal boundary and is a measure of dislocations, vacancies, as well as number of non-graphitic atoms, which in turn is proportional to chemical functionality and shear strength of linkages [135]. The amount of disorder is an indication of fraction sp^2 bond and it is a measure of electrical, mechanical, and

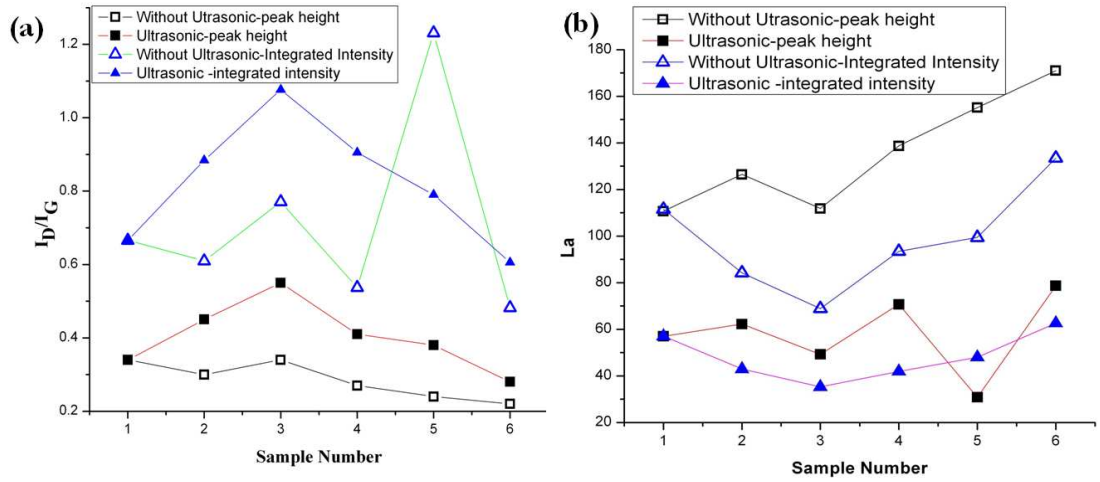

Figure 3.13: Calculation of L_a using experimentally obtained values of I_D/I_G; (a) I_D/I_G ratio obtained by both direct peak height measurement and using integrated area method. (b) The L_a values calculated using both these methods is plotted

optical properties. The lower value of La when oscillations are applied indicates the improved quality of the layers obtained. Also, the higher the value of La, the lower the shear strength. Thus, from fig.3.13 , if can be conclude that shear strength tends to increase when ultrasonic oscillation is applied.

This preliminary study opens up many interesting questions. It proves that the technique is capable of producing ultra-thin carbon nanosheets together with different variations. It requires further detailed investigations on the technique and the controlling parameters. Next section reports the further in depth analysis of various structures. As reported in the previous section, the morphologies of the cleaved layers are an interesting subject for further study.

3.4 Detailed Characterization of Carbon Nanosheets

In this section, we examine and report here the nature of layers produced by this technique and factors that contribute to layer-defects and process signatures. The emphasis here is on characterizing the ultra-thin layers obtained by oriented mi-

crotome sectioning (chapter 2) at varying levels of magnification using optical microscope, field emission scanning electron microscope (FESEM), and transmission electron microscope (TEM). Particularly, we identify the various nanostructures generated with this technique. The sectioning forces are also measured to analyze their relationship to the sectioning mechanism. We also report pre-existing defects in the HOPG and its effect on the layers obtained and measured force signatures. The force signature analysis together with a basic understanding of the sectioning mechanism will help towards advancing this technique for fabrication of thin graphitic films.

We start our investigation by examining the structure of the as-purchased unsectioned HOPG for any pre-existing defects. On the sidewalls of the HOPG, striation marks are observed (fig.3.14a) and these marks are left behind by the process originally used by the vendor to cut the HOPG blocks to the required size. The enlarged area of the surface shows presence of powdered particles attached to the surface fig.3.14b. To remove these particles and to enable viewing the bulk structure of the HOPG an adhesive tape is used to perform several peelings on the sidewall; the peeled HOPG sidewalls are then observed in an FESEM. As shown in fig.3.14c, several defects such as kinks (indicated as circle 1), discontinuous layers (circle 2), and voids are noticed. Surprisingly, the layers seem to be bunched together. In certain areas, heavily distorted layers (fig.3.14d) are also observed. We also performed several adhesive peelings to clean the top surface of the HOPG and observed them for the presence of any pre-existing defects/structures. Defects such as cleavage steps, wrinkles, and folded-over flakes are readily visible similar to that reported in the literature [144]. These observations of pre-existing defects in the HOPG need to be taken into account when studying the structure and morphology of the layers obtained after sectioning.

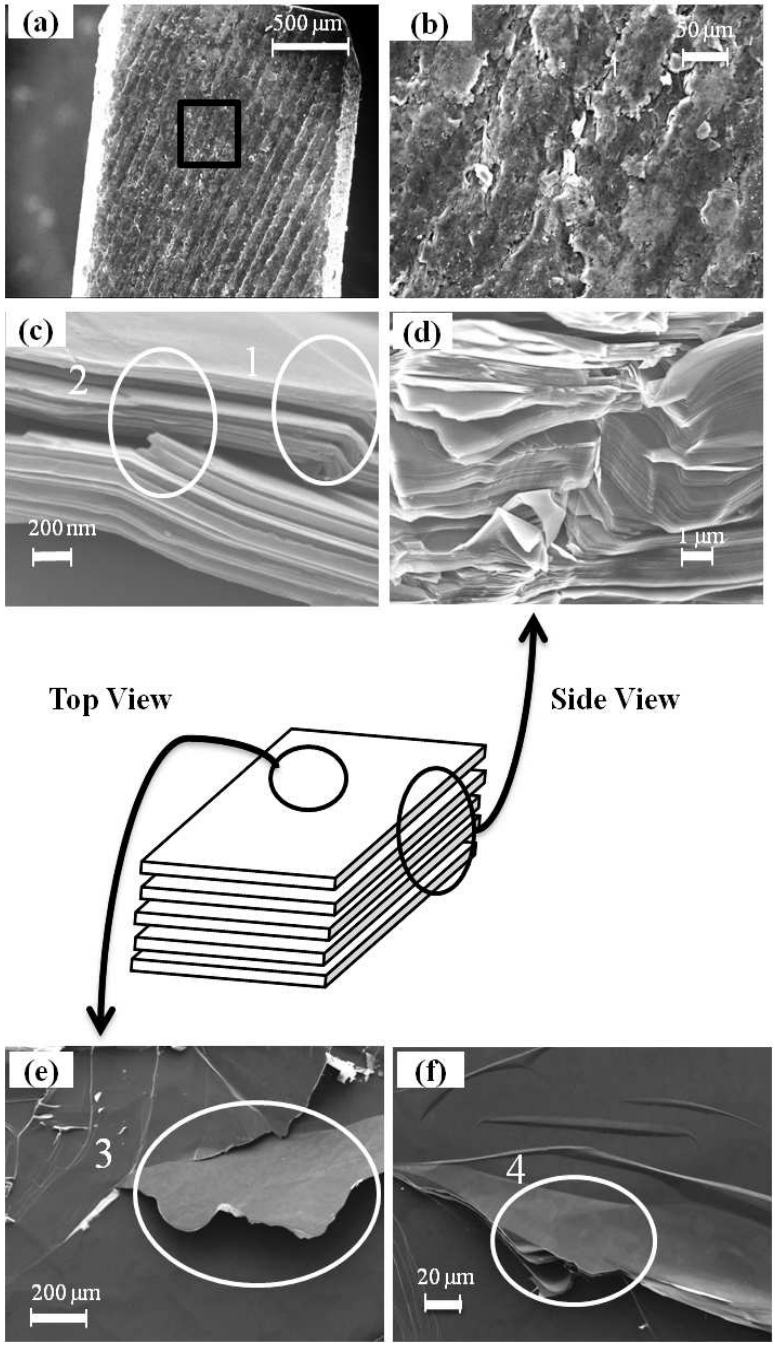

Figure 3.14: Pre-existing defects in HOPG prior to sectioning; (a) Sidewalls of the as received HOPG material show parallel striation marks, (b) Enlarged view of HOPG sidewalls showing presence of powered material, (c) Kinks (circle 1) and discontinuous layers (circle 2) seen on the sidewalls after adhesive tape peelings to remove the powered layer, (d) Distorted layers can also be seen on some side wall locations, (e) Cleavage step, (f) Wrinkles on the top surface of the HOPG after several peelings.

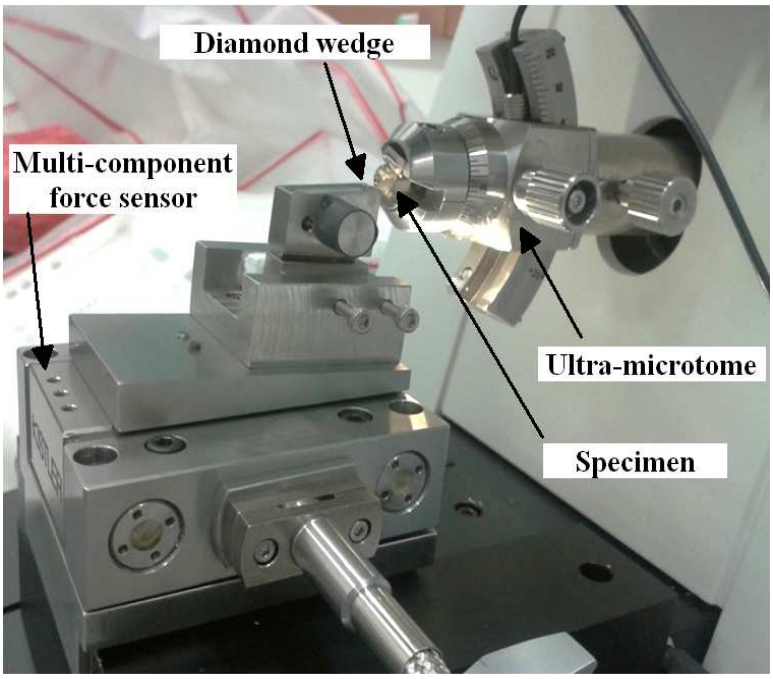

Figure 3.15: The experimental setup for force measurement; The HOPG sample is mounted on the moving stage of the ultramicrotome while the wedge is mounted on a force sensor held on the fixed portion of the microtome. The force sensor detects sectioning forces.

As reported in section 3.2, same material preparation technique is adhered to. The sample is prepared taking into account layer orientations. The trimmed small pieces are placed in an embedding mould in such a way that layers are arranged in a vertical direction. In this set of experiments we tested several process parameters by changing the sectioning speed in the range of 1-5 mm/s and the section thickness in the range of 10-40 nm (thin sections) and 500 nm (thick sections). The wedge-setting angle is held constant at 49 ^{0}. Sectioned layers are transferred onto same substrates for detailed characterization. A multi-component force sensor (Kistler C9256) detects forces experienced during sectioning(fig.3.15). A custom-made fixture holds the wedge directly on the force sensor at an inclination angle of 60 ^{0} thus providing clearance to the HOPG surface being sectioned.

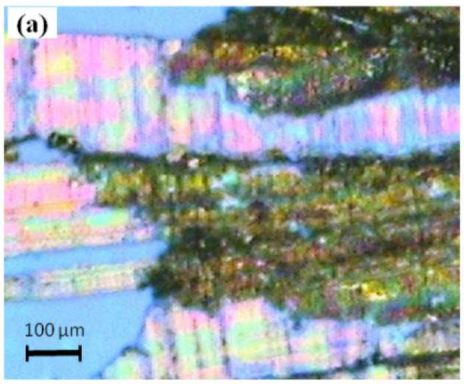

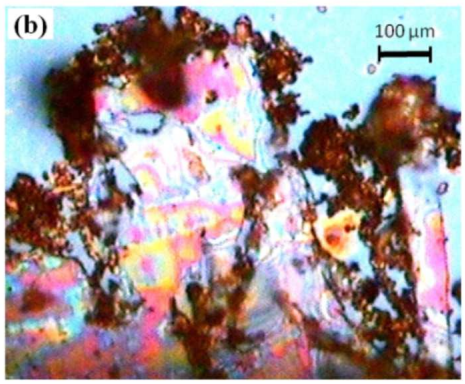

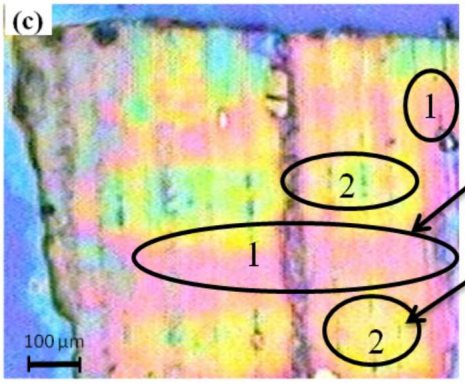

(d) Thickness and colour variation

Colour	Thickness	Reference
Blue	Less than 3 nm	[145]
Pink		
Purpule		
Yellow	Tens of nanometers	[146]

Figure 3.16: Optical microscope images of thin section layer morphologies: (a) Flat and several folded layers showing the thickness variations in colors, (b) Carbon particles attached to the edge of the layers (c) Enlarged image of a single continuous layer. The marked regions of 1shows pink color that indicate thickness less than 5 nm, and 2 shows yellow color regions represent the thicker (tens of nanometers) sections

3.4.1 Qualitative Analysis of Sectioned Layers with Optical Microscope, FESEM and TEM

Similar to earlier discussion we start our characterization with the optical microscope.

Optical microscopy (thin sections): Images from optical microscopy (Zeiss Axioskop 2 mat) are shown in fig.3.16. The microscope uses a 12 V, 100 W halogen illuminator and was operated in the transmited mode.The first notable observation is the shape and size of the cleaved layers. As similar to preliminary study, even though we expect the area of the cleaved layers to be equal to the area of the sample

it is not the case for the sectioned layers observed the layers are smaller than the sample area. This may be due to partial cleaving resulting from uneven material surface and possible misalignment between the block and the wedge. The layers exhibit various colours mainly due to thickness variations [145]. As reported in the literature blue, pink, and purple color patches indicate very thin layer sections and approximately the thickness is less than 3 nm [146]. The yellow patches indicates relatively thicker regions [147]. These thin regions are marked as 1 and the thicker regions as 2 in fig.3.16. Considering the position of these regions, it is difficult to perform AFM type of measurement to grantee the thickness. This visual aid provides a clear indication on thin regions on the cleaved layers. Damages are also noticeable on the edge of the layers. Separated and folded layers are also observed clearly (fig.3.16). During the experiments, we collected the layers after sequential sectioning performed continuously several times. We use water as a supporting medium to allow layers to float and to avoid the layer contacting the wedge surface. If there is a gap between the edge of the wedge and the water then the cleaved layers may contact the wedge surface causing folding and overlaps. Friction on the wedge surface may also contribute to the folding. As reported in previous studies [148], we interested to see the presence of any deformations or sectioning artifacts. The layers we observed (fig.3.16a), are very thin and due to the reflecting colours it is difficult to discern the presence of artifacts. However, the images clearly indicate that the edges have undergone severe deformations. Carbon particles are also visible at the edges of the layers in fig.3.16b: this is reported as a type of defect in the literature [144]. Fig.3.16c shows continuous unfolded thin layers of graphite seen among the samples.

Optical microscopy (thick sections) (fig.3.17): Layers obtained by a single sectioning stroke with section thickness of 500 nm were collected and transferred to copper grids. By performing this single stroke of sectioning, we avoid the folding of two consecutive layers seen earlier. The thick layers show signs of several mechanical

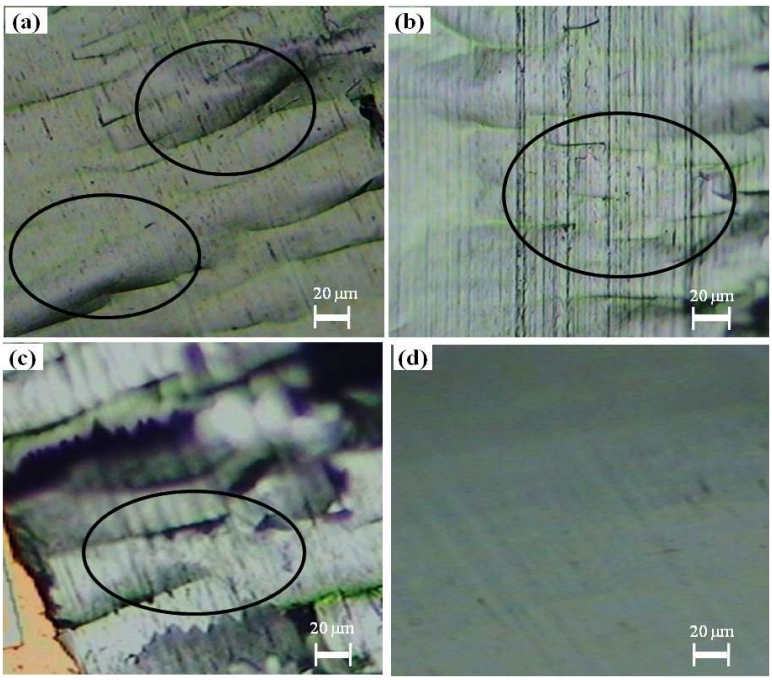

Figure 3.17: Optical microscope images of thick sections; (a) Suspected deformed graphite-stand regions, (b) Wedge marks (c) Tearing marks, (d) Large areaflat region without any folds or defects.

deformations (fig.3.17a). The layers appear crumpled and some features look like a graphite stand another type of defect reported in the literature [144]. A number of suspected wedge (cutting) marks (circled in fig.3.17b and c) and tearing marks are also seen on the cleaved layers. These marks are caused by the edge roughness of the wedge. Similar wedge marks are also observed with other materials sectioned using a microtome [61]. As shown in fig.3.17d, large flat surface areas are also visible.

FESEM observations : FEMSEM micrographs (fig.3.18) indicate the existence of various types of layer morphologies. A stack of sheared as well as laterally displaced and folded layers can be seen in fig.3.18a and fig.3.18b respectively. The sectioned layers show the presence of several types of kinks (fig.3.18c & d). The shape of these kinks are similar to that reported in the literature [149] where mechanical exfoliation using an adhesive tape was performed. The step and peak capped shape kinks are evident in fig.3.18c, and d. The edges appear to be shifted in the step kinks. Such

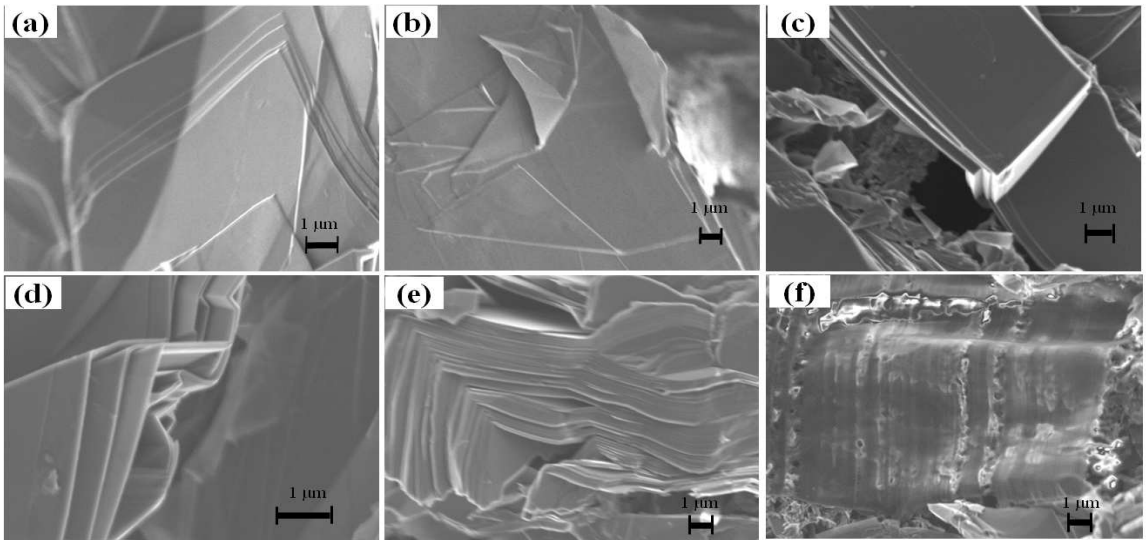

Figure 3.18: FESEM images of sectioned layers: (a) Sheared layers, (b) Folded layers (c) Step shaped kink, (d) Peak-cap shaped kink (e) Crumpled layers with sharp folds

kinks can form in several ways. Kinks can pre-exist in the as-received HOPG, or can form either during the material preparation process or during the sectioning process itself. It is not known whether one or all these steps created the kinks. We already reported in the previous section the presence of pre-existing kinks in the as-received HOPG. During the material preparation, the larger HOPG sample is cut into smaller pieces for embedding in epoxy, and trimming of the embedded HOPG can cause kink formation. The pre-existing kinks in HOPG (fig.3.16c & d) can also be transferred as-is to the sectioned layers. Kinks can also form during the sectioning process. During sectioning, the graphene layers are subjected to large deformations as the moving wedge applies a force parallel to the basal plane of the graphene layers. The weak van der Waals interaction between the layers and weak bending rigidity can lead to deformations under such conditions. Similar deformations have been reported to cause delamination of grains and formation of shear and kink bands in layered hexagonal materials such as Ti_3SiC_2 [150–152]. Another study, on Ti_3SiC_2 aslo, reported [153] a similar type of kink formation caused by grain buckling or bending under compression. Compression-induced heavily crumpled

layers with sharp folds in stacks of layers are also seen in fig.3.18e. Understanding these structures and their formation can provide useful information to control the exfoliation process.

Figure 3.19a shows flat and sheared layers. A tearing layer is observed and it is folded back onto its surface as in fig.3.19b. The kinks (fig.3.19c, d), observed earlier at lower magnifications with FESEM, are clearly visible here and kinked layers appear to be sheared and slid out. Other types of curvilinear shapes were also observed as shown in fig.3.19e-h. These are clearly multiple layered and some of them appear to be bent into various shapes such as S (fig.3.19f). Another group of layers appear partially rolled and slid out along their axis (fig.3.19g, h). Such layer shapes are important to many applications, for example the use of rolled carbon sheets as nanoactuators and energy storages [154, 155]. The conditions that lead to the formation of such rolled structures are yet unknown. We speculate later that the exfoliation process can cause such structures to form. As reported in the literature [144], several defects such as cleavage steps, fold-over sheets are also noticeable.

FESEM images of the HOPG specimen surface: After sectioning the sample under various conditions, we observed the sample surface itself in an FESEM (fig.3.20). The surface is not smooth with uneven surface features present. After performing one set of experiments, we section the material for adequate number of times to remove the uneven surface marks, before proceeding to the next set of experiments. The enlarged image of a portion of another sectioned specimen surface shows the presence of wedge marks (fig.3.20c); similar wedge marks were seen earlier on the sectioned layers. These wedge marks can easily be transferred on to the sectioned layers as well. Re-sharpening the edge of the wedge will remove these appeared marks on the both substrate and the sectioned layers. Fig.3.20d shows discontinuous regions on the surface of the HOPG specimen; these could be crystal-

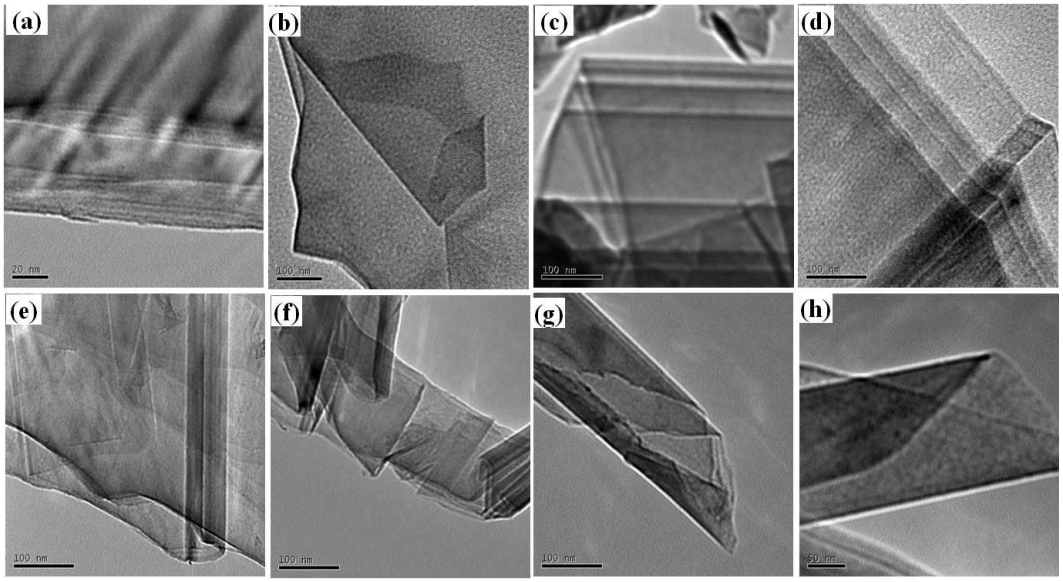

Figure 3.19: TEM Images of sectioned layer morphologies; (a) Flat and sheared layers, (b) Torn layers, (c) and (d) Kinks, (e) and (f) Multiple bent layers, (g) and (h) Partially rolled and axially slid out structures.

lite regions or cracked areas. The sectioned layers are likely to get discontinuous at these regions.

The questions arises as to how these layers and structures produced by the oriented sectioning compare with results previously reported by performing unoriented sectioning on natural graphite and synthetic graphite? The effects of orientations during sectioning were indeed speculated and discussed with different structures expected in oriented sections compared to non-oriented ones [67], but no particular effort was made to improve orientation and study its effects. While flat layers were previously seen in unoriented sectioning micrographs [66, 67], we expect to see more such regions in oriented sectioning since the layers tend to cleave better. While presence of rolled sections (called cigar like) were reported in earlier unoriented sections [67] but clear evidence was not presented. We suspect that the wedge bluntness in combination with the orientation alignment causes the edges to roll up more frequently and thus are more evident in oriented sectioning. Similarly, the presence of sheared layers in unoriented sections was conjectured but no evidences

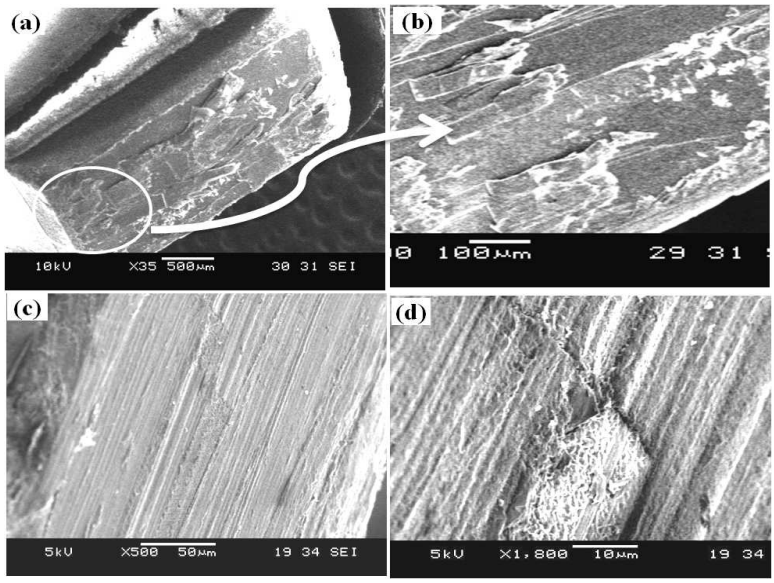

Figure 3.20: The surface of HOPG after sectioning; (a) Uneven surface after sectioning, (b) Enlarged image indicating patches of cleaved regions, (c) Enlarge image of a sectioned surface indicating wedge marks, (d) Cracked regions on the HOPG surface where cleaved sections are torn at this point.

were provided [67]. Such shearing in oriented sectioning is likely to be easier because of the orientation of the layers with respect to the wedge with the wedge displacing the layers especially during exit. In addition, no evidence of kinks was shown in previous unoriented microtome type sectioning. It is not immediately clear if oriented sectioning facilitates kink formation. We speculate that the ease of layer shearing in oriented sectioning can also contribute to kink formation. We should note here that kinks, similar to what we report here, are also reported in layers obtained by tape-based mechanical peeling [149] though the fundamental mechanisms of layer separation are different here.

This study provides an understanding of the nature of layers produced by oriented sectioning. It is evident that the sectioning and the sample preparation technique intern, can create several defects such as kinks, cleavage steps, ridge, folded over layers, and broken pieces. The cutting edge itself contributes to the tearing and wedge marks on the layers. This study provides some clues as to the factors that influence

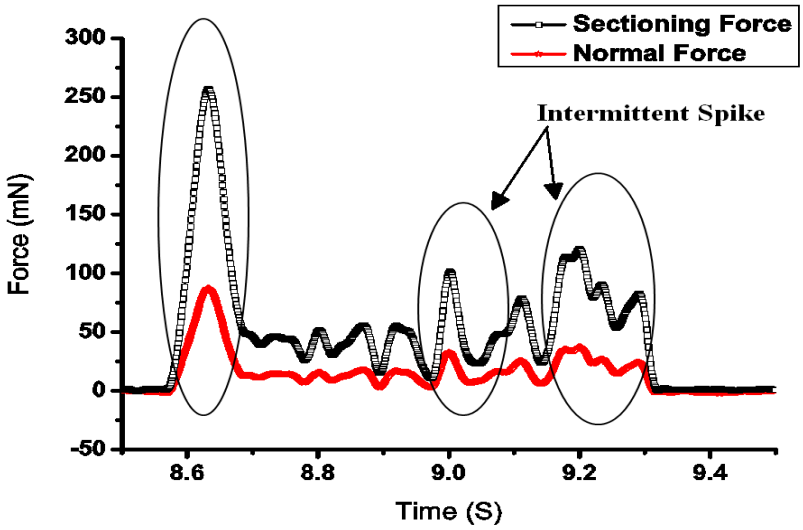

Figure 3.21: Sectioning and normal force trends with time. Several intermittent force-peaks were observed during the sectioning process. The first peak is due to the wedge and material engagement, while subsequent peaks could be caused by pre-existing defects.

the formation of various layer structures and that can avoid defect formation. Key sectioning process characteristics such as energy/forces involved can further indicate sectioning mechanisms and nature of the layer formation. In the next section, the measured sectioning forces, characteristic patterns, the effect of pre-existing defects, and their interactions with the moving wedge during sectioning will be investigated. We expect the characteristics of the energy and forces involved in the sectioning to change in the presence of defects.

3.5 Sectioning Force Signature

The recorded sectioning forces, for a particular sectioning condition, are shown in fig.3.21; similar force profiles were seen at other sectioning conditions. The forces acting along and perpendicular to the wedge movement are termed as sectioning and normal forces respectively. The sectioning force profile show several spikes

during the process. The first spike is at the beginning of sectioning and subsequent spikes appear as sectioning progresses. The initial spike is caused by the wedge and material engagement as the layers resist the advancing wedge. This is considered as the point of initiation of cleavage. The initiation causes a rapid increase followed by a rapid decrease in force without reaching a steady state thus indicating a significant force required at the beginning of the process and further wedge penetration requires smaller forces to overcome the van der Waals interactions. The normal force shows a similar trend as the sectioning force but with a reduced magnitude. The normal force is caused by wedge pressing on the substrate. The subsequent spikes seen in the force profiles could be due to interaction between defects in the HOPG layers and the moving wedge. FESEM observations of HOPG sidewalls prior to sectioning showed various types of imperfections. These imperfections may contribute to the subtle changes in how the wedge causes the layers to cleave. Here, we hypothesize that the spikes subsequent to the first one may be due to the presence of discontinuous layers (fig.3.14c), a pre-existing defect in the HOPG. We confirm this hypothesis by presenting molecular simulation studies (in chapter 4) since in-situ observation of cleaving under high magnifications was not possible. From these experiments, the average cleaving and vertical unit forces of the wedge material interface are calculated as 20 and 1.3 N/mm x10^2 respectively.

3.6 Summary

We have demonstrated a novel mechanical exfoliation technique to produce carbon nanosheets from HOPG using an ultra sharp diamond wedge. Preliminary studies of AFM measurements indicated that the proposed mechanical cleaving method is capable of producing thin layer graphene with a thickness of tens of nanometers. This was further confirmed with color code studying by placing cleaned layers on $Si0_2$

surface. TEM studies revealed that considerable amount of attention is required to understand the edge formation since obtaining structures resembling other nanostuructures were observed. Application of ultrasonic vibrations along the tool edge was observed to significantly reduce I_D/I_G ratios in Raman spectrum. Hence, the applied oscillations may have potential to reduce defects in cleaved layers. The application of ultrasonic vibration also appeared to reduce the crystallite size.

Observing the sidewalls of the as-received HOPG indicated the presence of several pre-existing defects such as discontinuous layers and kinks. Characterization of the sectioned layers at various levels of magnification revealed the presence of various shapes and structures. From optical micrographs of the sectioned layers, we observed colored (evidence of thin sections), flat and distorted layers. Some of the sectioned layers appeared to be folded with dust type carbon particles attached. A closer FESEM examination showed the presence of sheared and flat layers as well as two types of kinks peak cap and step shape. Heavily crumpled and distorted sections were also observed among the cleaved sections. TEM micrographs confirmed the presence of flat, folded and torn structures. Several types of rolled sheets were also noticed. Besides the sectioned layers, examination of the sectioned HOPG surface indicated uneven surface contours and cutting artifacts. Experimental sectioning forces indicated the presence of several intermittent force peaks.

Chapter 4

FACTORS AFFECTING WBME - A MOLECULAR SIMULATION STUDY

4.1 Background

A wedge based mechanical exfoliation (WBME) technique (fig.4.1a) was proposed and tested to produce carbon nanosheets in the previous chapter. The layers produced had various interesting structures: flat, rolled, sheared layers (fig.4.1b-d). The experimental conditions such as depth of insertion (DOI), rake angle, clearance angle, and cleaving speed can be controlled in this process. Close observation of uncleaned HOPG indicates presence of features such as discontinuous layers, kinks (after cleaning), and several distorted layers on the side surface. The measured force signatures showed high initial peak at the beginning and several other intermittent peaks appearing as the wedge advanced. These observations have led us to ask the question of how this folding and sliding of the layers are caused by the action of

the moving wedge. The WBME technique can be better controlled if the nature of separation initiated by the wedge is well understood. Since it is not easy to make in-situ observation during the exfoliation we have resorted to the use of molecular dynamic simulations to study the process. Here we report, using molecular dynamics simulation studies, how and under what conditions graphene layers separate, fold and shear during the wedge-based mechanical exfoliation machining technique to produce few layers of graphene. Section 4.1 describes the details of the molecular dynamic model used. Then, the simulation results related to separation, folding, and shearing phenomena during the process are discussed. Subsequently we try and understand how the force spikes appear during wedge advancement. Section 4.5 then presents the effect of wedge radius on the initial wedge-material engagement. The last section of the chapter describes the effect of application of oscillation to the WBME process.

4.2 Simulation Model

We first modeled single layer of graphene sheet using the selected Large-scale Atomic / Molecular Massively Parallel Simulator (LAMMPS) software [109]. The sheet is built considering the atomic positions of the graphene unit cell (fig.4.2 [156]). The customized *metal* unit system was selected to model the a single-layer zigzag graphene sheet. The simulation box is bounded by 0-103.987, 0-30.2471, 0-3.4 (A^0), in the X, Y, and Z directions respectively. A total number of 1213 atoms per sheet were included in the model. Periodic boundary conditions were applied.

In this model, we used the well established Adaptive Intermolecular Reactive Empirical Bond Order (AIREBO) potential that is available in the LAMMPS. This potential function has been developed to model the hydrocarbon systems. The

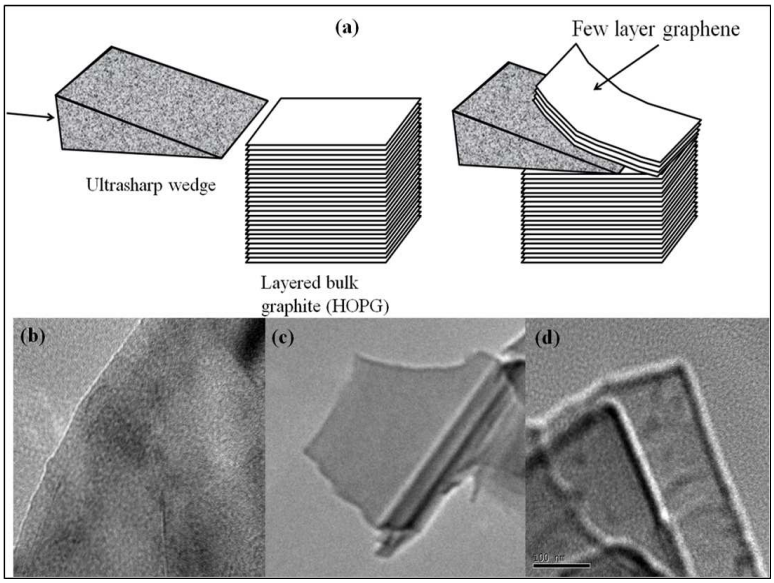

Figure 4.1: (a) Schematic diagram for wedge based mechanical exfoliation of few layers of graphene, TEM image of flat separated (b), folding (c) and sheared (d) few layers of graphene.

potential energy in this system is expressed as in equation 4.1:

$$E = \frac{1}{2}\sum_{i}\sum_{j\neq i}[E_{ij}^{REBO} + E_{ij}^{LJ} + \sum_{k\neq i,j}\sum_{l\neq i,j,k} E_{kijl}{}^{TORSION}] \tag{4.1}$$

where E_{ij} is the pair potential between the atoms i and j. The term E^{REBO} represents short-range (typically less than 2A ^{0}) interactions among C-C atoms while the long-

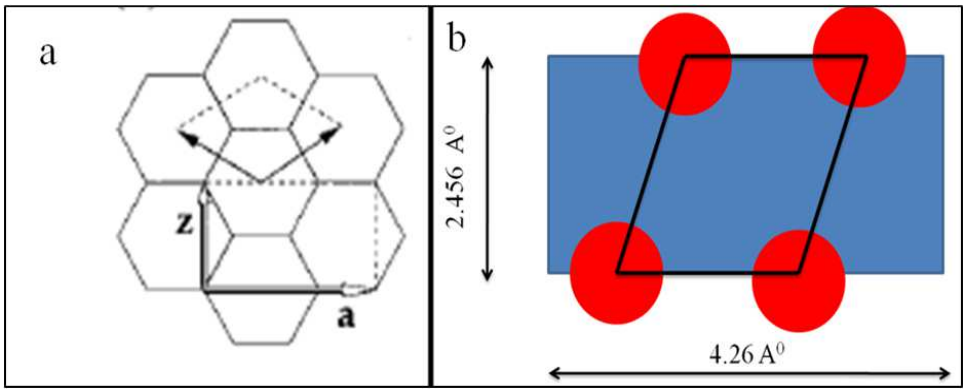

Figure 4.2: (a) Graphene unit cell [151], b) Atom position used for building the model

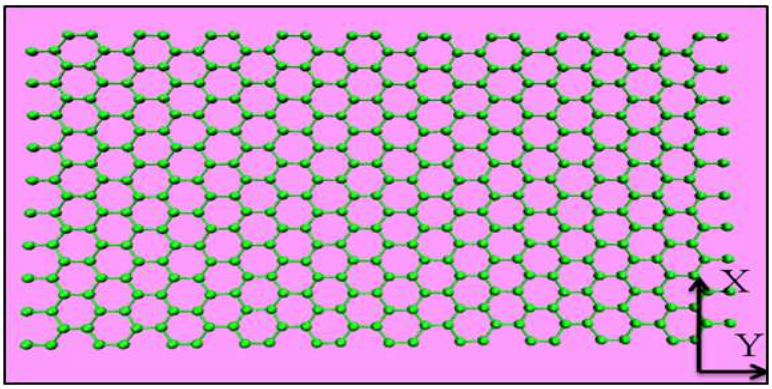

Figure 4.3: Model single layer graphene sheet

range interactions are modeled by the term E^{LJ}. The $E^{TORSION}$ is the energy contributed by the various dihedral angles. The interaction between work material and wedge is represented by the Lenard Jones potential and its energy is given by equation 4.2:

$$E^{LJ} = 4C\left\{\left(\frac{\sigma}{r}\right)^{12} - \left(\frac{\sigma}{r}\right)^{6}\right\}, r < Rc, \tag{4.2}$$

where R_c is the cutoff value and r is the distance between atoms (C= 0.00284, σ=3.4 A ^{0} [157]). The necessary outputs such as potential energy, temperature, total energy, stresses in each direction are written to an output file as the simulation gets completed. The output file is visualized with the assistance of the visual molecular dynamics (VMD) software [158]. A modeled single-sheet of graphene is shown in fig.4.3.

To verify the modeled single-sheet, an uni-axial tension test was simulated to calculate its Young's modulus. To simulate the tension test, the equilibrium was attained with NVT conditions, and a uniaxial strain of (0.001/ps) was applied with a constant temperature condition using a Berdersen thermostat. The time used step was 0.001 ps throughout the simulation. The tension was applied in the Y direction. From the output file, the stress-strain diagrams were plotted to calculate the Young's modu-

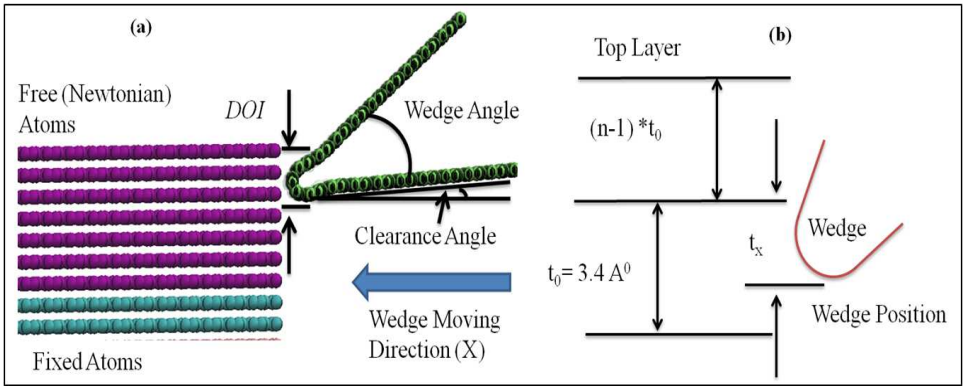

Figure 4.4: Simulation model; (a) Schematic diagram of the MD simulation model; the work material is composed of fixed boundary layers (cyan), and free layers (purple). The wedge (green) is modeled as a rigid object. With appropriate wedge and clearance angles close to the diamond wedge used in the experiments, (b) Schematic diagram of wedge position between layers; t_o the distance between immediate two layers, t_x the distance from the immediate top layer to the bottom of wedge atom.

lus. We repeated the similar test several times and the calculated Young's modulus is in the range of 0.8-1.0 TPa. The obtained modulus values are compared with the literature reported values (table 4.1). It can thus be concluded that the model developed (AIREBO potential values, boundary conditions etc.) are validated and that the model can now be used for further simulation studies.

A schematic diagram of the WBME simulation model is shown in fig.4.4a. This model consists of two components namely a graphite block (HOPG) modeled as a stack of graphene layers (hexagonally arranged atoms), and a rigid wedge. To

Table 4.1: Young's modulus value of graphene reported in the literature

Value of Young's modulus	Method
1.00 [159]	Nano-indenting (experimental)
1.05 [160]	Density Functional Theory
1.11 [161]	Ab initio calculations
1.24 [162]	Density Functional Theory
1.27 [163]	Non orthogonal tight binding
0.94 [164]	Molecular mechanics
0.86 [165]	Molecular dynamics

simplify the diamond wedge geometry, we have a used single-sheet of graphene bent with a fixed included (wedge) angle of 35 ^{0} and an edge radius of 2.4 A^0. All the atomic positions are seized to represent the rigid wedge. The wedge is held inclined at an angle of 4 ^{0} (fig.4.4a) and the edge of the wedge is kept parallel to the graphene layers. The width of the wedge (68.8 A^0) is kept larger than that of work material so that the entire width of HOPG is sliced. The depth of indentation is defined as the distance from the top layer to the bottom most wedge atom, which determines the thickness of exfoliated layers. From fig.4.4b, *DOI* can be written as (n-1)*t_o + t_x. (n - number of graphene layers above the wedge). The wedge position between the two nearest layers can be presented as t_x/t_o. The exfoliation process is performed in x- direction on the (001) surface of the work piece by moving the rigid wedge towards the graphite block with a constant speed. Simulations are conducted at constant temperature of 300 K. The set of parameters used for this simulations are provided in table 4.2. Initially, the wedge is placed a little distance away from the work material and after several time steps it moves forward to interact with the work material. The cleaving wedge interacts with the zigzag edge during the exfoliation simulation. Care should be taken while assigning cut-off values between the wedge and work materials. Various cut-off values have been tested and relevant chip morphologies and force profiles are obtained. All force components in x, y, z directions are plotted when the wedge edge moves from its reference position. The forces profiles generated by a cutoff value of 3.4 A^0 captured the proper forces, and hence is used this value for simulations.

In the experimental study, the wedge starts cleaving from one end of the HOPG block and emerges at the other end to complete the exfoliation. To simulate such experiments, two types of models are considered in the simulations. In one model, named hereafter as bottom fixed system (*BFS*), we fix the bottom two layers of atoms and there are no constraints on the two ends. The *BFS* model simulates the

Table 4.2: MD simulation model parameters

Parameter	Value
Work piece dimension (A ^{0})	208.5 x 59 x 68
No of atoms in the work-piece	53900
Wedge width (A ^{0})	3200
Wedge width A ^{0})	68.8
Wedge nose radius (A ^{0})	2.4
Clearance Angle (Degree)	4
Wedge angle (Degree)	35
Temperature (K)	300

fact that as the wedge reaches the end of the cut, the edge atoms are free to move in response to the advancing wedge. As graphene layers are weakly bonded by van der Waals forces, intuitively, we can expect that the small-applied forces at the cutting edge may cause shearing of layers in the direction of wedge motion [166]. In the other model, hereafter called as fixed end system (*FES*), as in most MD simulation studies of nano-machining, we fix not only the bottom two layers of atoms as in the *BFS* model but also one end of the HOPG (opposite end of where the wedge enters). The *FES* model simulates the fact that far way atoms with respect to the advancing wedge are in standstill position and relatively unaffected during initial wedge engagement and beginning of exfoliation.

We note here that the actual experimental conditions are not perfectly replicated in the simulation models. The limitations are mainly in wedge sharpness (in relation to layer thickness), model size, and computational times. We use higher wedge speeds and smaller work/wedge sizes in the simulation models to reduce computational times. Higher wedge moving speeds can result in larger temperatures due to higher deformation rates and frictional dissipation. In the simulations we use constant temperature throughout the machining process to eliminate any temperature effects. The wedge sharpness limitations can be resolved using a scaled model, resulting in reduced computational expenses. Thus, despite some limitations, we expect the

simulation results to provide fundamental understanding of the exfoliation process during the nano-machining. We use these two simulation models to study how exfoliation occurs during initial engagement, wedge penetration and as the wedge leaves the cut. The results and the findings are discussed in the following sections.

4.3 Separation, Folding and Shearing of Graphene Layers

During the nano-machining simulations, we found three kinds of separated layers similar to that observed in the experiments: clearly separated flat layers, layers that were folded, and layers that were sheared. The following sections describe the conditions under which different types of layers are likely to form.

4.3.1 Layer Separation

By layer separation we mean here cleaved graphene layers without any folding on edges. Simulation using the *FES* model showed that initial engagement of the wedge with HOPG results in initial layers deflects on (without folding) and wedge penetrates between the layers. In the experiments, the cleaved layers come on to the wedge surface and then slide onto a water bath. In the simulations, the cleaved graphene layers slide over the wedge surface as the wedge moves forward towards the HOPG as shown in fig.4.5. Water effects are not considered in the simulation. The wedge position is seen to be important to get cleaved flat layers without any folding (fig.4.5b). The number of layers that get cleaved is dependent on the depth of indentation. Positioning the wedge when n=1 and n=3 at $t_x/t_o = 0.59$ results in cleaving of one layer (fig.4.5a) and three layers (fig.4.5b) of graphene respectively.

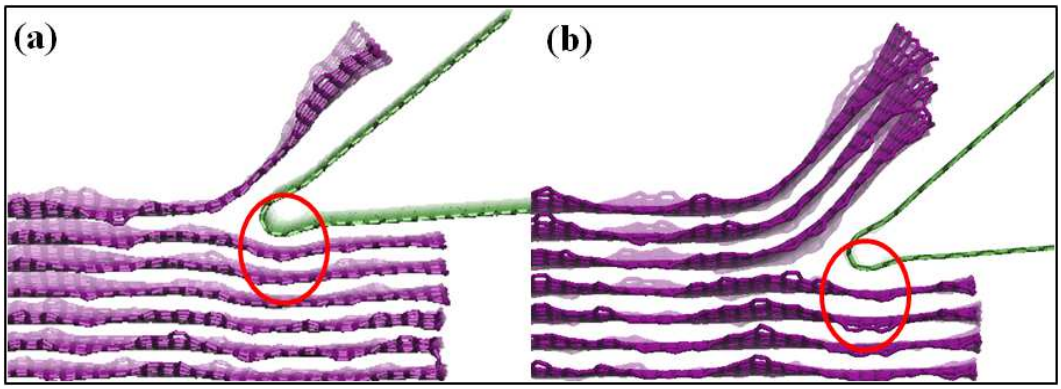

Figure 4.5: Conditions at which layer separation was seen in simulations (a) n=1, t_x/t_o=0.59; clear layer separation without folding, (b) n=3, t_x/t_0=0.59; clear separation without folding. The circles indicate the deflection of the layers below the wedge.

When the wedge is positioned at a smaller depth of indentation (n=1, t_x/t_o =0.18), the wedge elastically deflects the underneath layers instead of simply cleaving the top layer. There are considerable elastic deflections occurring due to the wedge pressing as shown in fig.4.5. These observations indicate that the wedge position is crucial and based on the wedge position one can predict the number and the nature of cleaved layers to be expected.

4.3.2 Layer Folding

Experimental results show the presence of folded layers of graphene in fig.4.1c. We observed similar occurrence of folded layers in the simulations also under certain conditions. The action of folding is directly influenced by the position of the wedge. It is observed that at certain wedge positions, penetration of the wedge causes the layer in front of the wedge to start folding (fig.4.6) instead of undergoing cleaving as discussed in the previous section (fig.4.5). The conditions at which it is observed is n=1 and up to t_x/t_o=0.18. Further advancement of the wedge makes the folded layer to spring back to the wedge surface recovering the fold. Two different depths of

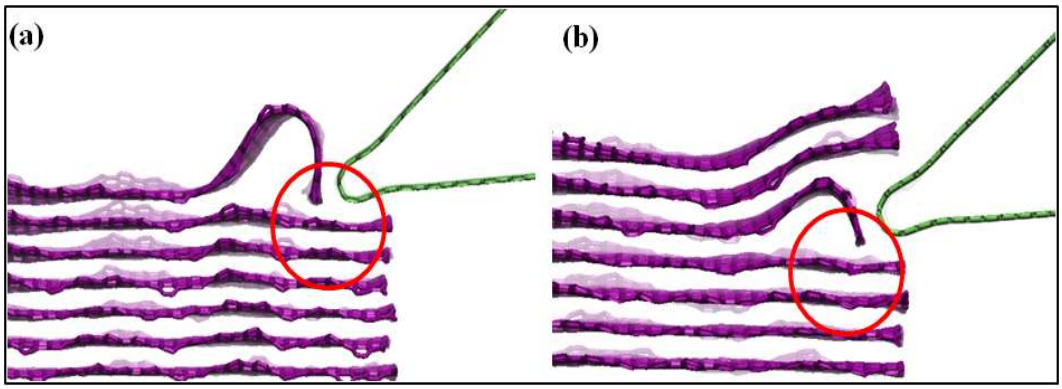

Figure 4.6: Folding of layers ahead of the wedge edge at various depths of indentations; (a) at n=1, (b) at n=3. Simulation is carried out at t_x/t_o =0.18, cleaving speed of 100 m/s. Less deflections are observed when the folding layers occurring. The circles indicate the deflection of the layers below the wedge.

indentation at a particular wedge position between the layers of t_x/t_o=0.18 displayed similar folding of graphene layers as shown in fig.4.6. The free rippled zigzag edges were seen to influence the folding of layers near the wedge tip.

As observed in the simulations, the wedge position plays a key role. We study the effect of wedge position and its influence on separation versus folding by studying the deflection of the layer immediately beneath the wedge. At lower values of t_x/t_o the layer deflections are low regardless of *DOI* (n value). At higher values of t_x/t_o the deflections are seen to increase dramatically. The conditions for folding and separation can be differentiated clearly: separation with folding occurs at low values of t_x/t_o where little deflection of the layer beneath the wedge is seen. Clear separation without folding occurs at higher values of t_x/t_o where considerable deflection of the layer immediately below the wedge is observed. We note here that the effect of the wedge-bluntness (or edge radius) may have a role to play in determining at what values of t_x/t_o the transition from folding to separation occurs.

Separation with and without folding are expected to affect some experimentally measurable signatures such as force or effort needed in wedge penetration. There are two types of forces acting on the wedge when it penetrates into the HOPG. The force

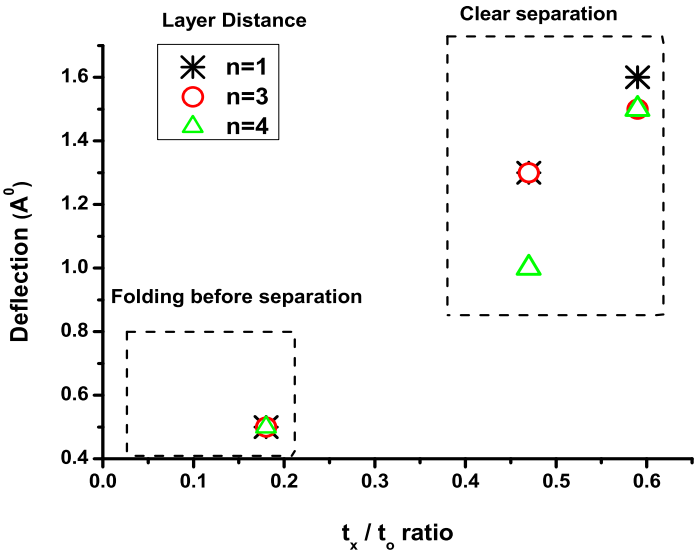

Figure 4.7: Deflection of the immediate layer below the wedge with respect to the wedge position (t_x/t_o) between the two nearest layers. Folding of the layer ahead of the wedge is observed at low values of t_x/t_o; clear separations of layers are noticed at higher values.

acting parallel (horizontal) to the wedge movement helps to cleave the layers and is called here as the cleaving force (fig.4.8a), the force perpendicular to the wedge movement is named as the vertical force (fig.4.8b). From the simulations, these forces acting on the wedge are extracted and plotted against the wedge displacement from its starting position. The cleaving force is seen to show a two peak profile. When the wedge starts to penetrate into the HOPG, a significant resistance force acts in horizontal direction on the wedge as evidenced by the first peak (fig.4.8a). The significance of second peak in simulation process corresponds to the folding of graphene layer. When exfoliating at t_x/t_o =0.18, the second peak is almost equivalent magnitude to that of first peak (see fig.4.8 inset) and causes folding of top layer (fig.4.6a). However, in other cases the magnitude of second peak is not that significant and there could be momentary partial folding and recovering to the flat structure. Similar trends were observed at values of *DOI* n=3. However, the magnitude of first peak reaches to 13.5 eV/A ^{0} for single layer cleaving (n=1) and

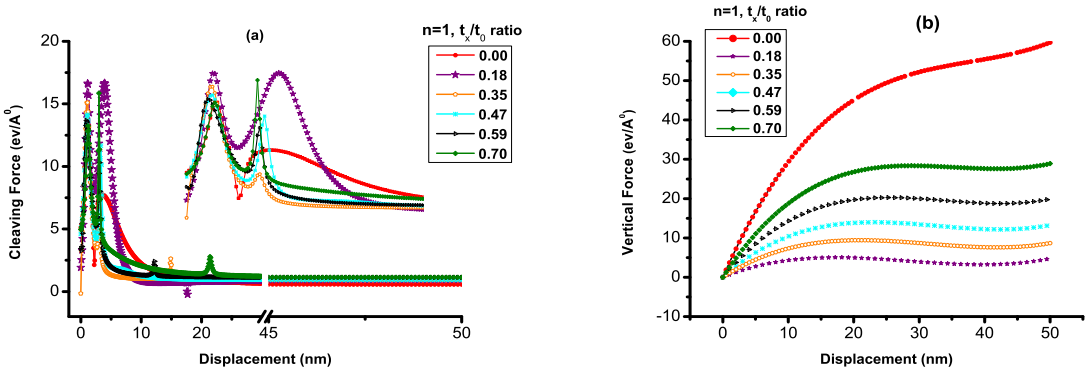

Figure 4.8: Forces acting on the wedge during the cleaving process for various wedge positions (t_x/t_o) ranging from 0 to 0.7 for n=1, (a) Cleaving force (b) Vertical force. The inset shows the two-peak profile signature seen during initial engagement of the wedge.

for three layers (n=3) this value reaches higher value 15 eV/A ^{0}. Such differences can be attributed to effort needed to fold the underneath layer. From the simulation analysis, it is clear that there is significant resistance offered by the HOPG during wedge engagement and while cleaving least forces offered to overcome the weak van der Waals energy between the layers. Beyond the second peak cleaving forces merge to a constant force and is represented by smooth cleaving process without any edge effects. The calculated constant cleaving force converges approximately to 1 eV/A ^{0} and matches well with calculated theoretical force value of 0.8 eV/A ^{0} required to break the van der Waals bonds in the cleaved region assuming a constant specific energy of 0.035 eV/atom [167].

The vertical force component during the cleaving process is calculated and reported in fig.4.8b. It is progressively increasing during the wedge engagement, reaching a constant value when the wedge moves forward to cleave the layers. The magnitude of vertical force varies with t_x/t_o unlike the cleaving forces which merged to single value as cleaving progresses. The magnitude of vertical force increases with increase in t_x/t_o. In the case of t_x/t_o =0, the magnitude of the vertical force is much higher

and is due to the wedge indenting the top layer instead of cleaving. The energy exerted by the wedge is spent on cleaving and pressing the wedge. By measuring the deflection of the layers immediately beneath the wedge, the bending energy can be calculated. The bending energy is given by equation 4.3 [168]:

$$E = (Bending\ Modulus) * (Bending\ Area) \tag{4.3}$$

and considering derivative as the force for bending (equation 4.4)can be determined as

$$F = \frac{\mathrm{d}E}{\mathrm{d}x} = \left(\frac{D * w}{R}\right)\left(\frac{1}{\sqrt{2R\,(x - x^2)}}\right) \tag{4.4}$$

where D is the bending modulus, w is the width of the HOPG block, R is the deflected curvature, and x is the vertical deflection. Adding up the forces required to deflect all the layers (in this case we calculate up to three layers) the magnitude of the vertical force is about 5.5 eV/A ^{0}. This value lies in the simulation mean force range of 5-55 eV/A ^{0} based on the wedge position. In this calculation we neglected the in plane strain and considered a constant bending modulus throughout the calculation. As stated in the literature multilayer graphene has different values for bending modulus based on the number of layers [169]. The above investigations clearly show that separation and folding can be controlled by adjusting wedge position. The analysis of forces indicates that the wedge based exfoliation process requires higher effort during initial wedge engagement and as exfoliation proceeds comparatively lower effort to sustain the cleaving process. The vertical force on the wedge depends on its position and the wedge is seen to impart strain to the layers beneath it; this could possibly influence the quality of the layers cleaved subsequently.

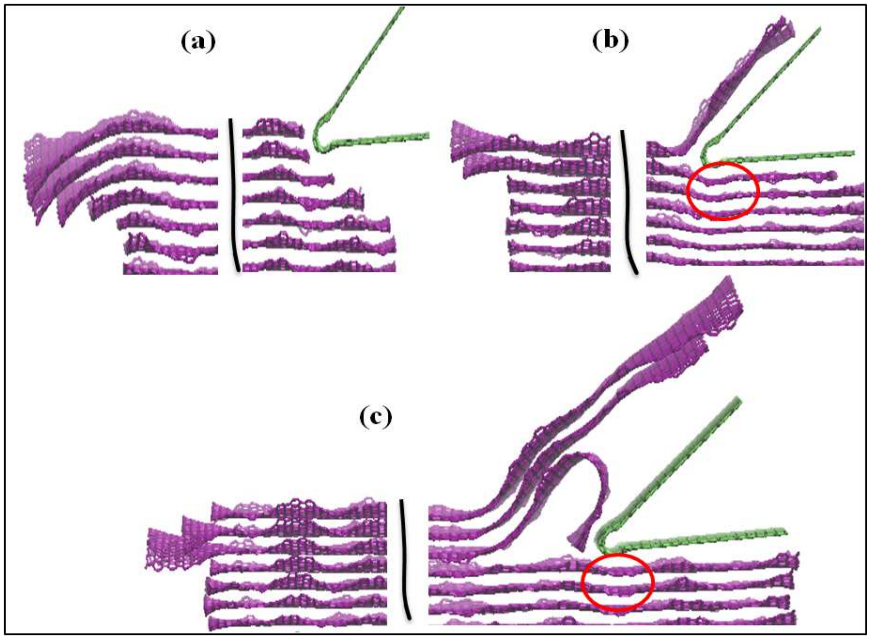

Figure 4.9: Shearing of graphene layers as the wedge exits the HOPG block using the *BFS* model where the end face atoms are free to move; (a) at lower speeds wedge advancement creates step like edges (n=1, $t_x/t_o = 0.59$ at 100 m/s), (b) At higher speeds wedge advancement shears the layers at end face while cleaving and separating a single sheet of graphene (n=1, $t_x/t_o = 0.59$ and cleaving speed of 500 m/s), (c) At higher depth of indentations at the same higher speed (as in (b)) a few layers graphene cleave and separate while a folded layer ahead the wedge is formed; this same folder layer is seen to get sheared at the end face (n=3, $t_x/t_o = 0.59$, and cleaving speed of 500 m/s). The circles indicate the deflection of the layers below the wedge.

4.3.3 Layer Shearing

During the experimental investigations shearing of graphene layers were observed in the cleaved samples (see fig.4.1d). However, we noticed little shearing in the *FES* model simulations that were discussed in the previous sections. We hypothesized that perhaps shearing was occurring only when the edge completes cleaving and exits the HOPG work sample. To check this hypothesis, simulations using the *BFS* model are considered here. In this model, the rear side atoms are free to respond and move to applied forces; this is the only difference in the model setup compared to the *FES* model used earlier. Different depth of indentations and various cleaving

speeds are simulated at room temperature using this model. The simulation results are shown for three different scenarios in fig.4.9. Figure 4.9a shows that shearing of layers occurs at two places: at the front of the HOPG block (below the wedge) and also at the back end of HOPG when cleaving at a lower speed of 100 m/s. Due to weak van der Waals interactions between the layers, these shear layers look like step edges. Once, the step edges (fig.4.9a) formed the layers below the wedge are locked due to energetically active edges and layers above the wedge slide horizontally in the direction of wedge penetration. No layer separation was observed. Similar cleaving patterns are observed at other wedge positions (t_x/t_o) and various *DOI* (n) at this same speed; more layers were seen to shear out of the back end at higher *DOI* values. When cleaving at a higher speed (500 m/s) two scenarios are noticeable depending on the depth of indentation. At lower depth of indentation, (fig.4.9b), the graphene layer cleaves, separates and slides on to the wedge surface similar to that observed in the *FES* model simulations. However, at the rear end of HOPG we can observe that the top two layers undergo shearing out of the HOPG end face. The separated layer was seen to be sheared the most at the HOPG end face with the shear gradually reducing in the layers beneath it. At higher depths of indentation layer separation was seen but along with a folded layer close to the wedge tip position. This folded layer was seen to be sheared the most projecting out of the HOPG end face; the cleaved and separated layers above it and the layers below it were seen to undergo less shearing at the HOPG end face. At slower speeds the layers prefer to shear rather than cleave and separate (fig.4.9a). A higher speed of cleaving layer separation is preferred along with shearing. The shearing seems largely restricted to the layers closest to the wedge tip. With the exception of the case when the wedge tip is close to the HOPG surface where the layer closest to the tip gets separated and sheared (fig.4.9b), the separated layers are seen to undergo less shear (fig.4.9c). These simulation results show that the wedge exit effects are

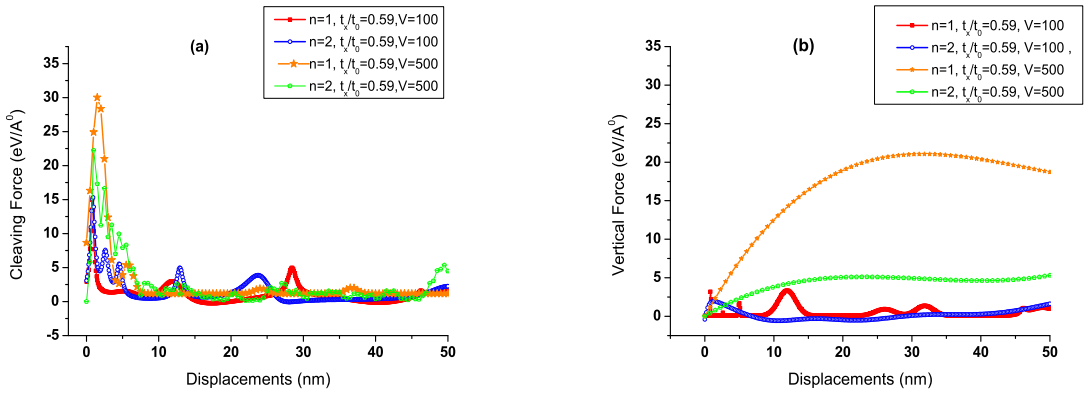

Figure 4.10: Forces acting on the wedge extracted from the BFS model simulations; (a) Cleaving force and (b) Vertical forces at n=1, 3 and at t_x/t_o=0.59 for low (100 m/s) and high (500 m/s) cleaving speeds.

important for layer shearing that was observed in the experiments. Layer shearing is likely to influence the forces experienced by the wedge as it reaches the end of the cleaving process. This is considered next in the discussion.

Similar to the *FES* model, the forces on the wedge are extracted from the simulations and plotted as shown in fig.4.10. The cleaving and vertical forces are calculated for two sets of cleaving speeds and depths of indentation. fig.4.10a presents the variation of cleaving forces with wedge advancement. At the time of wedge engagement (left side of the graph), a large resistive force in the form of an initial peak is observed at both speeds and *DOI*. Once the wedge engages completely then the forces acting on the wedge diminish as cleaving starts and also due to the weak van der Waals forces between layers of graphene. At higher cleaving speeds, the magnitude of initial peak is twice that seen at lower cleaving speeds. Also *DOI* has no effect on the magnitude of the peak forces at lower speeds but has an effect at higher speeds; lower *DOI* (n=1) appear to produce a higher peak than the larger *DOI* (n=3). At the lower cleaving speeds, for n=1 and n=3, the low intensive intermediate peaks is seen and is caused by sliding resistance between the step edges and the resistance from the folding of layer. However, at higher cleaving speeds, the intermediate peaks

are seen to diminish since the number of sheared layers is less than that at lower speeds.

Trends in the vertical force component are shown in fig.4.10b. Small intermediate peaks are observed, at lower speeds, due to edge interlocking effects. Large vertical forces are seen at lower *DOI* (n=1) at higher cleaving speed; this may be due to the wedge indenting the layer below the tool (similar to that seen in the *FES* model) and at higher *DOI* the initial peak is predominantly caused by the folding of graphene at the time of wedge engagement; the wedge indentation effect is smaller here. Large vertical forces can be detrimental to the graphene layers causing stress and damage. The large vertical forces can be avoided by appropriate choice of speeds and *DOI*.

4.4 Correlation of Structural Defects and Intermittent Force Spikes

Using the developed molecular model no other intermittent peaks were observed as reported in the experimental force measurements. The molecular model is now altered by incorporating one type of defect (a discontinuous layer) observed in earlier experiments (chapter 3.4). The results are shown in fig.4.11. The sectioning force profile, without any defects, indicates a single sharp spike at the beginning of the wedge engagement (fig.4.11a-c). The altered model is shown in (fig.4.11d). Penetration of the wedge initiates cleaving of the first layer as shown in the fig.4.11e. Further wedge movement causes wedge interaction with the modeled discontinuous layer. The simulated sectioning forces are shown in fig.4.11f. There are several spikes seen in the sectioning force. The first spike is due to the wedge engagement with the material. Next spike is due to the wedge engagement with the discontinuous layer. Subsequently, another spike is appearing very close to the previous spike due

to layer bending ahead of the wedge. The simulation spike trends are similar to the experimental observations we reported earlier. Hence, defects such as pre-existing discontinuous layers in the HOPG and their interactions with the wedge can lead to the appearance of several spikes in the sectioning force characteristics. For a further complete understanding of the force signatures one needs to consider simulating other defects such as kinks reported earlier in the FESEM and TEM micrographs.

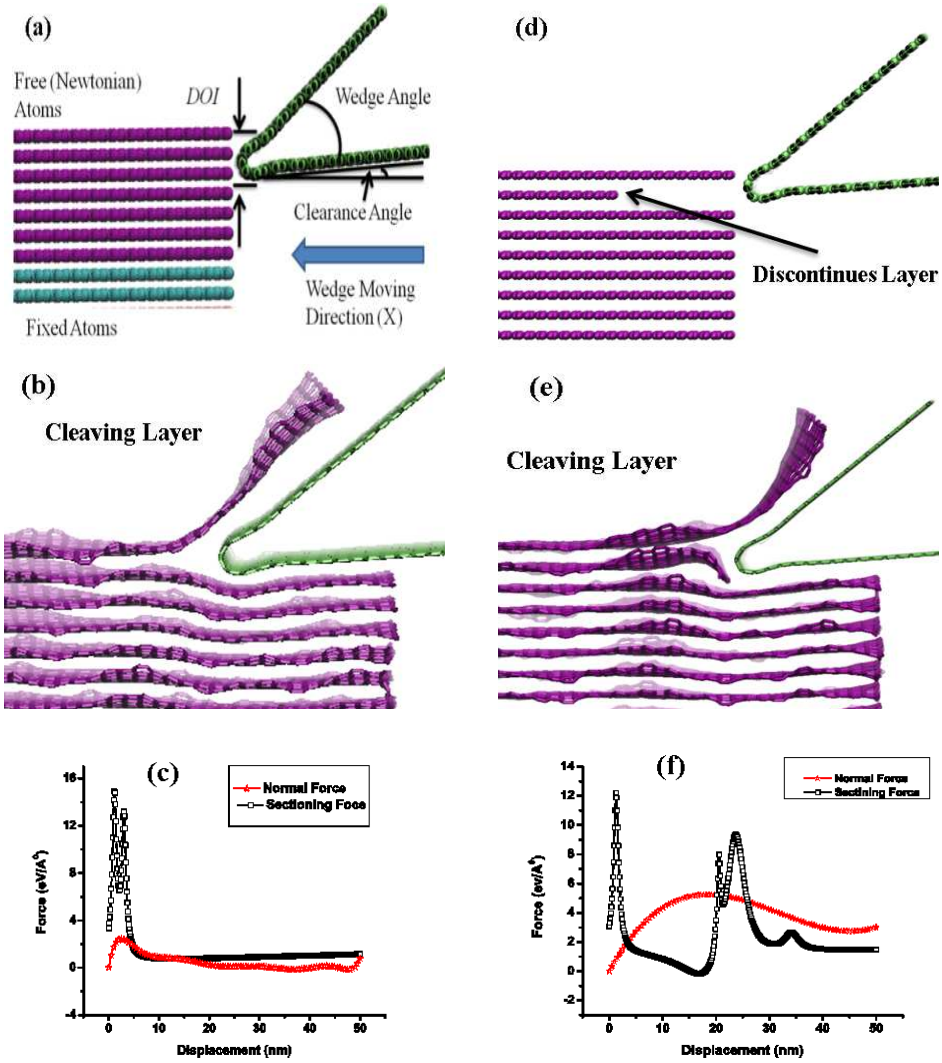

Figure 4.11: Molecular dynamics simulation model and results: (a) The modeled MD system with defect-free layers, (b) Separation of layers, (c) Sectioning force profiles - only one peak is observed, (d) The MD model with a discontinuous layer representing a pre-existing defect in the HOPG, (e) Shape of the layers generated ahead of the wedge during sectioning, (f) Sectioning force profile now displays multiple peaks.

4.5 Effect of the Larger Wedge Radius

At the macro scale, the wedge may appear to be perfectly sharp but at the nanoscale it can be significantly blunt when considered relative to the depth of insertion [79]. A sharp wedge has a positive rake angle whereas a blunt wedge has a negative one [79], when the depth of insertion is smaller than the wedge radius. Thus, the edge radius has considerable effects on the machining process particularly on machining forces, stresses, deformation zones, and quality of the surface produced [170]. A larger wedge radius exerts a hydrostatic pressure on the material when machined with negative rake angles. This edge-radius effect results in a ductile mode machining in brittle materials [79]. Literature also reports [171] that the material removal mechanism becomes one of plowing instead of machining due to the bluntness of the cutting edge.

From the observations in earlier chapters, initial wedge-material engagement is seen to be important. It is difficult to observe the process online at this scale, we attempt to understand the effects of edge radius on the WBME technique using molecular dynamic simulations. We focus on minimum thickness of layer that can be removed at various wedge radii. This study further considers the effects of wedge-material engagement on the nature of the cleaving and the forces acting during this impact. These simulation results may help to fine-tune the cleaving process for better accuracy and consistency. We use a simulation model similar to that with used earlier (section 4.2) but various wedges radii of 2.45, 5.46, 11.6, and 22.5A^0. The wedges consist of 3240, 2646, 3840 and 7452 atoms respectively. There are 43218 free and 10682 fixed atoms in the model. All other parameters are similar to what we used in section 4.2. We start our discussion by presenting the wedge radius effects on the minimum thickness of sheet cleaved on cleaving and folding, and on the nature of the folds produced.

1. ***Effect of the wedge radii on Critical Depth of Insertion ($DOI_{critical}$)***

It is reported in the literature that the material removal occurs very differently when the wedge radius is comparable to the depth of cut [172]. Thus, it influences the minimum thickness that can be removed from the material. Minimum cut thickness is about $1/10^{th}$ of the cutting edge radius for continuous (non-layered) materials [173]. Ikawa N et al. [174] studied the minimum thickness of cut in diamond turning and presented a definition based on experimental and simulation studies. In crysterlline metals (continuous material), the minimum cut thickness is defined, as the minimum uncut chip thickness which can be stably removed from the material [121, 174]. The factors such as wedge sharpness, material uniformity and the affinity of wedge and material have a influence on the minimum thickness of cut in conventional materials [174].

Limited investigations have been reported on the minimum thickness of cut in a layered material. Here we investigate the minimum thickness of sheet under various wedge radii. Interestingly, in this material due to the layered structure, the minimum thickness amount of material that can be removed is a single sheet of graphene layer. According to our earlier findings using a very sharp wedge, the initial wedge material engagement is more vital for the nature of cleaved layers. We noticed that at some conditions the wedge slides on the surface without cleaving any layers. This is because, if the *(DOI)* is below the critical value, any wedges no matter what its radius is slides on the surface (fig.4.12a, c, e, and f). However, gradual increase of *DOI* results in layer generation via rubbing of the wedge on the surface. Such layer cleaving is shown in fig.4.12b, d, f, and h. A sharper wedge cleaves the layer at a depth of insertion of 0.2A ^{0} and DOI)$_{critical}$ is independent of wedge radii at higher magnitudes as shown in fig.4.13. A depth of insertion of 1.6 A^0 is the critical value for a blunt wedge. We also measure the size of the buckling of the cleaved layers

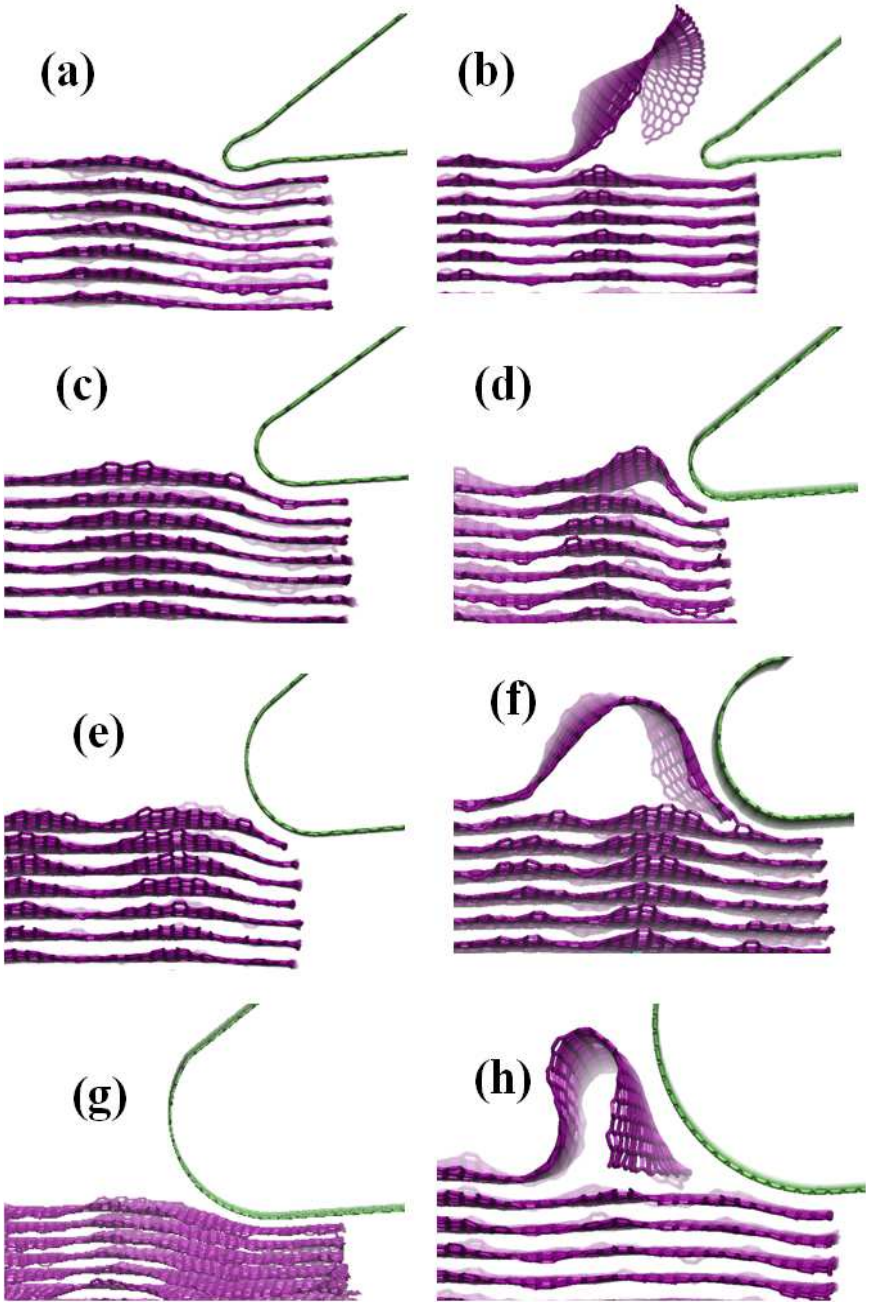

Figure 4.12: Investigation of $DOI_{critical}$ with respect to wedge radius. The wedge radius in; (a) and (b) is 2.45A ^{0}, (c) and (d) is 5.46 A^0 , (e) and (f) is 11.6A ^{0} , (g) and (h) is 22.5A ^{0}.

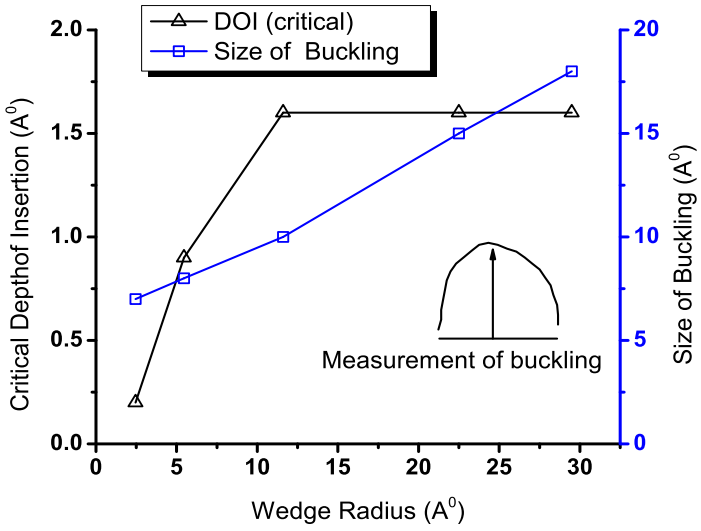

Figure 4.13: Variation of $DOI_{critical}$ and the size of buckling of the cleaved layer against the wedge radius is shown in (i).

ahead of the wedge and the amount of buckling increases with wedge radii (fig.4.13). The larger the wedge radii, the more bending the cleaved has to undergo before it overcome the the bluntness and get released above the wedge. in the next section, we focus on the effect of the larger wedge radius on cleaving layer geometries.

2. *Effect of the Wedge Radius on Wedge-material engagement*

Use of a sharper wedge resulted in several shapes of cleaved layers in section 4.2-4.4 and it will be interesting to see how the fold geometries change with a blunt wedge. For this study we select a larger wedge a radius of 11.6 A^0. The wedge position is controlled within the first three layers and the observation of initial wedge-material impact is shown in fig.4.14. At DOI =1.2 A^0, the wedge merely slides on the material surface without cleaving any layers (fig.4.14a). Gradual increase of DOI to 1.6 A^0 results in cleaving of a layer with a fold ahead of the wedge (fig.4.14b). After initiation, and buckling the layer then gets released on to the rake face of the wedge over and above the blunt nose of the wedge. Increase of DOI from 2 to 4.6 A^0

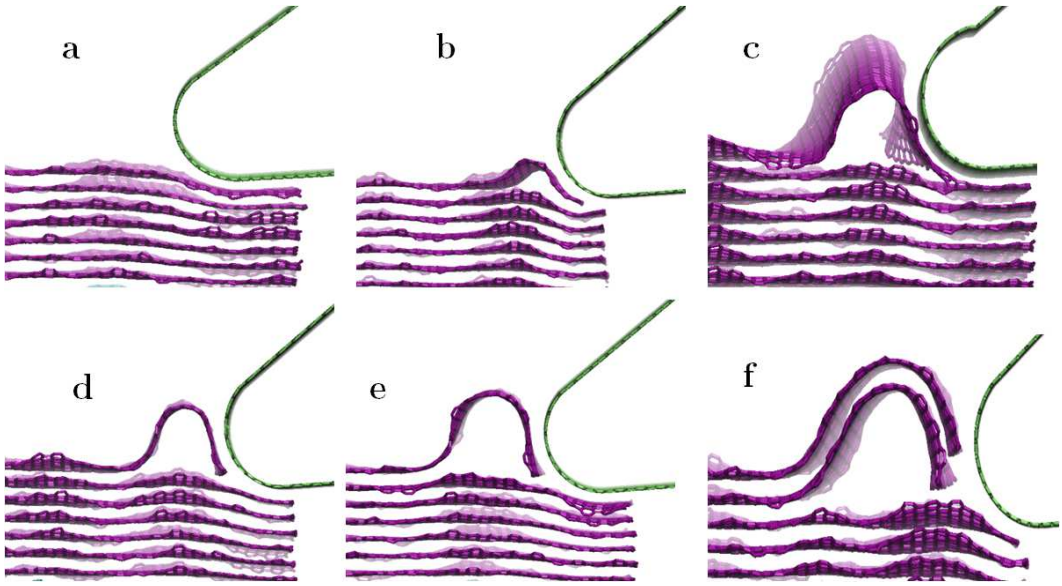

Figure 4.14: Effect of wedge radius (11.6 A^0) on layer initiations at various *DOI*; (a) *DOI*=0.6 A^0, (b) *DOI*=1.6 A^0, (c) *DOI*=2.0 A^0, (d) *DOI*=3.4 A^0, (e) *DOI*=4.6 A^0 and (f) *DOI*=6.8 A^0

(fig.4.14c-e) shows a similar trend of sliding and layer formation. Further, increase of depth of insertions to 6.8 A^0 results in cleaving two layers together (fig.4.14f). From our observations, rubbing becomes the major mechanism of cleaving mechanism under the action of a blunt wedge. Although, the wedge starts with a fold it is interesting to see how it behaves during the continued wedge penetration inside the material. During further wedge penetration (fig.4.15a), the separated layer folds back on to surface at *DOI* 1.6 A^0. Evidence of such folding was seen experimentally (fig.3.18b). However, at *DOI*= 3.4 A^0, the initiated layer exhibits entirely different behavior compared to earlier case (fig.4.15b). The folded layer moves on to the wedge face. The advancement of the blunt wedge at a depth of insertion of 6.8 A^0 results in twisting of the cleaved layer (fig.4.15c).

Forces acting on the wedge during penetration provide vital information about the cleaving process under the blunt wedge. Such insights are helpful to understand and control the process. Figure 4.16a shows how forces profiles detected from the simulations. The cleaving force, horizontal component, consists of several peaks. It

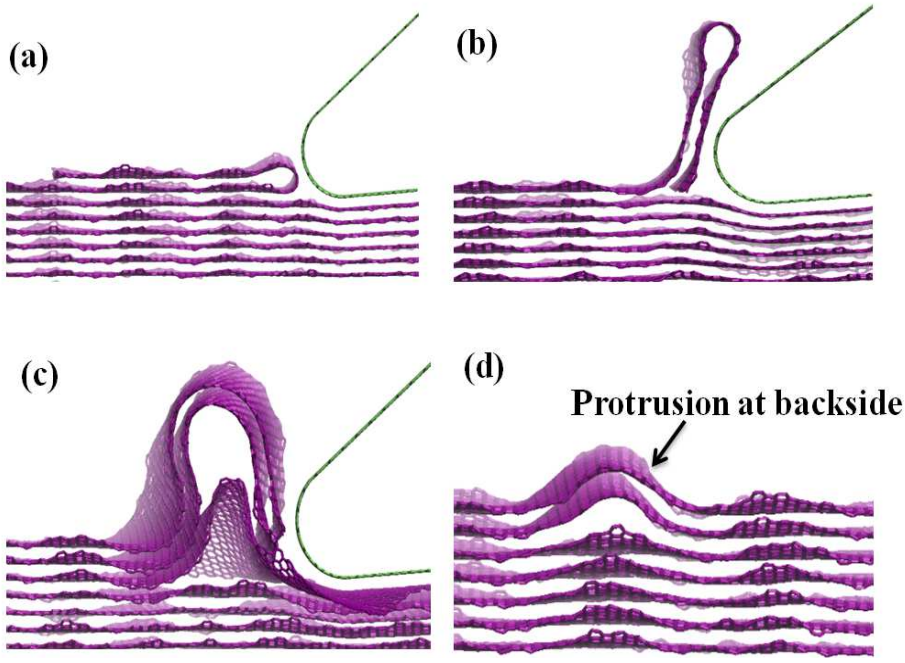

Figure 4.15: Cleaved layer behavior after significant penetration inside the material; (a) *DOI* at 1.6 A^0 abruptly kick off layers fold back on to the surface, (b) at 3.4 A^0 the initiated folded layer continues with the wedge penetration, at *DOI* 6.8 A^0 (c) shows subsurface damages and twisted layers during the wedge penetration, (d) Protrusion at the backside of the material

starts with a smaller (magnitude) spike (P1 in fig.4.16a) followed by a broader peak (P2). Observations of atomic trajectories indicate that the smaller peak arises due to the wedge compression of the layers. The border peak signifies the completion of cleaving. The magnitude of the first spike gradually rises with increase in *DOI* and the position of the broader peak moves closer to the initial peak.

Figure 4.16b shows how the normal force, acting in the perpendicular direction. It is seen to gradually increase and dominate with continued wedge penetration. We noticed two different shapes of normal force profiles: one having a peak in the middle and the other showing an exponentially increasing trend. The middle-peak occurs when the layer abruptly release from its buckled shape and moves on to the wedge face. This is observed at *DOI*=1.6 A^0. At this moment, the pressed layers underneath the wedge have more freedom for elastic recovery. In the other scenario,

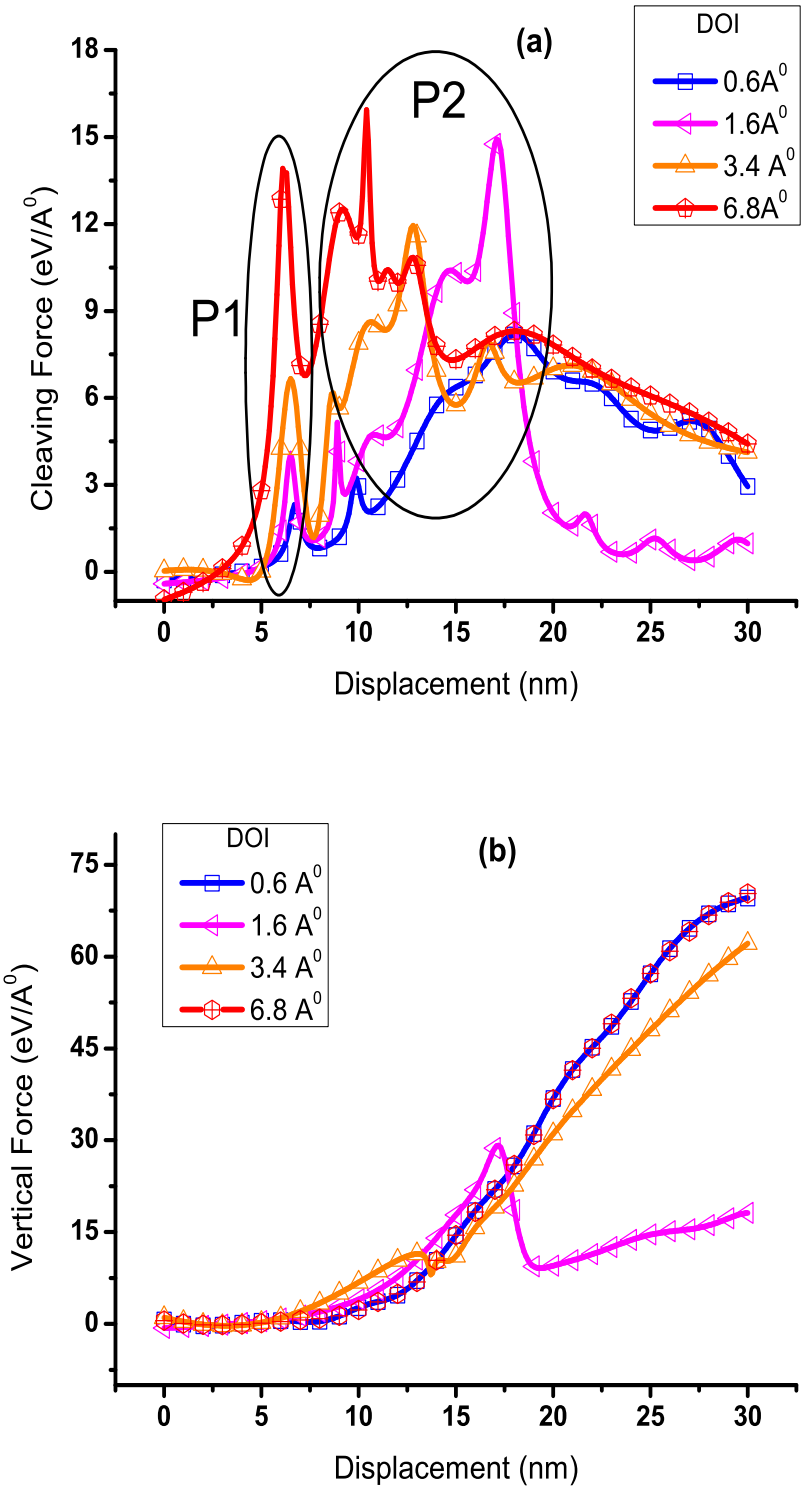

Figure 4.16: The cleaving and vertical forces acting on the wedge (11.6 A^0) with respect to the wedge position; (a) Cleaving and (b) Vertical force profiles

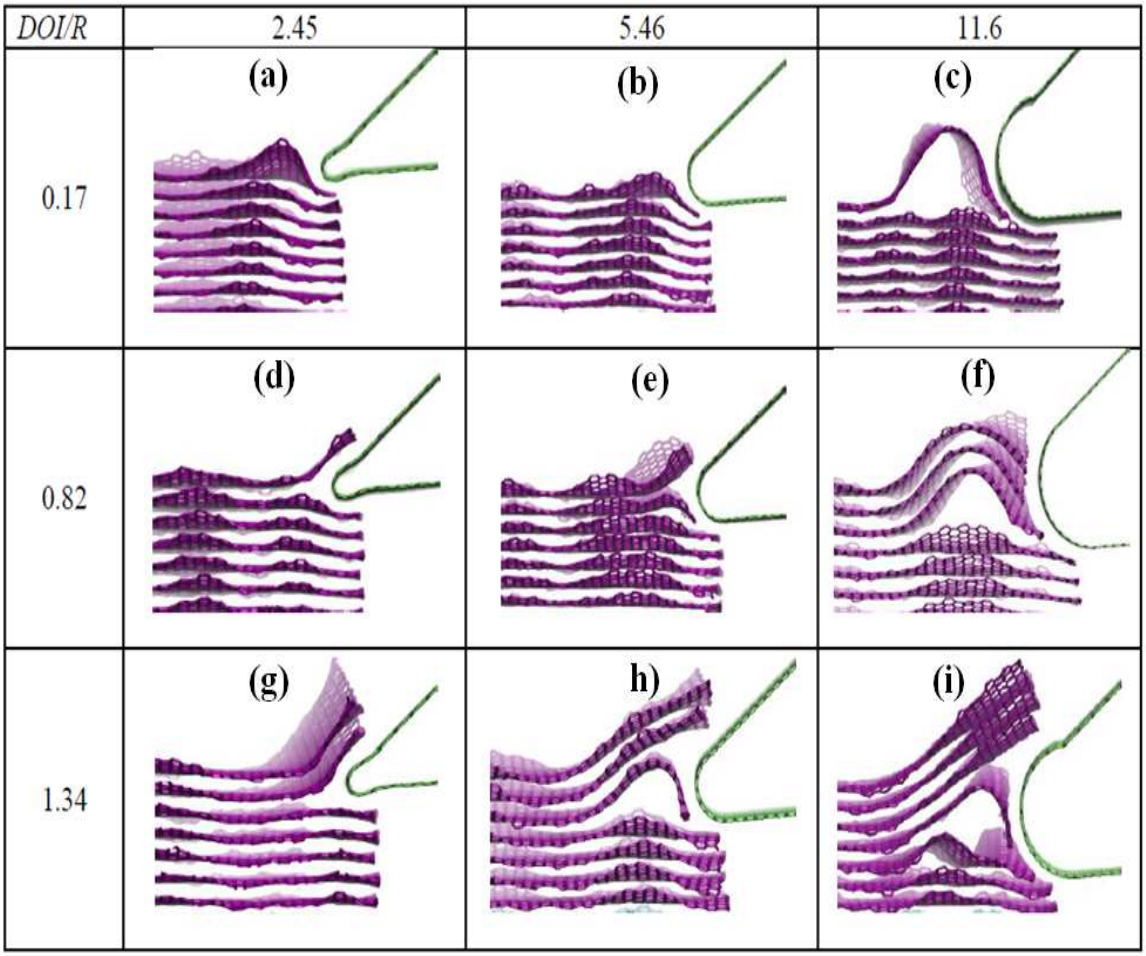

Figure 4.17: Wedge-material engagement at *DOI/R* 0.17, 0.82, and 1.34 with wedge radii 2.45, 5.46, and 11.6 A^0

the bending layer ahead of the wedge acts as a barrier to this recovery.

3. ***Effects of wedge radius on cleaving and folding at large DOI***

The study in the previous section was restricted to shallow depth of insertions. Now, we extend this study to analyze the effect of the wedge radius at larger depth of insertions. For this study, we selected three ratios of *DOI* to R (0.17, 0.82, and 1.34). The depth of insertions are selected in the broader range of 0.2 to 30.8 A^0 to satisfy the *DOI/R* ratios for a particular wedge radius. Figure 4.17 summarizes the wedge-material engagement with respect to *DOI/R* ratios. The observations clearly indicate three types of layer initiation modes during the initial wedge-material

interaction. These can be broadly classified into with and without layer folding a ahead of the wedge and a mode creates a protrusion at the back of the material. At lower *DOI/R* ratio (0.17), beyond the critical *DOI*, the wedge penetration starts a buckling layer ahead of the wedge. Figure 4.17a-c indicate this mode of layer initiation. All layers buckle upwards and rubbing is the main mechanism that cleaves the layer. In the second mode, layers get generated without any buckling ahead of the wedge. This phenomenon is observed with the sharper wedge as indicated in fig.4.17d and g. After the initial wedge engagement, further wedge penetration deflects the layers to either side of wedge leading to clear separation. The wedge radius has a significant contribution to this type of cleaving process. The nature of such cleaving process is similar at higher depth of insertion with respect to a particular wedge position. In the third mode, after the initial wedge engagement, the process neither cleaves any layer nor initiates any buckling ahead the wedge. Although, the initial impacts looks like a layer is about to generate (fig.4.17e), the continuous wedge penetration initiate a protrusion at the backside of the material (fig.4.15d). It shears several layers from the material surface. This feature is similar to the kinked structure that was observed in experiments. Increase in both *DOI/R* ratio and wedge radius (fig.4.17i) resulted in the separating layers latching on to another subsurface layer beneath the wedge. The layer thicknesses are seen to be uniform except for subsurface latching. From these observations, it is clear that the wedge radius has a significant effect on the nature of the cleaved layers produced by WBME process.

4. ***Effect of wedge radius on forces at large DOI***

We discuss here the force signatures, both cleaving and vertical, acting on the wedge during its penetration and how it changes with changes in *DOI/R* ratio. The force profiles under *DOI/R*=0.82 is shown in fig.4.18a-c. The initial wedge-material en-

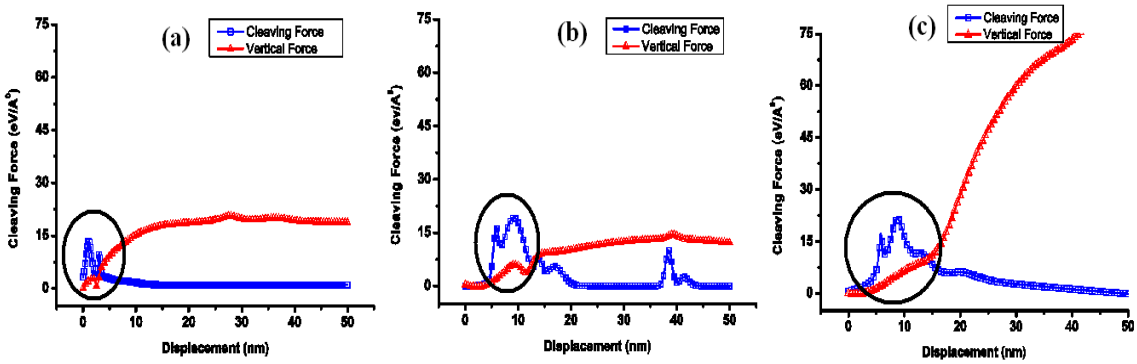

Figure 4.18: Forces profiles at DOI/R=0.82; (a) Wedge radius=2.45 A^0 , (b) Wedge radius=5.46 A^0 , (c) Wedge radius=11.6 A^0

gagement taken place at the circled region. The width of the circled area increases with increase in wedge radius. The amount of cleaving force after the initial impact reduces with the wedge penetration. A significant increase in the vertical force is noticed with increase in wedge radius (fig.4.18c).

We study the maximum force acting on the wedge during its engagement. This force also may cause maximum distortion in the layers at the point of separation. We obtained the peak cleaving force and respective vertical components from the captured forces. Figure 4.19a-c shows the variation of cleaving and vertical forces as well as the ratio of vertical to cleaving force with respect to wedge radius. The effect of wedge radius on the cleaving force is more pronounced on the radius increases. A closer look at the sharper wedge shows higher magnitude of the force value at lower DOI/R, than at other ratios. At higher ratios layer initiation modes are different (sliding vs deflection) and this may cause the difference in the cleaving force magnitude. This may correlates to the presence of thickness variation (expected vs cleaved) at higher cleaving forces.

Figure 4.19d-f shows the variation in, cleaving forces, vertical force, and also vertical-to-cleaving force ratio, with DOI/R. Cleaving force variation with DOI/R shows similar trend as in cleaving force variation with wedge radius, except that the vari-

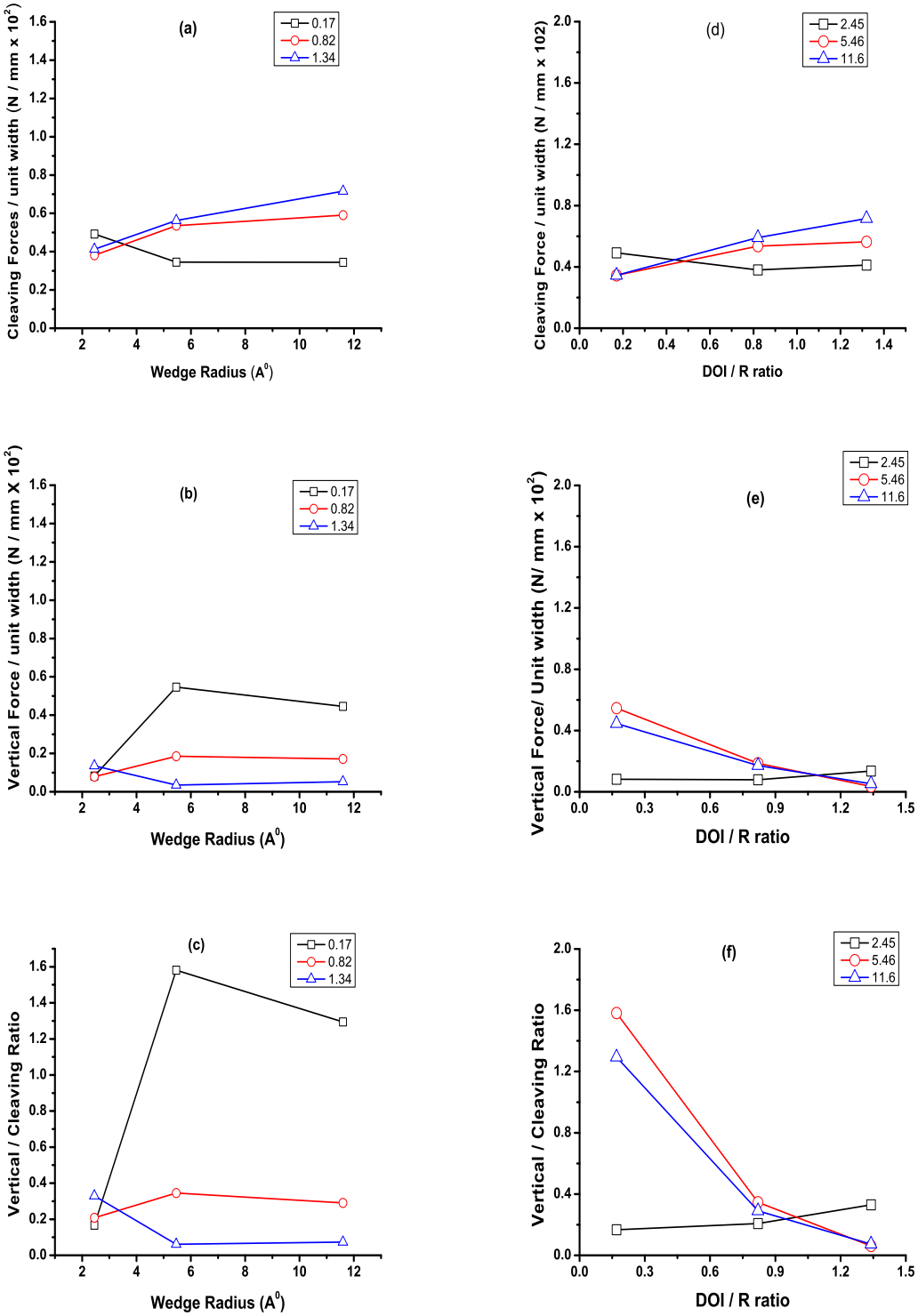

Figure 4.19: Force variation with wedge radius; (a) Cleaving force, (b) Vertical force, (c) Vertical to cleaving ratio, Force variation with DOI/R , (d) Cleaving force, (e) Vertical force, (f) Vertical to cleaving ratio

ations are smaller. Effect of the wedge radius is less at lower *DOI/R* and more pronounced at higher *DOI/R*. Vertical force variation shows the opposite trend with higher variation at lower *DOI/R* ratios. The *DOI/R* is seen to affect vertical to cleaving force ratio strongly with very large variation at small *DOI/R*, little to no variation at mid-range *DOI/R*and slightly large variation at higher *DOI/R* ratios. Though in the simulations the depth of insertions are very small compared to the experiments, we extrapolate the forces to match with the experimental conditions. The simulations with a blunt wedge ($11.6A^0$) provides the values for cleaving and vertical forces as 2.9 and 0.32 N/(mmx10^2) respectively.

The specific cutting energy is related to the forces and also provides vital signatures about the process. We compare the effect of wedge radius on the cleaving process at two wedge radius of 2.45 and $11.6A^0$ as shown in fig.4.20a. At lower depth of insertions a higher variation in the specific cutting energy is observed at both wedge radii but at higher DOI the variation reduces significantly. This specific cutting energy variation is similar to that seen in the literature with continuous materials [175]. The plowing effect is reported as the major contributor for such effect, with the supplied energy not completely consumed only for material removal [175]. At the beginning, a smaller wedge radius tool consumes more energy than the one with larger radius. This may be caused by different layer initiation modes. A sharper wedge deflects the layers while the blunt one slides on it. The influence of the wedge speed is also shown in fig.4.20a for the larger wedge radius tool. Larger variation is observed at lower depth of insertions and variation disappears with increase in *DOI*.

$$\sin(\theta) = \frac{r_e - t_o}{r_e} \tag{4.5}$$

The effective rake (fig.4.20b) has a significant contribution in nanoscale cleaving due to wedge bluntness. When the depth of insertion is less than the wedge radius, the

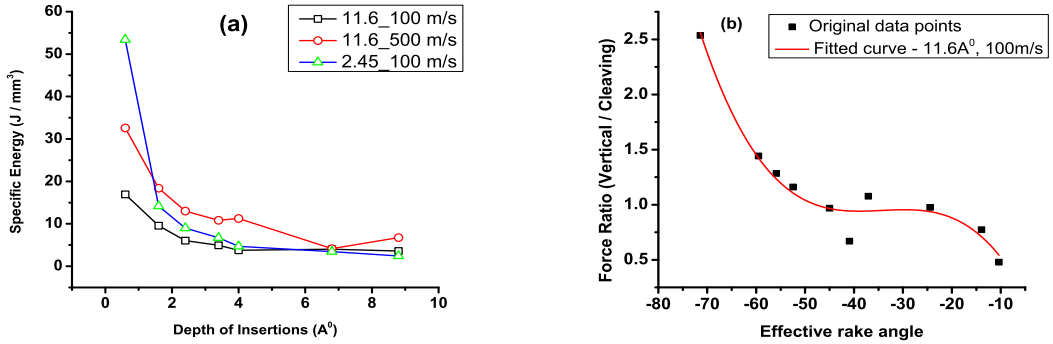

Figure 4.20: Cutting energy variation; (a) Specific cutting energy variation at wedge material interface, (b) The force (vertical / cleaving) variations with the effective rake angle for wedge radius (11.6A^0)

effective rake angle always becomes negative [176]. As reported [177], the effective rake angle can be calculated from the equation 4.5. The parameters in the equation: t_o as depth of cut, r_e as wedge radius, and θ as effective rake angle. The effective rake calculation based on our MD simulation (wedge radius 11.6 A^0, *DOI* ranging from 0.6 to 9.5A^0) varies in the range of -70 to -10 degrees. Observations of the atomistic trajectories indicate that the layer is formed when the wedge effective rake angle decreases to about -60 ^{0}. Such analysis can be used when experimental parameters are determining.

4.6 Effect of Ultrasonic Vibration

Many attempts have been made to assist the cutting techniques using application of vibration [80, 114]. Vibration can either be applied to the tool or the material in micro cutting. Such vibrations can be applied in the transverse direction, i.e. the direction perpendicular to the tool moving direction, and has many reported advantages such as reduction of chip thickness variations, applied forces, and improvement of surface finish [81]. It has been reported that oscillation applied in the

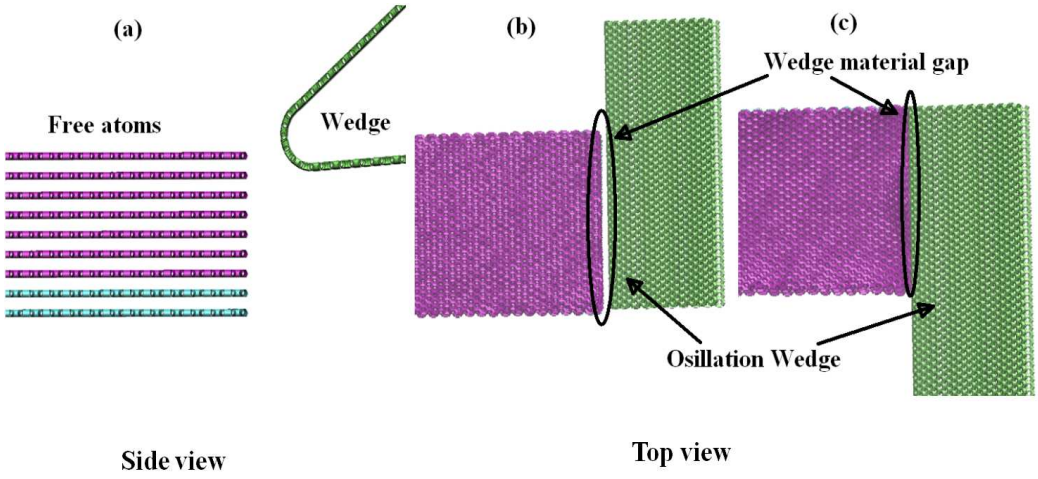

Figure 4.21: Oscillating wedge material system; (a) wedge material system, (b), (c) two consecutive wedge positions that indicate the oscillatory motion)

transverse direction reduces thickness variations (compression) and improves quality of the surface [24, 178]. As reported in chapter 3, our set up is capable of providing oscillation to the wedge. Recently, a number of attempts reported to develop this type of cutting technique as a fabrication method. The associated literature use the term *chatter* to indicate the cutting action. However, chatter is often avoided specially in microtome sectioning. Nevertheless, several reports [178, 179] proposed a effective way to use the chatter with an oscillating diamond knife to produce nanostructures. The focus is on controlling the wavy patterns. Here we attempt to use of simulation technique to model the vibration applied to the WBME process of cleaving graphene layers.

In this model, the wedge is oscillated perpendicular to its moving direction. Here, we assume no oscillations in any other direction. The applied frequency is a limiting factor in the simulation model. Similar to the use of a much higher speed in the simulations. Here we simulated much high frequencies. However, the insights obtained may provide a wealth of information useful for understanding and fine-tuning the process. The motions of the wedge movement simulated in LAMMPS software package. The relevant line of code is given in Appendix. The amplitude and the

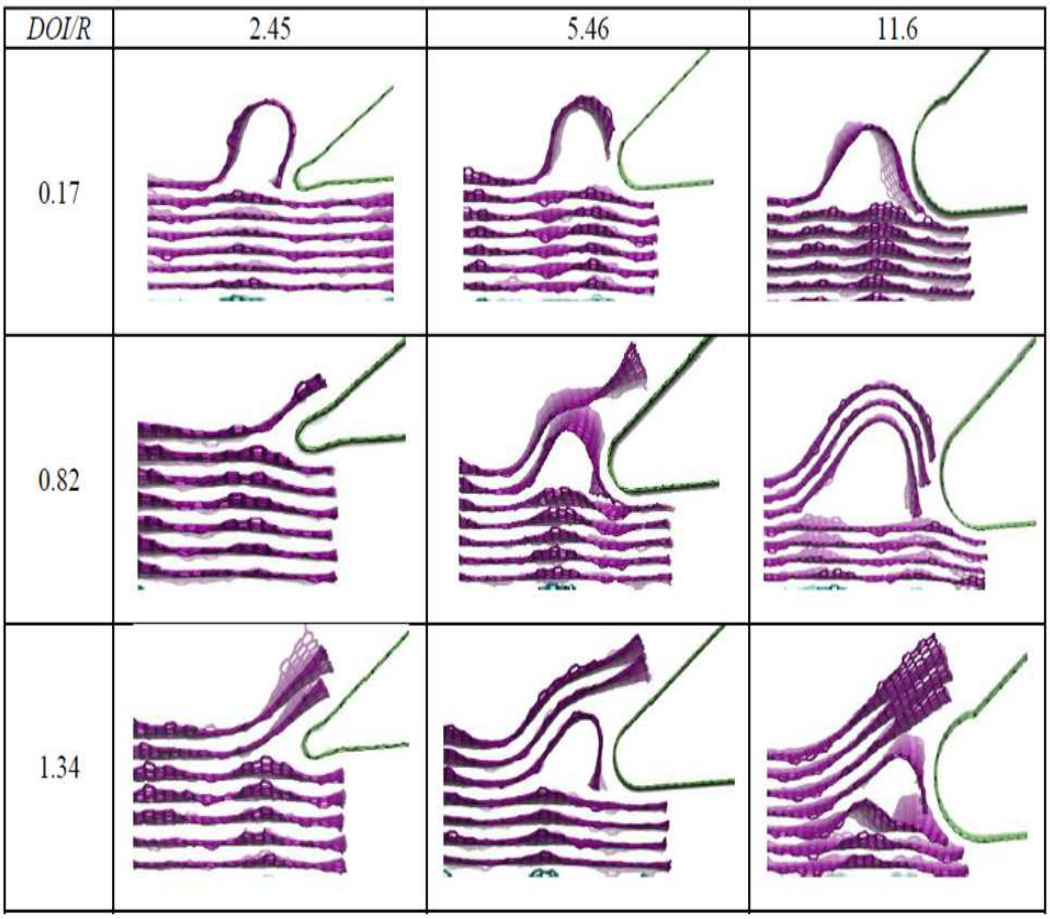

Figure 4.22: Wedge-material engagement with variation of *DOI/R* with ultrasonic vibration.

time period, have to be coded to get the desired frequency. The MD simulation system runs at the pico-second (ps) time scale. Therefore, the period value must be suitable for the system. For an example, we used a time period of 4 ps at which the model provide an oscillation of 250 GHz. During the experiments, we employed oscillations in the range of 25-40 KHz. Figure 4.21 shows the model setup. Two consecutive wedge positions are indicated and the reduction of gap shows the wedge movement in the cleaving direction (fig.4.21 b, c). Two relative wedge positions also shown the oscillating action taking place perpendicular to its moving direction. The observations of wedge material interaction are discussed in the next sections.

Fig.4.22 shows the wedge-material engagement with applied oscillations. The impact

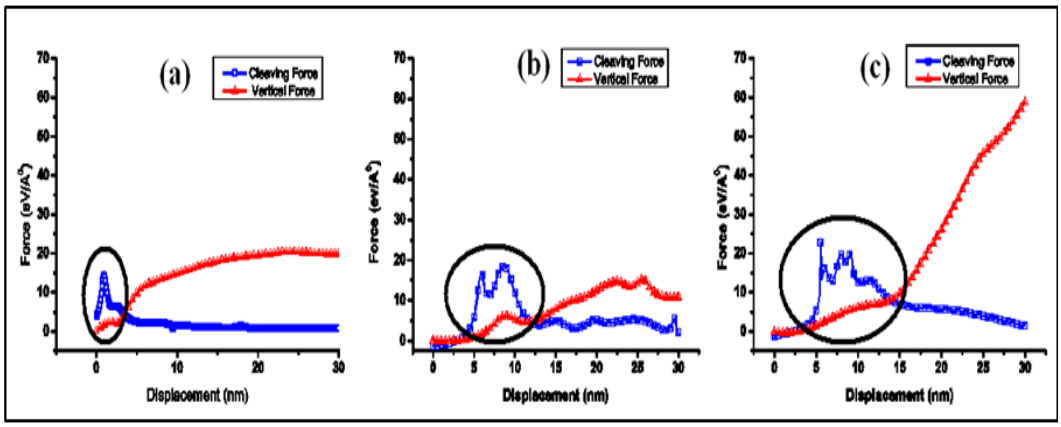

Figure 4.23: Forces profiles at DOI/R=0.82; (a) Wedge radius=2.45 A^0 , (b) Wedge radius=5.46 A^0 , (c) Wedge radius=11.6A^0 under ultrasonic vibration

and the layer generation modes are almost similar to that without oscillation as shown in fig.4.22. Similar to the earlier study, the forces are recorded and plotted in Fig.4.22. It is also similar to that of cleaving without application of oscillation that reported in earlier fig.4.23. This simulation study shows a very little effect on the applied oscillation. Therefore, further comprehensive studies may required to investigate the influence of oscillation.

4.7 Summary

Molecular dynamic simulations were used to understand the wedge based mechanical exfoliation of HOPG. The simulations show that separation, folding and shearing of graphene layers can be expected depending on cleaving conditions. Such separated, folded and sheared layers were also seen in the experimental results (chapter 3). This study also revealed that the placement of the wedge position is critical in controlling when shearing, folding and bending occur. Folding of layers is found when the wedge is placed at less than one-third of the inter-layer distance while clear separation without any folding occurs at wedge placement beyond this limit.

Force required to cause cleaving consists of two stages and indicate that initial wedge engagement requires a larger force than continuous cleaving of the layers. Shearing of graphene layers were observed during wedge exit as the wedge approaches the end face of the HOPG material. Shearing was seen to be affected both by speed and *DOI*. These simulation results provide valuable insight into the process that help in choosing suitable parameters such as position of wedge, cleaving speeds and boundary conditions to produce particular type of graphene layers.

Simulation also show that wedge radius or wedge bluntness has a significant effect on layer initiation modes. Cleaving with a larger edge radius, wedge causes layers to undergo buckling; larger the radius more the buckling effect. The buckled layer then suddenly unbuckles and releases over the wedge face over the blunt wedge. A critical *DOI* of 1.6 A^0 is seen necessary for a single layer to be separated; hence with accurate positioning and an atomically flat HOPG surface it is possible to mechanically cleave a single layer. The critical *DOI* value is seen to be independent of wedge radius. Forces and specific energy calculations also show the strong effect of wedge radius on the process. Simulations were further used to study the effect of ultrasonic oscillations.

Table 4.3: Factors affecting the nature of the exfoliation-though molecular simulations

Controlling Factor	Wedge	**Range**	**Type of FLG layers produced**
Wedge Position / Wedge Radius	Sharp	1/3 <DOI <1	Folded layers
	Blunt	0 <DOI <15.6 A^0	Folded layers; minimum DOI of 1.6 A^0 needed to form layer
	Sharp and Blunt	DOI <3 A^0	Significantly larger specific energy
Rake Angle	sharp	-17.5 to 50 ^{0}	Folded and unfoldedlayers but no scroll formation

Table 4.4: Summary of the parameter and model results validation

	Factors	**Method of Validation**		
		Experiments	Simulations	Analytical Model
Parameter Validation	Potential Function		Litreature records	
	Spacing between layers	Experimentally obtained (Literature records)	The spacing was measured after the energy minimization of the model	
Model Results Validation	Flat, folded and sheared layers	Own experimental observations	Own simulation observations	
	Process Signatures (Forces)		Simulation obtained forces	Theoretically reported values
		The trend of the experimental forces	Trends of the simulation forces	
		Comparison on magnitude of the experimental cleaving force 20 N /mm x10^2 and vertical forces 2.9 N/mmx10^2	Comparison on the magnitude of the simulated cleaving force 1.3 N/ mm x10^2 and vertical force 0.32 N/mm x10^2	

Chapter 5

FORMATION OF CARBON NANOSCROLLS

As reported in earlier chapters, the WBME process produced some interesting layers consisting of various rolled structures. These structures are identified as carbon nanoscrolls (CNS). Carbon nanoscrolls of various forms are observed. We present two hypothesis of how such scrolls form. The first hypothesis is based on microscopy evidence of pre-existing folds in layer edges of the HOPG. The second hypothesis is based on literature evidence that graphene sheets when subject to deformation can result in defects on the torn edges. The sample preparation process can induce such defects in the HOPG layers. We show using molecular simulations that the interaction of the moving wedge with certain fold geometries can trigger scroll formation, confirming the first hypothesis. To test the second hypothesis, we show using molecular simulations, that layers with edge defects, upon interacting with the moving wedge, can also form scrolls. In reality, both these factors could simultaneously cause scrolls to form. Opportunities exist in fine-tuning this wedge-based mechanical exfoliation process to synthesize CNS for use in potential applications.

Section 5.1 presents relevant literature reports of carbon nanoscrolls. The next section describes the experimental observations of scroll formation. The following section presents molecular dynamic investigations to support the two hypotheses.

5.1 Background of Carbon Nanoscrolls

Carbon nanostructures in various forms such as graphene sheets, carbon nanotubes (CNT), and more recently carbon nanoscrolls (CNS), have been proposed for use in the development of nano-structured devices due to their unique properties [180]. The structure of CNS is somewhat similar to a multi-walled CNT, but with a spirally rolled up geometry and open edges at the ends. In contrast a CNT has closed edges that while providing rigidity to its structure can be undesirable since changes to its internal diameter are difficult to induce as required in several applications. The diameter of CNS can be changed by intercalation making them suitable for use in nano-mechanical devices [181]. By changing the diameter CNS gain incredible amount of volume nearly six times more than the starting material graphite [56]. Also CNS display high carrier mobility, mechanical strength comparable to graphene and CNT [181]. Its ability to be chemically doped and capability for hydrogen storage [182] make CNS viable for use as energy storage super capacitors and batteries. Other potential applications of CNS include tunable water and ion channels as well as tunable gene and drug-delivery systems [183]. These potential applications can be realized only if CNS can be fabricated effectively.

Many methods for fabricating CNS have been proposed with literature. One method reported earlier makes use of an arc discharge [184]. When a dc arc is stuck between a graphite electrode and a carbon block [185] CNS have been observed in the graphite whiskers formed. These graphite whiskers are observed to be in the form of

concentric tubes, much like rolled up sheet of graphite layers, spanning the length of the whisker. Carbon nanoscrolls have been also reported to form in high energy ball milling process used to make natural graphite powders in an argon atmosphere [4]. Besides these methods, several chemical routes have also been proposed. Production of CNS is reported using a potassium-based [186] and acceptor-type [187] intercalation compound. In an independent study [56], a similar chemical method has been used to produce scrolls however only upon sonication; the role of sonication remains to be clarified. In a different chemical process [181], controlled addition of isopropyl alcohol droplets is used to control scrolling of graphene monolayers; the monolayers are obtained using the scotch-tape method of mechanical exfoliation.

Conditions that facilitate scroll formation have also been investigated using molecular simulations. A molecular dynamic (MD) simulation study reported that substrate-supported scrolling of a graphene monolayer is initiated when a CNT is placed on one end of the monolayer [180]; the CNT is reported to reduce the energy barrier needed to form an overlap leading to scroll formation. In another study, water nanodroplets have been used to guide folding and scrolling of graphene sheets [188]. The formation of CNS from its planar structure must be accompanied by an energy assisted process [189]. In summary, while many techniques have been proposed so for CNS synthesis, the experimental techniques attempted thus far display poor reproducibility due to lack of ability to fine-tune the process. Also several of the simulation based techniques proposed are yet to be verified experimentally. Thus, there is a need to continue investigation on alternative methods of CNS synthesis that is controllable and tunable.

Here, we report scroll formation observed in our previously reported technique of WBME and attempt to explain its formation. This is a controlled technique of mechanical exfoliation from highly ordered pyrolytic graphite using a wedge. As

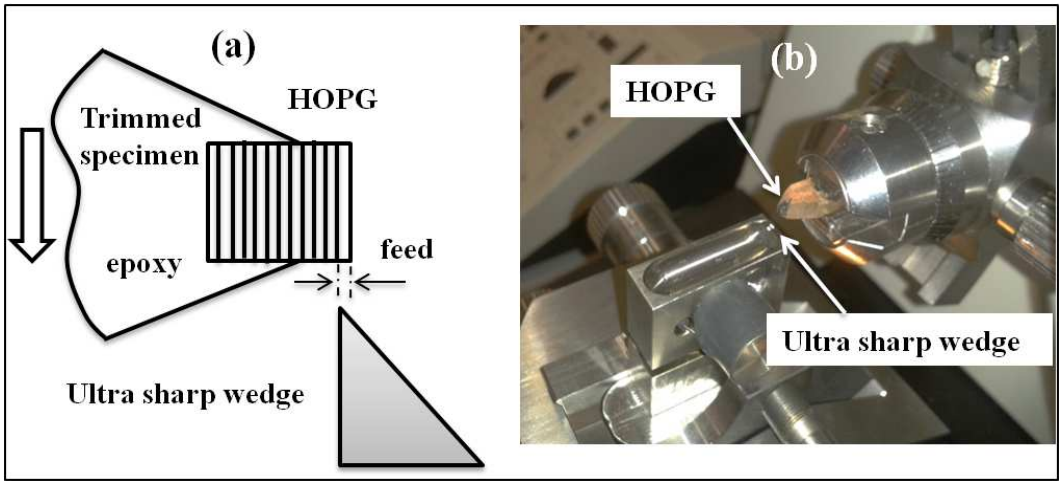

Figure 5.1: Experimental set-up of wedge based mechanical exfoliation (a) Schematic diagram showing the wedge positioned with respect to the HOPG specimen to induce cleaving (b) Experimental set up where the HOPG and wedge are placed on high precision slides for positioning and movement to cause cleaving

explained in chapter 3.2, initially, HOPG is prepared by trimming and embedded in an epoxy medium which is used to hold it in an ultramicrotome. This technique is chemical-free with only a water-bath being used to collect the cleaved layers. Some of the experiments conducted by varying controlled parameters resulted in observation of some interesting edge structures such as scrolls. Conditions that leads to such scroll formation during the wedge interaction with the HOPG is the main focus of this study. We present two hypotheses for scroll formation, both of which are based on experimental evidence. Molecular simulations show how scrolls can be form under such conditions proposed in the hypothesis. The molecular simulation results provide a fundamental understanding of CNS formation and the findings may guide to tune the experimental conditions for better quality and controllability in the production of CNS.

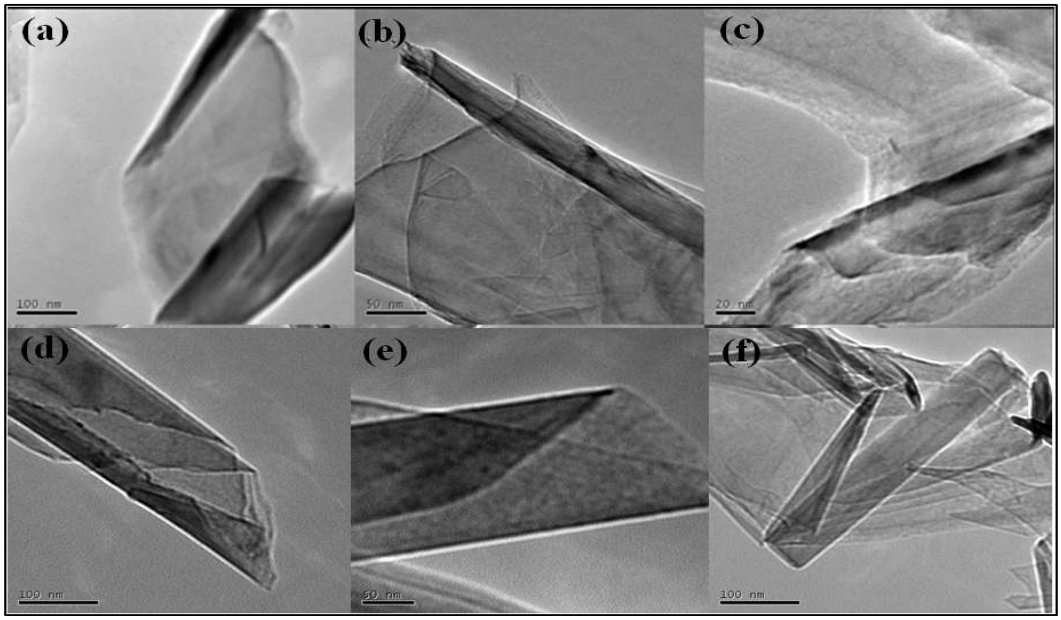

Figure 5.2: Experimentally observed nanoscrolls formation in layers synthesized using wedge-based mechanical exfoliation. Different forms of scrolls are evident: sheets with scrolls on two edges (a); fully rolled up sheets (b, f); stack of sheets rolled together with axial sliding of the roll creating a conical shape (c, d, e).

5.2 Experimental Observations of Scroll Formation

The cleaved layers were collected and examined using Transmission Electron Microscopy (TEM). The TEM images revealed that various forms of nanostructures are present in the collected samples, such as flat, folded, and scrolled structures. In this study, the focus is on the nanoscrolls. Several sample TEM images of scrolled structure are shown in fig.5.2. Various sizes of nanoscrolls are observed and the measured scroll diameters ranging from 30 to 120 nm. Nanoscrolls appear in different forms such as graphene sheets partially rolled up on their two edges (fig.5.2a), completely rolled sheets (fig.5.2b & f), and several sheets stacked and rolled together with some rolls partially slid out axially (fig.5.2c, d & e).

CNS Formation Hypothesis

The scroll formation was investigated in several directions as indicated in the table 5.1. The effect of rake angle was investigated with a sharper wedge as indicated in fig.5.3a. The negative rake angle of -17.5 degrees with unfolded layers did not form any scrolls. The same no scroll formation was observed even after starting with a partial fold at the same negative rake angle as in fig.5.3b. The similar result was noticed when the rake angle changed to the positive rake (50 degrees) and it reported in the dissertation under section 4.3 (figure 4.5 and 4.6). The effects of wedge radii and the wedge positions were discussed in the section 4.5 and the findings revealed that these factors did not cause the scroll formation. Angled wedge and the speed of the wedge provide the same results. Hence, we present two conditions under which scrolls can form: one, due to presence of pre-existing folds on the layer edges and two, due to the presence of certain type of defects in the edges. When the moving wedge interacts with the layer edges both these factors can trigger scroll formation.

Our first hypothesis attributes pre-existing folds on the edges of the HOPG layers as a source of scroll formation. This hypothesis follows naturally from our observations of side walls of the HOPG. The side walls of the HOPG sample, where the wedge will penetrate into, after peeling using a scotch tape to remove any attached dust particles shows presence of folds/curls on the free surface layer edges (fig.5.4a). Such folds, upon interacting with the penetration wedge, may further develop into various shapes of scrolls due to the continuous energy supplied by the moving edge. This is much like folding a carpet or sheet of paperyou start with a fold and supply energy to roll it up.

Our second hypothesis is based on reports that graphene layers with stresses on their edges induced by the presence of defects causes the spontaneous curvature on the edges [125]. Such edges upon interacting with the moving wedge could lead to scroll

Table 5.1: Effects of various factors on scroll formation

Factor	Range	Results
Rake angle (Degree)	-17.5 <rake angle <50	No scroll formation
Angled wedge (Degree)	6 <Angle<15	No scroll formation
Wedge Radius(A^0)	Sharper (2.45)	No scroll formation
	Larger (11.60)	No scroll formation
Wedge Position (A^0)	0<DOI<15.6	No scroll formation
Wedge speed (m/s)	50 , 100, 500	No scroll formation

formation. The basis of our speculation that such edge defects are indeed present in our sample is based on another earlier study [190], that reported presence of edge defects on a graphene sheet upon creating a hole using electron beam irradiation in a TEM. This study reveals specific defective structures such as pentagons and heptagons formation when a graphene sheet is subjected to edge damage leading to reconstruction of edges. During our HOPG sample preparation process, we trim the HOPG with a sharp cutting edge (fig.5.4b) to facilitate embedding in an epoxy. Further trimming is carried out to remove the embedded medium around the HOPG material. The trimming process by its very nature damages the graphene layer and can hence generate defective edges (fig.5.4b).

We performed molecular simulations to investigate whether these two hypotheses can lead to scroll formation. The discussion starts with the hypothesis of previously existing curls on the edges of the HOPG layers rolling up due to the action of the moving penetrating wedge. Then, we present a study on the second hypothesis on the defective edges that curl to form scrolls.

The molecular dynamic simulation model used to test the hypothesis comprises of two major components; the material and the wedge. The HOPG is modeled as layered graphene sheets. We use Large-scale Atomic/Molecular Massively Parallel Simulator (LAMMPS) package [109] with Adaptive Intermolecular Reactive Empirical Bond Order (AIREBO) potential [157] to simulate the long and short range of

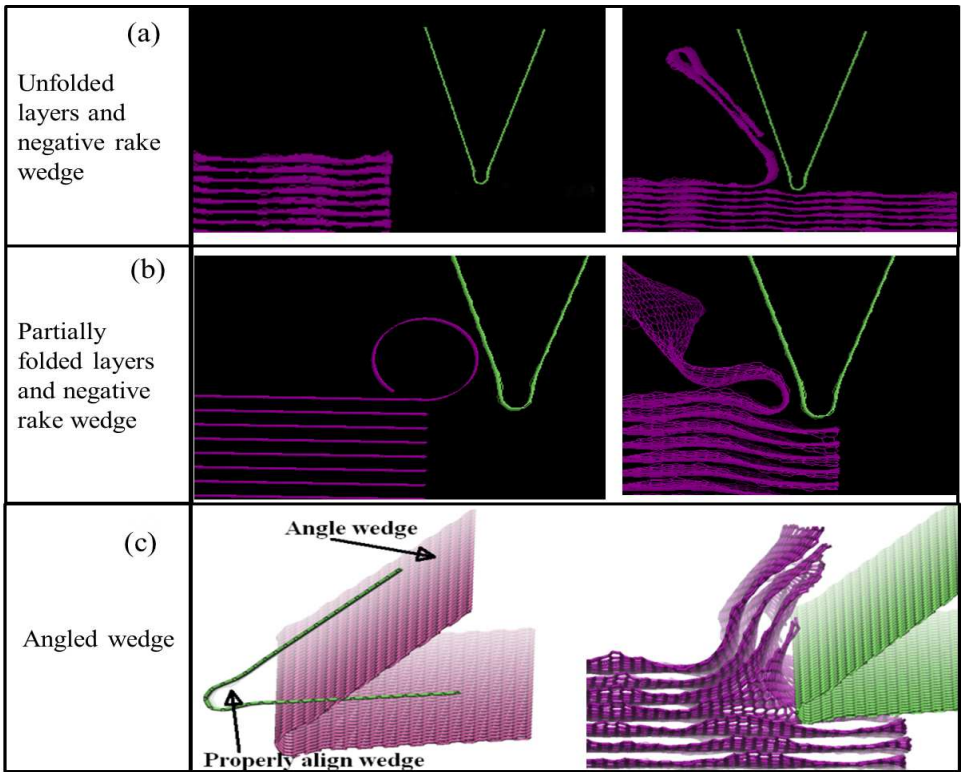

Figure 5.3: (a) Investigation of scroll formation with rake angle -17.5 ^{0}. (a) Simulation starts with unfolded sheets and resulted only a folding layer. (b) Under the same conditions, the simulation started with a partially curved layer and resulted again, only a folding layer. (c) The effect of the angled wedge positioned at 15 ^{0} with respect to the properly aligned wedge; continuing the cleaving with a such wedge (radius -2.45 A^0) resulted only a folded layer as similar to earlier

carbon atom bonds. This potential includes the van der Waal interactions to capture the inter layer binding energy. The material, HOPG, consists of a set of fixed and free atoms. The fixed atoms are used to mimic the boundary, which are at the bottom and the left end of HOPG and free unconstrained atoms are used to model the rest of the HOPG structure. The Lennard Jones (LJ) potential is used to represent the interactions between wedge and the material with selected cut off values. The diamond wedge is modeled with an included angle of 35 ^{0} and wedge radius of 2.4 A^0. The exfoliation process is performed in the x-direction on the (001) surface of the HOPG block by moving the wedge towards the HOPG block with a constant speed. The wedge is considered as a rigid body during the entire simulation. Sim-

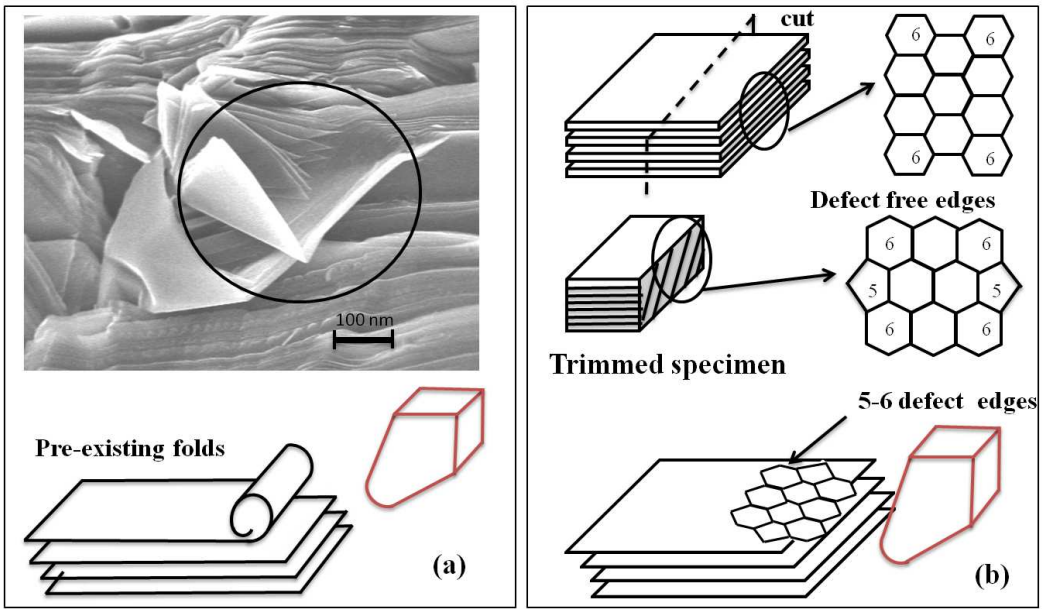

Figure 5.4: Hypotheses for scroll formation ;(a) Pre-existing folds hypothesis; view of the scotched tape peeled side-surface of the HOPG sample indicate presence of folds/curls or distorted sections before exfoliation; wedge interacts with such folds may wind newly exfoliated layers around the pre-existing folds, (b) Defective edge hypothesis; the HOPG trimming process defective edges on a planar graphene sheet. This can trigger scrolls to form when energy is supplied by the moving wedge which also releasing layers.

ulations are conducted at a constant temperature of 300 K to mimic experimental temperature conditions. In our previous work, we showed that few layers of flat graphene can be exfoliated from the HOPG without defects or pre-existing scrolls. Here, simulations are conducted to study under what conditions scrolls can form in exfoliated graphene layers. In one model, the HOPG layers are built as defect free structures with pre-existing folds and in the second model, we introduce defects on layer edges to explore the process of scroll formation.

1. ***Scroll Formation Using Previously Existing folds on Layer Edges***

We start our simulations with various pre-defined folds as shown in fig.5.5a-c. First two folded structures (a) and (b) do not have any overlapping segments. These folded structures are built by folding a planar graphene (defect free) sheet. The

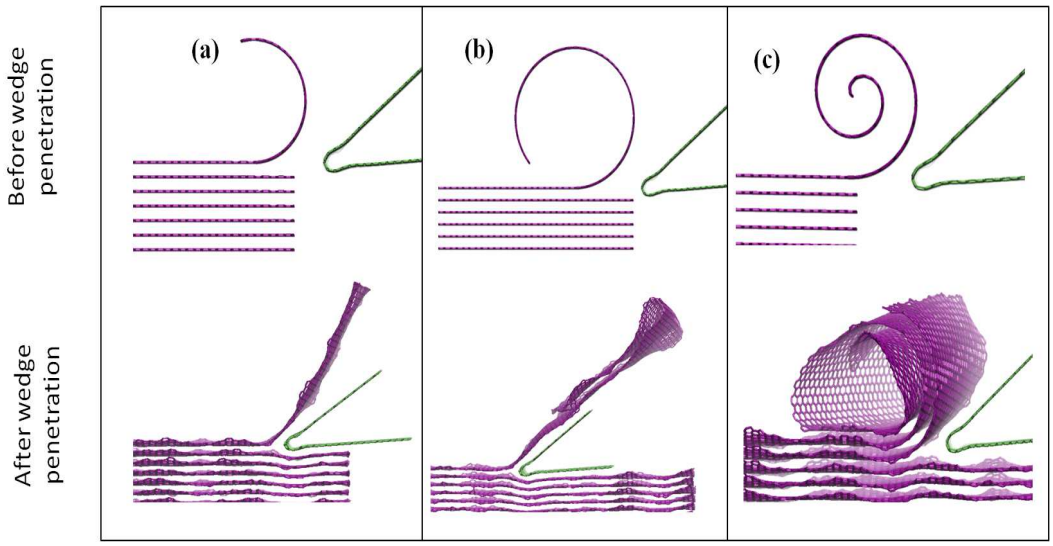

Figure 5.5: Molecular layered structure with pre-existing initial scrolls/folds and a rigid wedge. (a) and (b) structure starts with a predefined fold of various geometries on the edge. This kind of structure does not form nanoscrolls; instead, they unwind completely and produce either flat or folded structure. (c) Complete pre-defined scroll as in results in scrolled layers sliding out and forming a conical shape similar to experimental observations.

wedge is positioned in front and below the pre-folded HOPG layer. The distance from the HOPG top surface to the lowest atom at the bottom of the wedge (cleaving depth) is set to 2 A^0. The cleaving depth determines the number of layers that will exfoliate from the bulk HOPG. Simulations are carried out at 300 K fixed temperature with a time interval of 1 femto-second and wedge penetration speed of 1 A^0/ps. The initial shape of the fold is found to be important in scroll formation. With a pre-existing fold without an overlapping section, as shown in fig.5.5a and b, wedge penetration causes complete unwinding of the pre-existing fold. When the pre-existing fold is designed with an overlapping section as in fig.5.5c, These simulation results do not indicate any forms of carbon nanoscrolls. The overlapped structure in fig.5.5c results such geometries of carbon nanoscrolls. An involute configuration with an inner radius of 1.28 A^0. Then during simulation it reaches a equilibrium state maintaining the scrolled structure.

Before the wedge penetrates into HOPG, the system is allowed to minimize for its equilibrium structure and this causes the initial flods to partially unwind and the gap between the scrolled layers reaches value of about 3.4 A^0. As the wedge moves towards the HOPG block the layers cleave continuously and scroll around the predefined fold. The inner diameter of the equilibrated scroll is about 20 A^0, in good agreement with stable CNS diameters reported [189]. During the initial simulation process, imperfect scrolls are observed. These are caused by the large initial scroll diameter as well as mechanical stresses imposed by the high wedge speeds. Atomic relaxation during attainment of equilibrium results in perfect scrolls. As further scrolling proceeds, the conical form of scrolls are also observed due to the non-uniform relative sliding in the scroll (fig.5.5c) similar to the experimental observations shown in fig.5.2. However, with a small diameter of initial fold sliding is not observed and leads to formation of perfect scrolls.

Increasing the cleaving depth produces multilayered nano-scrolls (fig.5.6a) and the cleaved layers wind around the initial equilibrated CNS. The initial single scroll is enough to continue the scrolling of multilayer scrolls due to the van der Waals interaction between the scroll and the exfoliated cleaved layers. From fig.5.6a, we can also find that bond formation occurs occasionally between the scrolls/layers caused by active edge atoms due to the wedge impact during engagement. If the initial fold diameter is much larger than 20 A^0, the scroll is unstable and forms a folded structure with continuation of relative sliding of the layers as the wedge moves (fig.5.6b). Hence, the geometry of the initial fold plays an important role in determining the nature of the CNS finally obtained.

In our previous studies, we observed that the relative wedge position with respective to the HOPG (depth of cleaving) plays an important role in layer cleaving. In the current study, we also observed that the wedge position plays an important

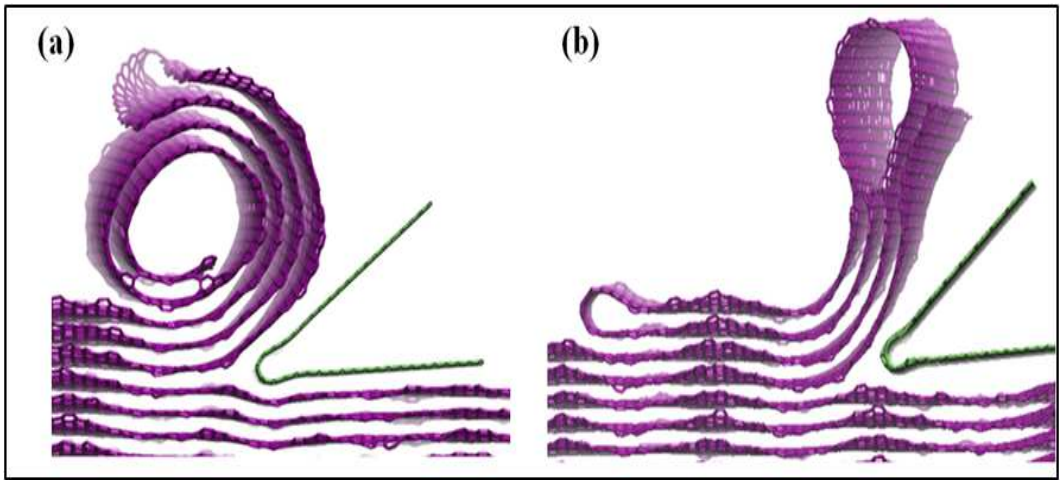

Figure 5.6: Effect of the initial fold; (a) Scrolling at a larger cleaving depth (8.8 A^0) generates multi-layer scrolls (b) Starting with a higher initial fold radius results in equilibrating to a different scroll shape with additional cleaved layers rolling up on to this same shape.

role in controlling the structure of the scroll. We conducted simulations at several wedge positions and the different scrolled structures formed are illustrated in fig.5.7. Initially when the wedge is kept at cleaving depth of 2 A^0 below the reference surface it found that cleaving action continued with the removal of an additional layer (besides the already scrolled up initial layer) as shown in fig.5.7b. This is because, before the start of wedge penetration the system energy is minimized and during this process the layer adjacent to the pre-formed fold forms a partial scroll due to van der Waals interaction. Further wedge penetration causes the additional layer to continuously scroll on the pre-existing folds as shown in fig.5.7b. When the wedge is placed above the HOPG layers (i.e negative depth of cut) as indicated in fig.5.7c, only the layer with the pre-existing fold continuous to scroll. No other layers are cleaved under this condition.

2. ***Scroll Formation due to Defects on the Layer Edges***

As discussed earlier, there is a possibility for defects to occur on the HOPG sample

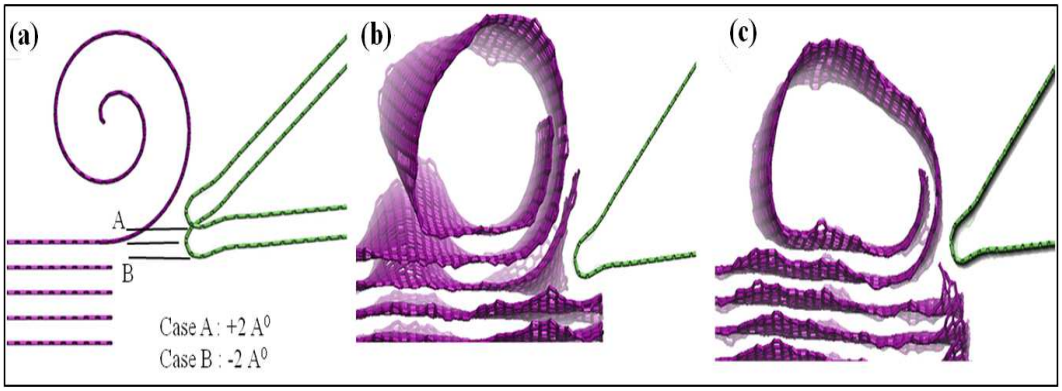

Figure 5.7: Effect of wedge position on scroll formation; (a) Illustrating wedge position at two different cleaving depths, (b) Scroll formation at a cleaving depth of 2 A^0 - wedge is seen to cleave and scroll up additional layers, c) Scroll formation at a cleaving depth of 2 A^0 above the HOPG top layer; the wedge cleaves only the initial folded layer and no additional layers are cleaved.

during the trimming process. The effect of the edge defects (fig.5.8) on the morphologies have been studied and the resulting edge stress quantified for various types of edges [44, 125, 190]. The nature of edge stress can be either tensile or compressive and especially pentagon-hexagon (5-6) type edge defects can lead due to large edge stress resulting in curling [191]. We first study the influence of this type of edge defects on a free standing graphene sheet by introducing 5-6 defects on the armchair edge of the graphene sheet and then relaxing the structure to its minimum energy state. Due to the tensile stress caused by 5-6 edges, the flat graphene transforms to a curved/scrolled shape at the equilibrium state. The stages of spontaneous curling are shown in fig.5.9. The sheet starts to crumple and then form a S shape at 75 ps, and continuously changes its shape and finally forms a completely scrolled structure. The potential energy (fig.5.9) indicates the 5-6 edge graphene sheet is energetically unfavorable and it will come to a stable state by scrolling. Some of these observations have been noticed in the experimentally cleaved layers, specially the S shaped rolling, reported in the literature. We now study the effects of inducing such type of defects on mechanical exfoliation caused by the wedge.

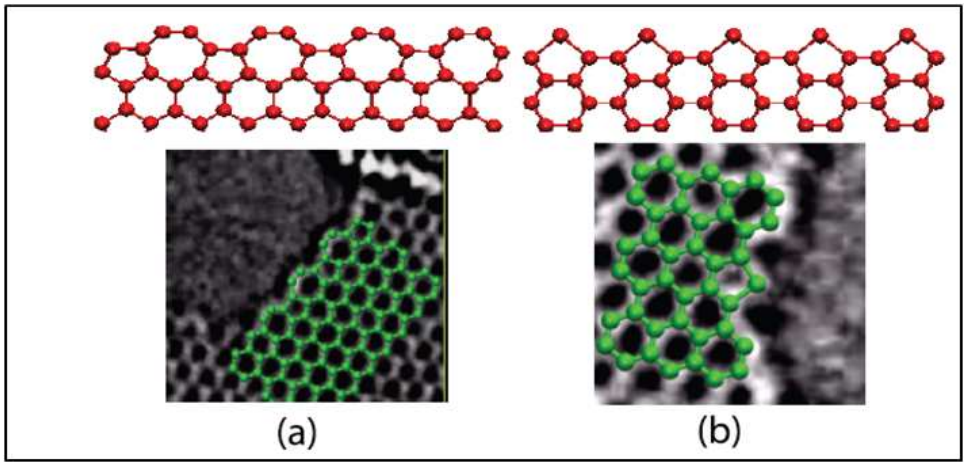

Figure 5.8: Graphene sheets with defect edge structures; Top raw indicate the (a) zigzag edges reconstructed with pentagon & heptagon (5-7), (b) Armchair edges reconstructed with pentagon& hexagon (5-6) structures, respectively. (Bottom) Reconstructed structures observed in recent experiments [125]

Defective edges are introduced to the top layer of the HOPG stack. The 5-6 reconstructed structure is introduced to the first (top) layer and other layers are defect free (fig.5.10). Initially the entire structure exhibits a flat shape including the defective edge layer due to van der Waals interaction between the adjacent layers. Once the wedge engages, the top layer initially bends (fig.5.10a-1, 10-b1 and 10c-1) and transforms to a scrolled shape (fig.5.10a-2, 10b-2 and 10c-2). Initially the cleaved layer can bend either away or towards the HOPG depending on the initial impact as well as the penetration depth of wedge. Once the layer bends away from the HOPG then complete scrolling of layers is observed as the wedge moves inside HOPG (fig.5.10a, 10b). However, if it bends towards the HOPG then the top layer initially folds and then forms a scroll with a large diameter as shown in fig.5.10c-1 and c-2. The staring position of the wedge is seen to affect scroll formation; with single scroll formed when the wedge start closer and multilayer scroll fold when the wedge stats further away. In the absence of any defects in the top layer, the cleaved layers do not fold or scroll and remain flat as reported previously.

During the simulation process, the force acting on the wedge is captured as shown

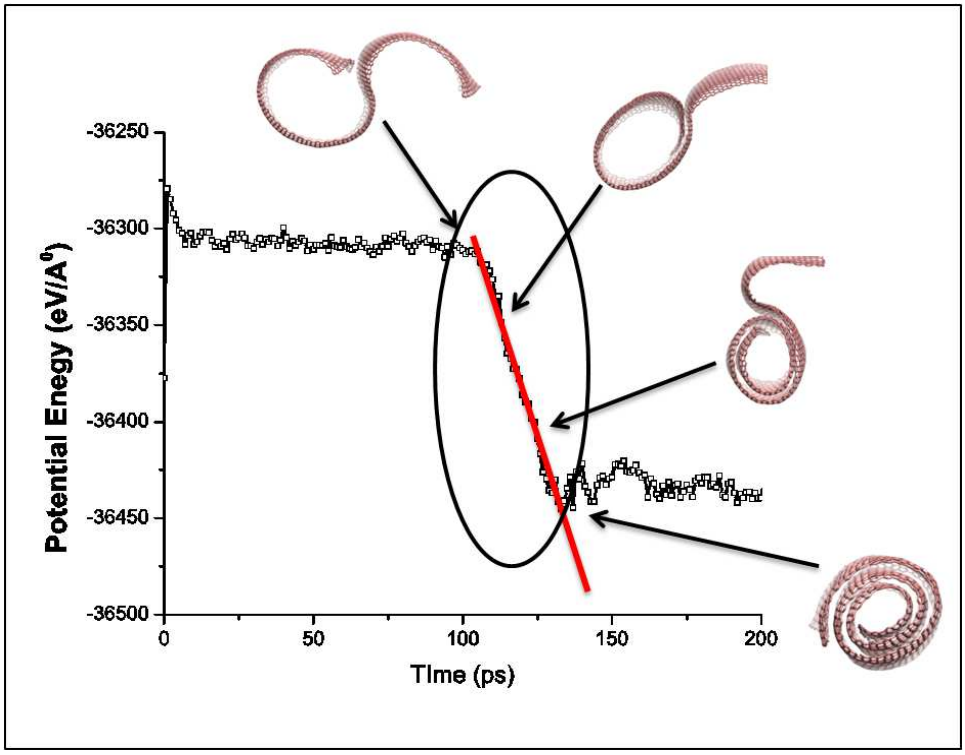

Figure 5.9: Variation of potential energy and development of scroll formation after inducing 5-6 defects on the armchair edge of a free standing graphene sheet ; A planar sheet rolls into an S shape after 75 ps, starts forming CNS after 100 ps and the fully wrapped CNS forms after 135 ps.

in fig.5.11. The horizontal forces acting on the wedge, called as cleaving forces, are responsible for scrolling the layers. In pre-existing scrolling without any defects at its edges (fig.5.11), the cleaving force profile shows that there is a significant initial peak during the wedge engagement at the time of initial scroll formation. Once cleaving starts and scrolling proceeds, the cutting force reduces reaching a low steady state value. The energy required for this process must be just enough able to break the weak van der Waal forces between the layers on HOPG. The low steady state scrolling force value could also be due to the self-induced scrolling nature of process requiring very little energy for further scrolling. In defect induced scrolling (fig.5.11), lower magnitude of initial scrolling is observed. Spontaneous curvature due to the defective edge structure may reduce the initial effort that required for scrolling.

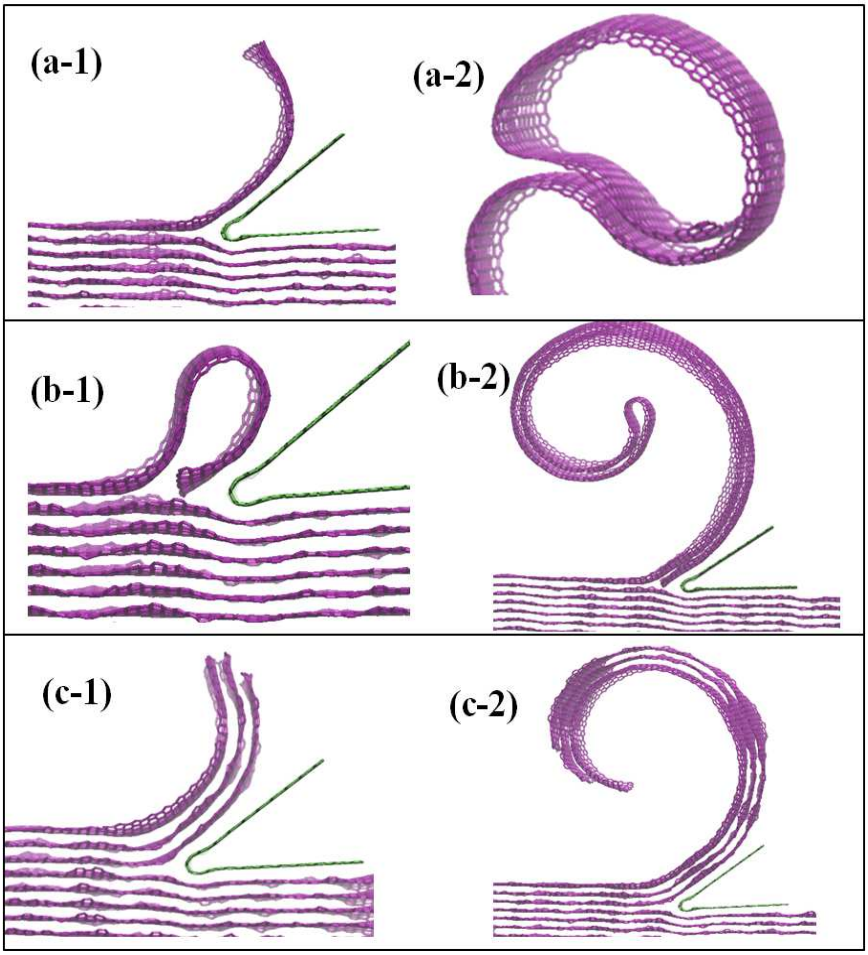

Figure 5.10: Effect of 5-6 type of defects during the exfoliation process; (a-1) and (a-2) starting with clean separation and single layer scrolling (DOI at $2A^0$), (b-1) and (b-2) starting with a bent layer and ending with multilayer scrolling (DOI at 2 A^0), (c-1) and (c-2) starting with clean multilayer and ending up with multi layer scrolled structure (DOI at 8.8 A^0).

We noted that from the literature theoretical models that deal with scrolling or unscrolling of CNS under certain conditions. For example, one of the cited papers [192], presents a model where the inner radius is held fixed (equal to that of a CNT placed inside). Even though the scrolling we presented happens at slightly different conditions (e.g. larger radius scroll with less bending without presence of any CNT, with presence of edge defects etc.) we performed a theoretical analysis using presented model [192] to compare the effects of our cleaving with and without scrolling. The model in [192] predicts a scrolling energy release of 0.06-0.08 nN/nm.

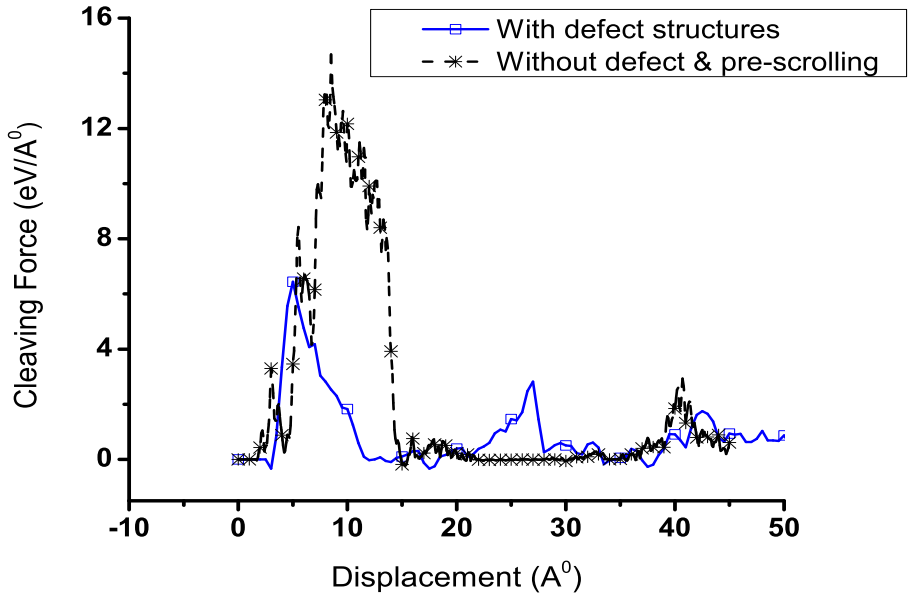

Figure 5.11: Comparison of cleaving force at cleaving depths of insertions at 2A^0 in pre-existing fold with and without any defect structures; larger initial peak and lower steady state value indicate the effect of initial wedge engagement and self-induced scrolling nature of process. Defect induced structures display a less force at wedge-material interface.

This translates to a driving force of about 0.472 nN (0.295 eV/A^0) for our 5.9 nm wide sheet. With scrolling releasing energy the force/energy needed for our cleaving should be less than without scrolling. We had earlier reported in the dissertation that the theoretical force needed for our cleaving (without any scrolling) is about 0.8 eV/A^0 for our 5.9 nm wide sheet based on overcoming van der Waals interactions between the sheets. Hence, with scrolling, the cleaving force needed is 0.8 0.295 eV/A^0 = 0.5 eV/A^0. We can see from our force profile plots (fig.5.11 in our thesis) that the steady state forces reach a value close to this; dynamic effects do create some spikes in the force profile, but overall the average forces reach this value.

We analyze the potential energy during the formation of carbon nanoscrolls both with pre-existing folds and with defective edges (fig.5.12). A positive slope indicates that a constant energy is required to exfoliate the graphene layer from HOPG and in

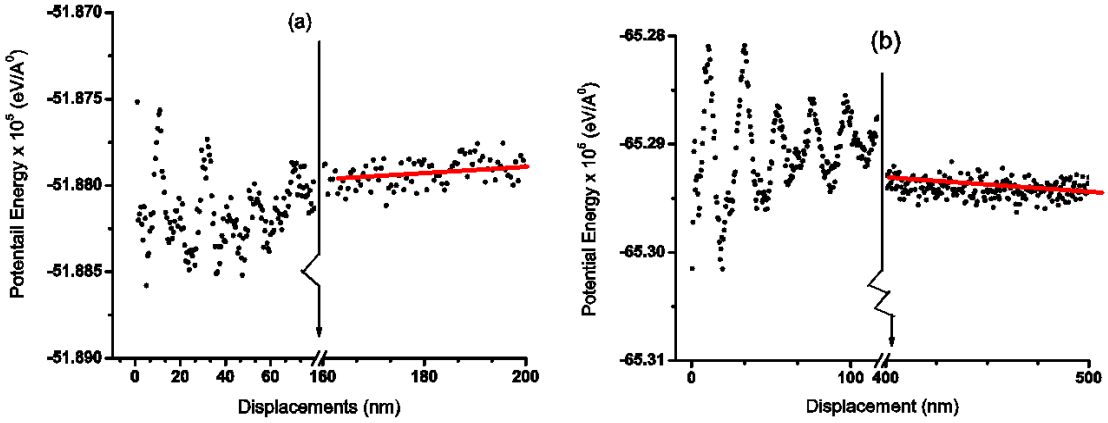

Figure 5.12: Comparison of without (pre-defined) and with defect scrolling; (a) and (b) indicate the variation of potential energy against the displacement, initial section showed the stick slip type of variation and fitted liner curve in enlarge potion indicate a increasing and decreasing pattern

the presence of pre-existing fold the exfoliated graphene itself transforms to complete scrolls due to van der Waals interaction. A negative slope in energy indicates that a small perturbation or initial force is required to break the van der Waals interaction and then the 5-6 edge layer transforms to a scrolled structure for its most stable state. By increasing the depth of cut, both (with initial fold and edge defects) structures need a constant external force to exfoliate and then the exfoliated layers transform to multi layered scrolled structures. In both cases, a positive slope in potential energy is observed due to exfoliation of multiple-layers and the associated bending is an energy intensive process during scrolling.

The simulation studies show opportunities that are available to control the CNS formation by manipulating several factors. These include: introducing folds of various dimensions, controlling wedge starting position horizontally and vertically, controlling the nature and the type of defects, introducing defects in several layers above and below the wedge. We acknowledge that not all factors can be well controlled, but speculate here that some of them are. For example, selective electron beam irradiation could be performed to introduce layer edge defects at several layers prior

to wedge exfoliation. The introduction of layer defects, not just in the top layer, leads to interesting scrolling of the layers as the wedge penetrates (these simulation results are not shown here). Controlling of the wedge position is easily achieved by precisely controlling the positioning stages. Introduction of folds of certain selective dimension can perhaps be undertaken if we better understand the effect of mechanical trimming on the layer edges; a special pre-processing step could then introduce such folds prior to wedge based exfoliation. Hence, controlling a set of factors can lead to many interesting carbon nanoscroll structures.

5.3 Summary

In summary, we report the formation of carbon nanoscrolls experimentally when exfoliating HOPG mechanically using a sharp moving wedge. Scrolls were observed in various forms and two hypotheses are presented for this scroll formation. The first is based on the hypothesis that pre-existing folds in layer edges cause the CNS to be formed when the wedge penetrates. The second is based on the fact that stressed edges, caused by the defects, can induce scroll formation. Molecular dynamic simulations with pre-existing folds show that the initial fold structure and wedge position (cleaving depth) are important parameters in the formation of CNS. The force profiles indicate that, compared to initial wedge engagement, a smaller cleaving force is required to continue exfoliation and scroll formation. The potential energy profiles indicate that the formation of single scroll is an energy intensive process only in the case of pre-existing scrolled structure. With defective edges, the process requires smaller energy to exfoliate and then the defective edged layer spontaneously forms scrolls. The wedge based mechanical exfoliation method shows a promising way to produce carbon nanoscrolls for future device applications.

Chapter 6

INDENTATION OF HOPG PARALLEL TO BASAL PLANE

From our experimental and simulation studies we identified that wedge-material engagement is important for layer structures to form in the WBME process. In order to understand this better we undertook micro-nano indentations of highly ordered pyrolytic graphite parallel to the basal plane. The indentation process allows us to control the depth and load leading to an understanding of the various stages of layer separation and edge structure formation. Such control is not possible within the setup used for WBME.

Section 6.1 eleborates further on the motivation for this particular study. It is followed by a description of the experimental setup used. Section 6.3 presents and discusses the results. Here particular attention is given to the various shapes of load-displacement curves seen and associated structural changes. The following section presents the Raman spectroscopic data at the indented locations.

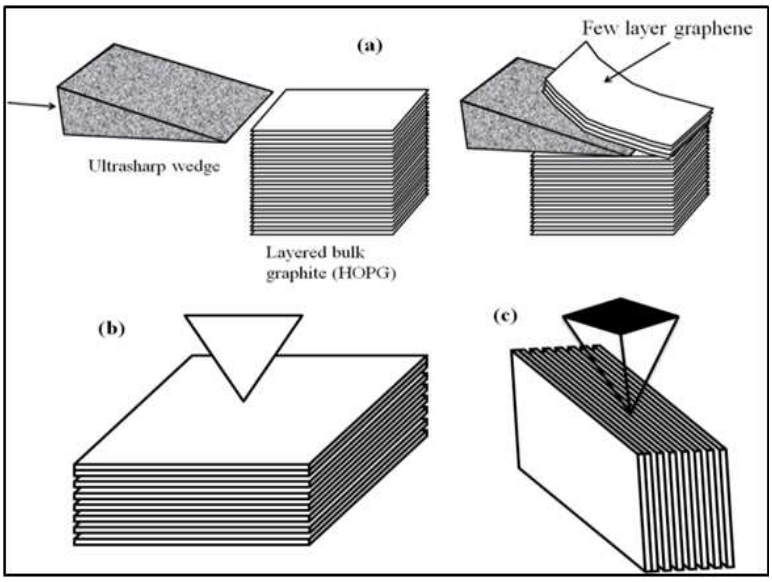

Figure 6.1: Schematic diagrams of (a) Cleaving few layers of graphene using a wedge, (b) Indentation normal to the basal plane, (c) Indentation parallel to the basal plane in graphite

6.1 Motivation

In nano-scale machining (fig.6.1a), there are many challenges for real-time process monitoring. It is also difficult to freeze the process in between to observe closely which may be possible do at the meso-macro scale (e.g. quick-stop devices have been used in meso-micro scale cutting). The ultra-microtome setup we reported earlier is not amenable to controlled stopping of the wedge or use of quick-stops. Therefore, we propose initiating process understanding through alternative means. Indentation is one alternative method available to study the machining induced deformation. This study can provide some fundamental insight to overcome the above mentioned issues in micro and nanoscale machining.

Indentation uses a sharp tool to penetrate the material under controlled conditions. Understanding material deformation behavior under indentation induced loads has been used in diverse applications such as acquiring elastic modulus, hardness, fracture toughness [193] especially in thin films [63], and assessing the residual stresses in

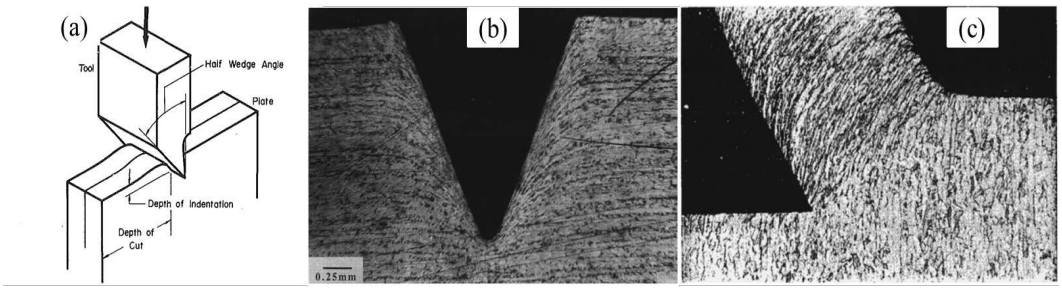

Figure 6.2: a) Plan strain wedge indentation [196], (b) Etched cross section through the center of a conical indentation in mild steel showing deformation of texture lines. Note that the texture lines are not cut by the tip of the indenter. (c) Etched cross section of a machining quick-stop specimen involving sliding of the chip over the rake face. Note that the flow lines are cut by the cutting edge of the tool [197]

.

welding [194]. There are reported attempts to utilize indentations to test the quality of particularly residual stresses on the machined subsurface through experimental and numerical investigations [195].

The WBME process is essentially a very high-rake angle orthogonal nano-machining process. The interaction of the wedge with the material can be studied in the more controlled environment of micro/nano indentation. Several discussions on indentation and its relation to machining have been reported [196–198] in the literature. Some of these discussions elaborate on the machining and relate it to the technique of hardness measurements, appropriate load values used in machining, and the relevance of hardness in multi-point machining [198]. Besides these literature also reports similarities between the machining and the indentation. In both indentation and machining, a tool is pressed against the material. As highlighted by Madhavan [197], some researchers identified the machining process as an asymmetric indentation. As emphasized in the same report, the shear-plane model is much easier to investigate in machining than the wedge indentation. However, the earlier model becomes inadequate and more complicated when examining the details of the machining process. A wedge type of indenter (fig.6.2a) has been used

to study plastic deformation occurring in metal cutting; particularly determination of the correlation between wedge indentation and incipient chip formation has been reported [196]. The comparison of flow line patterns using these two techniques has reported and shown in fig.6.2b and c. Atomistic analyses are also reported under certain conditions to compare these two processes in terms of physical phenomena. Similar comparison of indentation and machining under oblique impact also provides the conclusion that indentation can be treated as a special case of machining [199]. Atomistic analyses are also reported under certain conditions to compare these two processes in terms of physical phenomena. A molecular simulation is performed to understand the properties of subsurface deformed layers in nanocutting process with the aid of nanoindentation test [200]. Another work [201] uses indentation to explain the material removal mechanism on brittle material machining. Komanduri et. al [79] considers that indentation sliding can used to simulate the ultrapresion machining, grinding or abrasion process with the use of a blunt wedge. They also reports that the indentation process is a useful method to explain the material removal phenomena observed in nanomachining. The process of indentation is equivalent to the machining with a negative rake angle due to its high included angle. This is particularly applicable to nano-scale machining due to the size of the edge radius and the depth of cut. Another study reported the use of indentation to evaluate residual stresses induced during high speed milling [202]. Hence this is sufficient evidence to support the study of machining via indentation process. As a result, we adopted micro-nano indentation of HOPG in study the wedge-graphite interactions that happen in WBME.

Leading to this study, we investigate the existing literature more carefully on carbon related indentations. A large numbers of experimental and simulation studies are reported in graphite [203]. These studies investigate various forms of carbon including single layer of graphene [159, 204, 205]. Indentation studies of graphite,

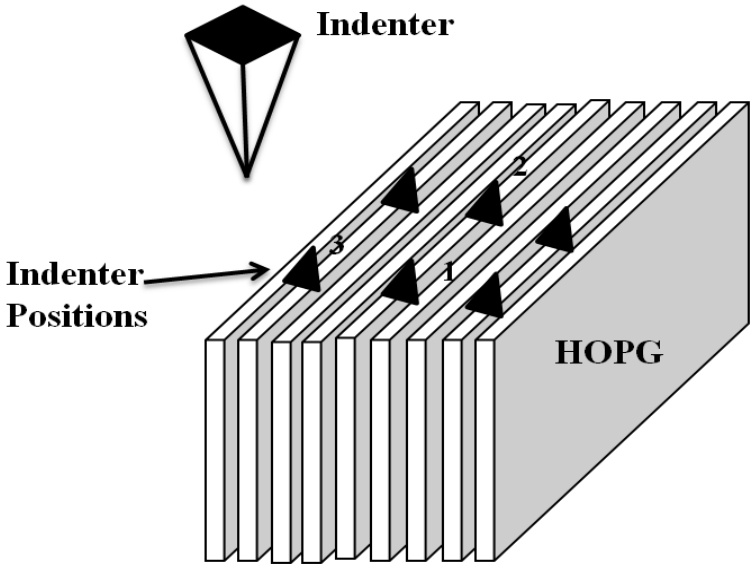

Figure 6.3: Indented positions on the HOPG surface parallel to the basal plane

especially Highly Ordered Pyrolytic Graphite (HOPG), has been reported in the literature [150]; however such indentations are carried out normal to the basal graphite plane (fig.6.1b) and this approach is not related to the tool penetrations caused by tool motion parallel to the basal plane. HOPG is highly ordered along its c-axis and widely used in many research purposes. In this study, we focus on indentations parallel to the basal plane (fig.6.1c); this is more similar to the impact of the wedge and the material engagement during cleaving of the graphitic thin films. As reported earlier, the initial wedge position and material engagement is critical to the nature of the layers obtained. We expect this indentation study to strengthen our understanding of the wedge-graphene interaction.

6.2 Experimental Setup

Indentation experiments are carried out using two indentation systems. The first series of indentations are carried out on a Matzusawa micro hardness tester. The second sets of experiments are conducted on a Nanointender XP with a Berkovich

diamond indenter (65.3^0) at room temperature. The allowable drift rate is 0.05 nm/s. The Poissons ratio of HOPG is set as 0.25 [206]. First, the HOPG sample (EMS-434-AB ZYB) surface to be indented is cleaned by peeling the surface several times with an adhesive tape. During the indentation, the HOPG sample is held using a strong adhesive tape and other props to ensure the layers are oriented in the vertical direction as shown in fig.6.1c. Indentations are then carried out at several locations targeting positions at the center (bulk) and also close to the edge (fig.6.3). Both depth controlled indentation and load controlled indentations have been carried out. We study the load-displacement curves and observe the resulting indented deformations closely using field emission scanning electron microscopy (FESEM).

6.3 Results and Discussion

We start our discussion first by presenting results of indentation trials using the micro-hardness tester. Then, we discuss the results of depth and load controlled indentations. Indenter induced damage in the sample surfaces using the micro hardness tester is shown in fig.6.4. The load applied during the indentation is 1kgf. We choose this arbitrary value to observe the damages on the surface. The micrographs show heavy distortions on the sample and evidence of brittle fracture on the subsurface. Micrometer sized layers are fractured and seen in various shapes and forms. Extensive damage around the indent area is evident and there is no clear trend in the crack paths. The cracks look like scallops which have been reported in brittle material machining [87]. This shows the damages possible to the layers during the initial wedge and material impact. In certain locations, cracks are seen to propagate between stacks of layers. This observation is also very similar to machining with a blunt wedge where material separates around the wedge radius.

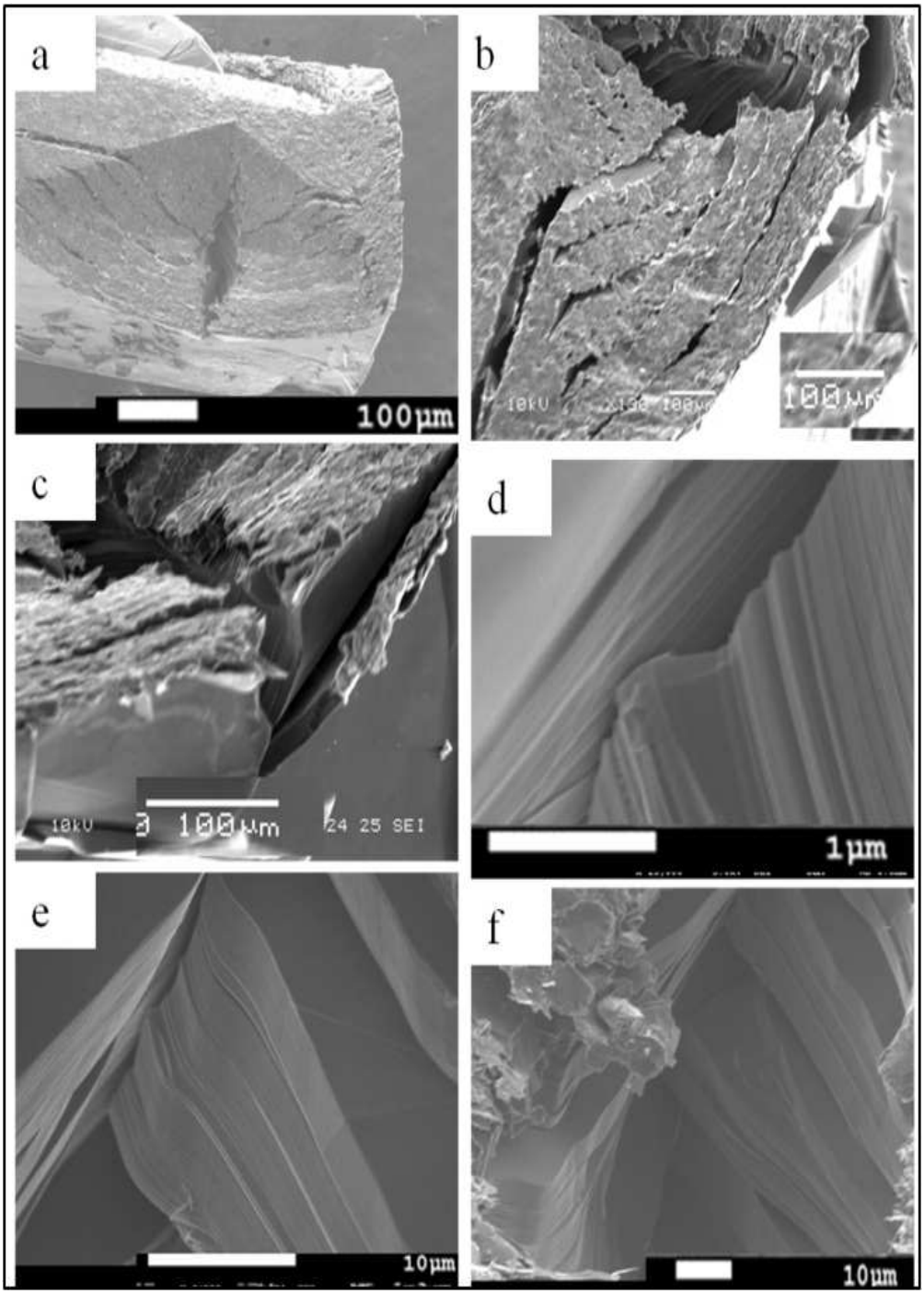

Figure 6.4: FE-SEM images of micro indentation parallel to the basal plane with a micro hardness tester; (a) Surface area under after indenter, (b) Scallop type of crack propagation, (c) Crack propagated cracks near the edge , (d),(e), and (f) Enlarged image of delaminated graphene layers

Use of the nano-indenter provides better process control that is unavailable in our WBME process. Using the Nanoindentation Xp machine, first we performed the depth control indentation. The wedge indenter tested in this experiment (Berkovich indenter) is geometrically different from the simple extruded triangle wedge that we used in our machining experiments. Nevertheless, these indentation observations can reveal some useful insights about the wedge and material engagement. Our exfoliation length of the HOPG samples is in the range of few hundred micrometers. Therefore, in this study we focus on relatively larger depths of indentations. A single indentation is shown in fig.6.5a; it shows an open loop hysteresis curve. The nonlinear loading curve is noticed with pop in and pop out events. During such events there is no change in the load but indenter continued to penetrates through the material [207]. General believe is the elastic-plastic transition is happening in this regions due to various reasons. Multiple examples are demonstrated, for instance, to track the phase transformation during such events with silicon using temperature variations [208] and electrical measurements [209]. A study on gallium arsenide reports a similar pop-in events due to the pressure induced phase transformation [210]. Studies on single gold crystals [210] as well as platinum [211] also demonstrate similar events.

We performed two sets of indentations at depths of 2 and 100 μm. At the lower depth of indentation, we observed that the moving indenter did not create significant damage to the surface. The load experienced by the indenter varies with target position with magnitudes in the range of 0-6 mN. This variation may possibly due to the nature of the HOPG layers at the indented location. In chapter 3, through the scanning electron microscopy images, we identified pre-existing defects on the HOPG. Among the defects, kinks and discontinuous layers were prominent. If the indentation happened at the locations one can expect the load to be different compared with other locations.

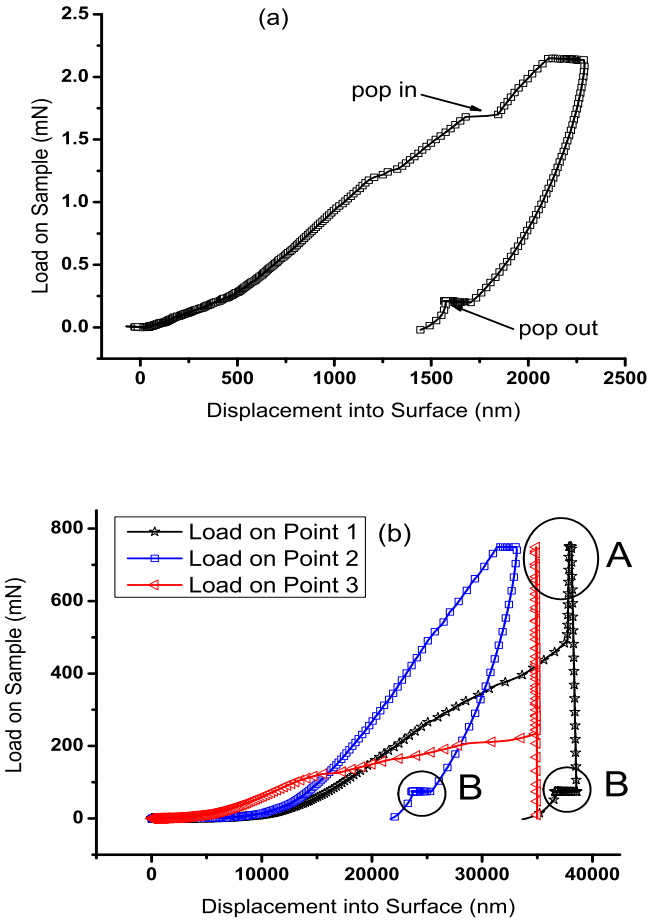

Figure 6.5: Load vs Displacement profiles (a) Single indentation, (b) Load vs displacement comparison at point 1, 2 & 3. Point 1 & 2 are in the middle of the surface and point 3 close to the edge of the samples. The load is held for a 10s period between loading and unloading

The larger depth indentations show two distinct types of load-displacement curves (fig.6.5b). From the several indentations that we performed on the surface, we chose three key indentations for discussion based on the shape of the profiles. The control of accurate indent placement is hampered by the low resolution of the in-built microscope of the nano-indenter (10X). Two indentations points denoted as 1 and 2 indicated in fig.6.5b are in the middle of the sample and display two different load-displacement profiles. The mention curve at point 1 has a monotonically increasing loading curve followed by a sudden vertical unloading. At point 2, a smooth contin-

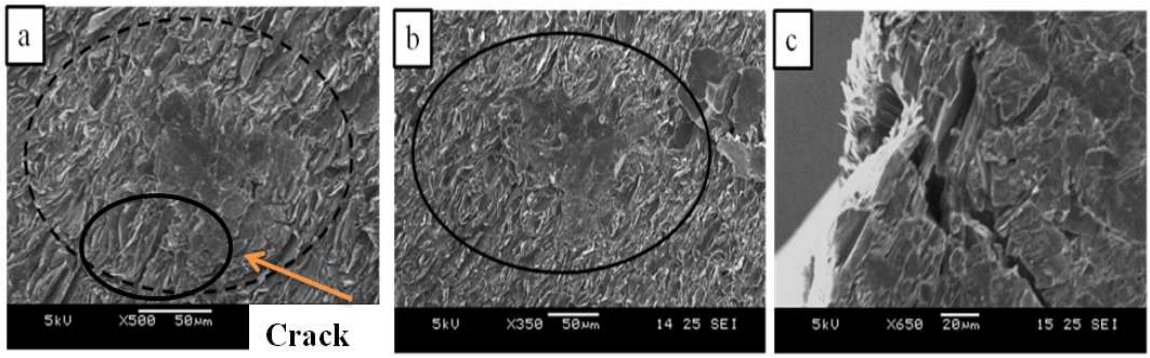

Figure 6.6: Indentation Marks on the surface signifies the depth control; (a) Point 1, (b) Point 2, (c) Point3

uous load-unload curve, without any significant events such as pop-ins and pip-outs, is observed. For these two selected cases, differences in loading rates are observed. A close observation shows that the loading curve at point 1 as having different gradients. These curves reveal vital information related to energy absorption or energy release [212].

In one of the profiles, a vertical unloading curve is observed (as circled A-fig.6.5), indicating that there is no elastic recovery. The possible reason for this is fracture of the layers as they deform plastically. There is also a short horizontal segment in the unloading curve (circled-B). These events seen to be occurring at higher loads and correlate to presence of defects and change in crystallographic orientations [212]. These pop out events may also be due to activation of pre-existing dislocations; this is highly possible in graphite. We report details of pre-existing defects in chapter 3. Pop-outs provide evidence that these locations are critical and may provide useful insights about material behavior.

In the other load-displacement profile (at point 2), smooth continuous loading and unloading curves are observed. The indented locations are closely observed in an FESEM (fig.6.6). The indentation marks point 1 shows some open cracks along the side. But the indentation at point 2 did not result in any cracks in the vicinity

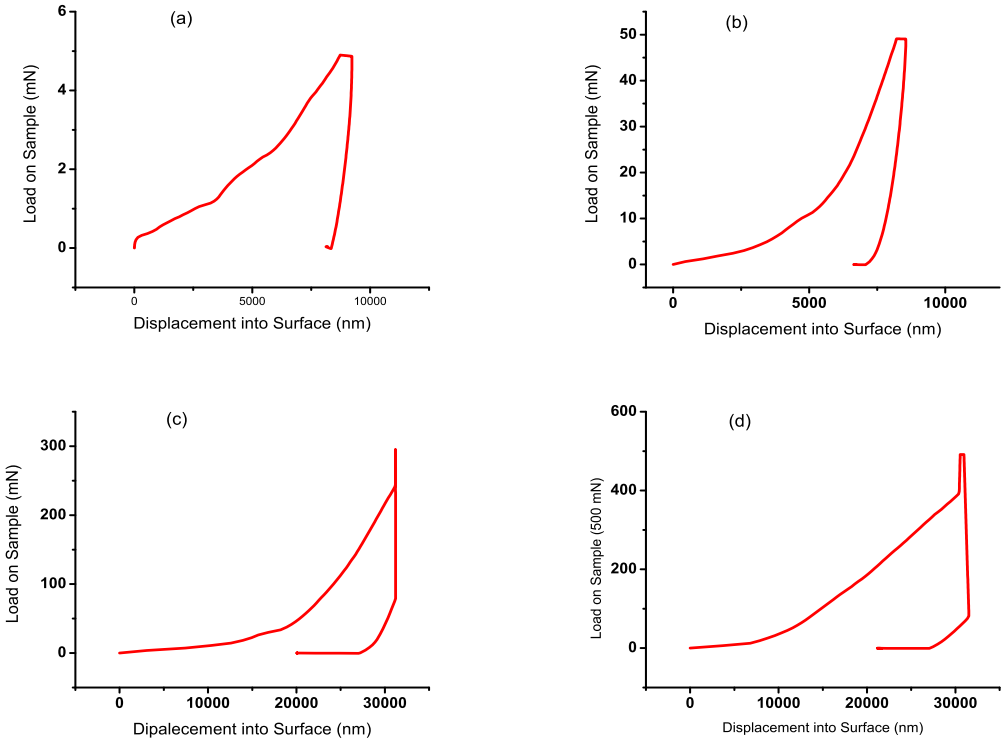

Figure 6.7: Load vs. Displacement curves at various loading conditions (a) 5 mN (b) 50 mN, (c) 300 mN, and (d) 500 mN

of indented location (fig.6.6b). Indentation at point 3 is carried out very close to the edge and the crack marks are clearly visible (fig.6.6c). The cracks thus seen to explain the difference in the two shapes of load-displacement profiles. The maximum load seen in the load-displacement curve is 700 mN.

In the next set of experiments, we conducted indentations by controlling the load. Here the purpose is to see what kind of damages happen to the layers under a specified load. The force measurements of our mechanical exfoliation indicate that the magnitude of the initial wedge material engagement generates forces around 300-500 mN, after which it reduces to a value of around 50 mN. Hence, we performed the indentation at a load of 5, 50, 300 and 500 mN. Figure 6.7 provides the load vs. displacement curves at these loads. Open hysteresis loops are observed at all the loads. It provides evidence of some form of irreversible structural damage on the

surface. Figure 6.7a shows 5 mN indentation load. Indentations were carried out at different locations at 5mN display the same trends of the load vs displacement curves were more similar. However, different loading curves were observed. This may be due to variation on the surface; In chapter 3, we presented the surface condition of the side surface of the HOPG. The indent marks were very difficult to obseve. Figure 6.7b presents data for 50 mN indentation load. It indicate smooth lopen loop loading and unloading curve. The indent marks were barely visible. Gradual increment of the loads to 300 and 500 mN results in a sharp peak at the end of loading before unloading commences. These deviations are entirely different compared with indentation normal to the HOPG surface. The max displacement at the peak load is changes with location with very little difference between 300 & 500 mN.

The surface after indentations indicate that at lower loads we can hardly observe any layer damages. However, at higher load it is possible to obseve them with certain distinctions. Figure 6.8a to f indicate surface damage at selected locations. The respective load vs. displacement curves are shown placements a shown in fig.6.7a-d. We selected these points out of a large number of indents; indented points (fig.6.8a,b) were selected close to the edge. The location at fig.6.8c is in the middle of the sample. Figure 6.8b shows an instance that bunches of layers are detaching form its bulk due to the indenter force. Fig.6.8d and e shows another two different locations under the indenter. Figure 6.8e shows cracks (circled) underneath the indenter. The enlarged image of fig.6.8f clearly indicates crushed layers and pillar types of layers.

The cracked surfaces are also closely observed to see the nature of the cracks and the distortions to the layers. In HOPG, the interactions between layers occur via weak van der Waals forces. Therefore, the indented forces may easily crack through the layers. In fig.6.9, it is noticed that the crack propagates between a bunch of layers

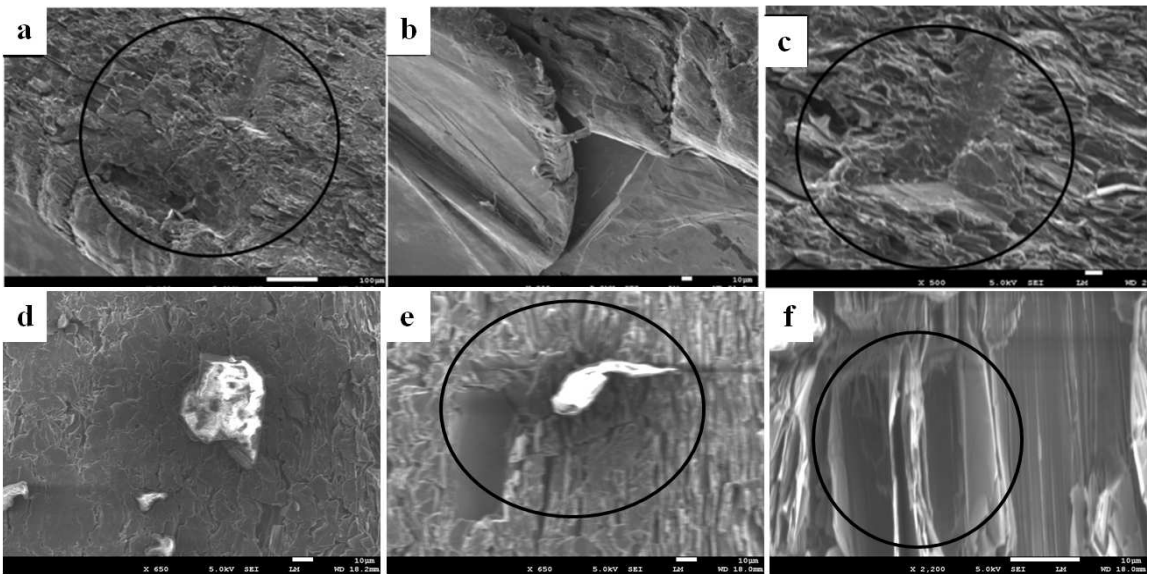

Figure 6.8: Indentation Marks on the surface under load control; (a) Indents close to edge, (b) Torn edge (500 mN), (c) Indented middle location ,(d) Less fractured surface (300 mN),(e) Fractured surface(300 mN), and (f) Crushed and standing distorted layers (500 mN)under the indenter

(fig.6.9a). A relative shearing of the layers is also observed. The thickness of the cracked layers are in the micro-meter range. There are a number of kinks (fig.6.9c and e) that are also observed. A number of voids are also seen between the layers. As reported in the literature kinks are formed due to dislocation movements [150]. These kinks are intact to see them in a bunch. Kinks have been reported in the literature [150,213] during indentation perpendicular to the basal plane. From these observations, it is thus possible for kinks to form by indenting parallel to the basal plane. Kinking is also observed during the WBME process and as reported in earlier chapter 3.

We conducted multiple indentations at the same place and the observed load vs. displacement curve as shown in fig.6.10. This was undertaken at two loads of 200 and 500 mN. Out of a number of indents, we have selected two different locations for discussion. At 200mN, a gradually increasing systematic pattern of the hysteresis loops, were observed as in fig.6.10a. At 500 mN two different types of load vs.

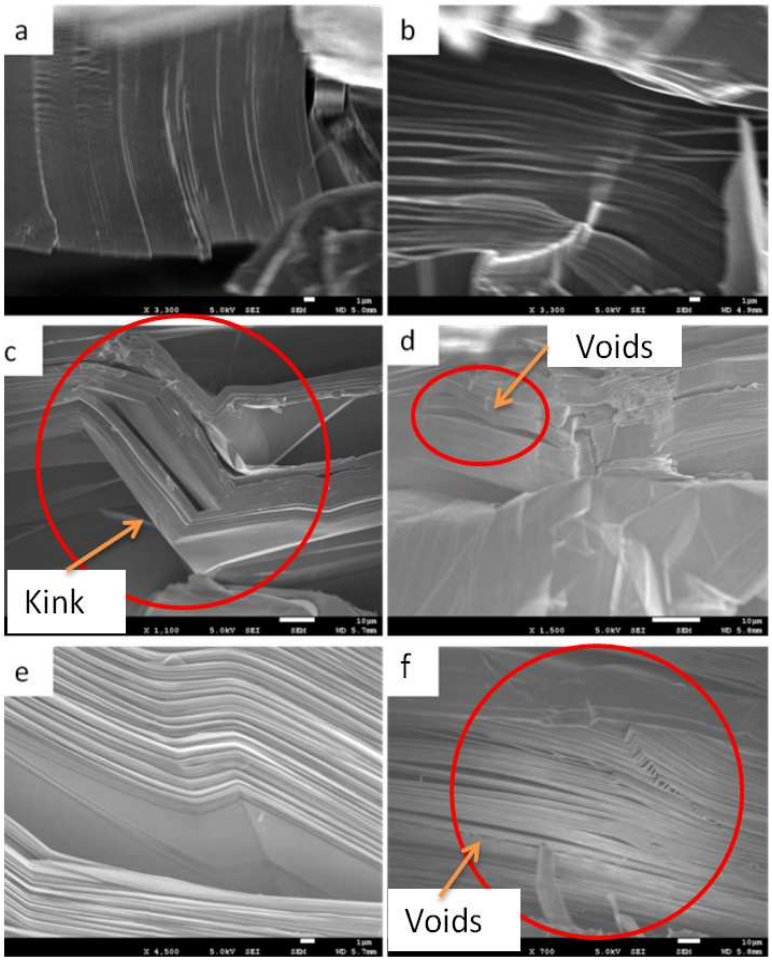

Figure 6.9: Effects of the indentation at high loads (load is 500 mN at locations at point 3-close to edge); (a) Bunch of breaking layers, (b) and (d) Distorted layers, (c) Bunch of kinks, (e) Separated kinks(f) Partially crack propagation

displacement curves are observed as in fig.6.10b. A similar indentation study [150] (normal to the basal plane) reported kink bands and proposed an explanation based on a kinking-based model. Another indentation study [214] with HOPG (normal to basal plane) is reported where fracture morphology was studied.

6.3.1 Raman Observations

We performed Raman spectroscopy analysis at the indented location to understand structural variation, defects etc. The peak positions in the Raman spectra and their

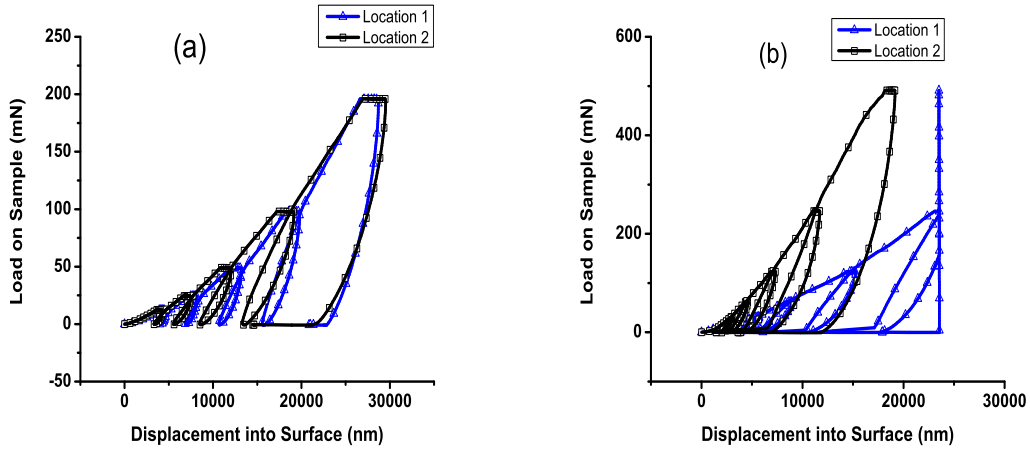

Figure 6.10: Load vs. displacement with multiple (5 times) indents at same location with (a) 200 mN and (b) 500 mN loads

widths indicate vital information. In graphite, several significant peaks are reported at 1360 cm^{-1} and 1580 cm^{-1} that relate to the defects and in-plane vibration respectively [215]. The Raman spectra are shown in fig.6.11. Data is collected on both free and indented surfaces. Two sets of readings were collected at each measurement. Both single indents and multiple (5) times under the load of 500 mN were examined. The full spectrum of data is shown in fig.6.11a. The enlarged sections of 1500-1800 and 2400-2600 are shown in fig.6.11b and c respectively. Compensation for basement deviations is applied to the data. The several key peaks observed are closely analyzed. At 1582 cm^{-1}, a peak is seen at, all three conditions and the multiple indenter location recorded the highest intensity magnitude. Several other peaks are observed close to the earlier peak at the multiple indent location. These shifts are observed at 1660, 1700, 1754 cm^{-1}. Broader, but almost identical peaks are observed at all three conditions at 2690 cm^{-1}. The first question arises as to what cause the several neighboring peaks at the multiple indent location.

The nature of these indentations, parallel to the basal plane, provides a unique perspective into layer interactions and damages seen in graphite, hitherto unreported. As explained earlier indentations are popularly performed perpendicular to the basal

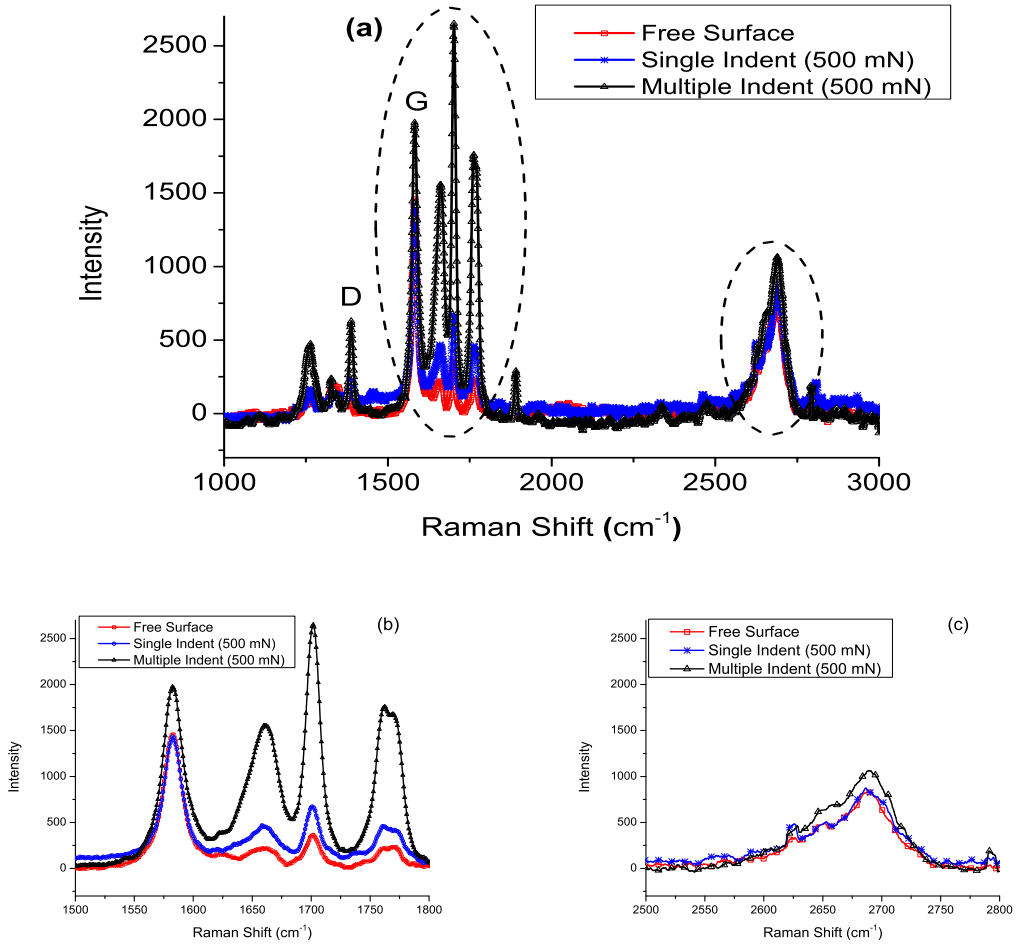

Figure 6.11: Raman peak variation; (a) Full spectrum of data, (b) Enlarge Raman shift spectrum between 1500-1800, and (c) Enlarge Raman shift spectrum between 2400- 2800

plane. From this point of view, this study and results are valuable. We do note that the observations seen in the nature of layer separation and damage could be accentuated due to the nature of the indenter geometry used. Using a thin microtomy type of diamond wedge may show similar damages but to a lesser degree as the wedge proceeds with the indentation. The results shown here have to be cautiously interpreted in order to understand and correlate to our wedge based mechanical exfoliation. This study is still open to address the questions of exactly what structural changes take place during 'pop-in' and 'pop-outs' and how the Raman data correlate

with these structural changes, etc.

6.4 Summary

We performed micro-nano indentation on HOPG parallel to the basal plane by controlling the load and the depth. Two different load-displacements curves were observed. Breaking of layers causes a sharp vertical line in the load-displacement curve during unloading. It is the major source of difference in the load-displacement profiles. 'Pop-in' and 'pop-out' events are observed during both loading and unloading process. Close observation of the cracked surface shows heavy damages to the layers. Heavily crumpled kinks are also observed with large separation gaps. Preliminary Raman microscopic analysis suggests that structural changes have occured.

Chapter 7

CONCLUSION AND FUTURE WORK

This chapter outlining the main conclusions of the thesis and suggests related areas for further exploration.

7.1 Main Conclusions

This thesis study has demonstrated the capability of the wedge-based mechanical exfoliation technique to produce few layers of graphene from the highly ordered pyrolytic graphite. The main observations and conclusions are summarized below.

1. The quality of the exfoliated layers produced:

- The area of the exfoliate layers is much larger than that reported using other mechanical methods such as a scotch tape method.

- The color spectrum obtained from the optical microscope indicates that the

thickness of few layers of graphene varies from a few nanometers to tens of nanometers.

- The measured I_D/I_G ratios of WBME layers are comparable with Cu foil grown CVD and the scotch tape peeled graphene reported in the literature.

- The application of ultrasonic oscillations along the tool edge is seen to significantly reduce the I_D/I_G ratios observed from the Raman spectrum. Hence, the applied oscillations may have the potential to reduce defects in exfoliated layers.

- Detailed microscopic studies at various magnifications using SEM and TEM show the presence of flat, folded, sheared and rolled few layers of graphene. Two types of kink (peak cap and step shape) bands are also observed in the exfoliated layers.

2. Folding, separation and shearing of graphene layers in WBME

- The molecular simulations conducted with LAMMPS show that the separation, folding and shearing of graphene layers can be expected depending on cleaving conditions as seen in the experiments.

- The simulation study with a shaper wedge revealed that the placement of the wedge is critical in controlling the shearing, folding and bending layers. Unfolded layers are found when the selected wedge is placed at less than one third of the inter-layer distance while the separation with folding occurs at wedge placement beyond this limit.

- Shearing of graphene layers is observed during wedge exit as the wedge approaches the end face of the HOPG material. Shearing is seen to be affected both by the speed and depth of insertion.

- The simulation result also shows that the wedge radius or wedge bluntness has a significant effect on layer initiation modes. Exfoliation with a large blunt wedge causes the layers to undergo buckling; larger the radius more the buckling effect. The buckled layer then suddenly unbuckles and releases over the wedge face over the blunt wedge. A critical DOI of 1.6 A^0 is seen necessary for a single layer to be separated; hence with accurate positioning and an atomically flat HOPG surface it is possible to mechanically cleave a single layer. The critical DOI value is seen to be independent of wedge radius. Forces and specific energy calculations also show the strong effect of wedge radius in the process.

3. Scroll formation

- The experimentally observed, rolled structures are identified as carbon nanoscrolls (CNS) and observed in various forms such as sheets with scrolls on two edges, fully rolled up sheets, and stack of sheets rolled together with axial sliding of the roll, creating a conical shape.

- The thorough investigations on the change of rake angle (-17.50 to 50 ^{0}), the wedge radii (2.45, 5.46 A^0 and 11.6 A^0), the wedge position (0-15.6 A^0) and the alignment (0 and 15 ^{0}), and the wedge speed (50, 100 and 500 m/s) during the molecular simulations did not cause any scrolls as we observed in the experiments. Hence, two hypotheses are presented for scroll formation and tested with molecular simulations.

- The first is based on the hypothesis that pre-existing folds in layer edges cause CNS to be formed when the wedge penetrates.

- The second is based on the fact that stressed edges, caused by the defects, can induce scroll formation.

- Molecular dynamic simulations with pre-existing folds show that the initial fold structure and wedge position (cleaving depth) are important parameters in the formation of CNS.

- The force profiles indicate that, compared to initial wedge engagement, a smaller cleaving force required to continue exfoliation and scroll formation. The potential energy profiles indicate that the formation of single scroll is an energy intensive process only in the case of pre-existing scrolled structure.

- With defective edges, the process requires smaller energy to exfoliate and then the defective edged layer spontaneously forms scrolls.

4. Nature of wedge material engagement

- Indentation study is performed on HOPG parallel to the basal plane by controlling the load and the depth to further understand the wedge-material engagement. Two different load-displacements curves were observed. Breaking of layers causes a sharp vertical drop in the load-displacement curve during unloading. It is the major source of difference in the load-displacement profiles. Pop-in and pop-out events are observed during loading and unloading processes. A close observation of the cracked surface showed heavy damages to the layers. Heavily crumpled kinks are also observed with large separation gaps.

- Experimentally measured sectioning forces indicate the presence of a significantly larger spike during initial wedge - material engagement and several other intermittent peaks during wedge penetration. The microscopic analysis of the as-received HOPG (prior to sectioning) showed the presence of discontinuous layers and kink bands even prior to sectioning.

- The force spike seen in experiments is strongly correlated with structural defects such as discontinuous layers and confirmed using molecular simulations. Simulations indicate a similar trend of the required forces to cause cleaving consist of two stages of initial layers and subsequent smaller spike indicating that initial wedge engagement requires a larger force than the continued cleaving of the layers.

- From the experiments, the average cleaving and vertical unified forces of the wedge material interface are calculated as 20 and 2.9 N/mm x10^2 respectively. The extrapolated forces from the simulations that matches with the experimental conditions with a blunt wedge provide the values for the same forces as 1.3 and 0.32 N/mm x10^2 respectively. The value is one order of magnitude difference. The absence of the friction and any material imperfections in the simulation model cases such differences.

- The calculated constant cleaving force (from simulation) converges approximately to 1 eV/A^0 and matches well with calculated theoretical force value of 0.8 eV/A^0 required to break the van der Waals bonds in the cleaved region assuming a constant specific energy

5. Recommendations based on the molecular simulation study are summarized on the factors that affect for the nature of the exfoliation and the scroll formation in table 7.1 and 7.2 respectively.

Table 7.1: Factors affecting the nature of the exfoliation-though molecular simulations

Controlling Factor	Wedge	**Range**	**Type of FLG layers produced**
Wedge Position and Wedge Radius	Sharp	1/3 <DOI <1	Folded layers
	Blunt	0 <DOI <15.6 A^0	Folded layers; minimum DOI of 1.6 A^0 needed to form layer
	Sharp and Blunt	DOI <3 A^0	Significantly larger specific energy
Rake Angle	sharp	-17.5 to 50 ^{0}	Folded and unfoldedlayers but no scroll formation
Mechanical damages prior to exfoliation	Edge defects	Edge defects with / without defects	Scroll formation
	Pre-initial scrolls due to mechanical damage		Scroll formation

This thesis proposed and tested, via experiments and simulations, a novel technique to mechanically exfoliate graphene layers from graphite. The novelty lies in taking a different approach of exfoliating by inserting a wedge from within the layers rather than peeling from outside as in other approaches reported in the literature. This method provides enhanced controllability and repeatability in mechanical exfoliation. The proposed and explored technique of exfoliation is essentially a high-rake

Table 7.2: Effects of various factors on scroll formation

Factor	Range	Results
Rake angle (Degree)	-17.5 <Rake angle <50	No scroll formation
Angled wedge (Degree)	6 <Angle<15	No scroll formation
Wedge Radius(A^0)	Sharper (2.45) Larger (11.60)	No scroll formation No scroll formation
Wedge Position (A^0)	0<DOI<15.6	No scroll formation
Wedge speed (m/s)	50 , 100, 500	No scroll formation

angle machining process. The main scientific contribution of this work lies in exploring the idea of machining or cleaving layered materials using very thin sharp cutting tools. The interaction of the advancing cutting tool with the layers and how this leads to separation, buckling, and folding of layers is of important scientific interest, as a general theory can be developed and extended to other layered material such as mica, MoS2 and others. The scientific contribution of this study is further enhanced via indentation studies of such layers along the layer plane direction. Such studies have not been undertaken before and provide valuable insights into the interaction of the tool with the layers both while in bulk and after separation from the bulk.

7.2 Future Work

The findings from the thesis offer sufficient scope for further study. The following work can be conducted in the future to extend the understanding of wedge-based mechanical exfoliation.

- Temperature assisted exfoliation

  Exfoliation can be assisted with a temperature treatment to the HOPG specimen. High temperature treatment may further weaken inter layer binding and it may hence be possible to cleave with reduced effort and reduce induced damages. Cryo-temperature exfoliation may also be attempted and it can perhaps control the damages that can happen to the cleaved layers.

- Investigations of application of ultra-sonic oscillation

  Preliminary study reveals that application of oscillation to the exfoliation system has a potential of reducing the defects. Application of such oscillations to other materials, is reported in the literature to result in smoothening of

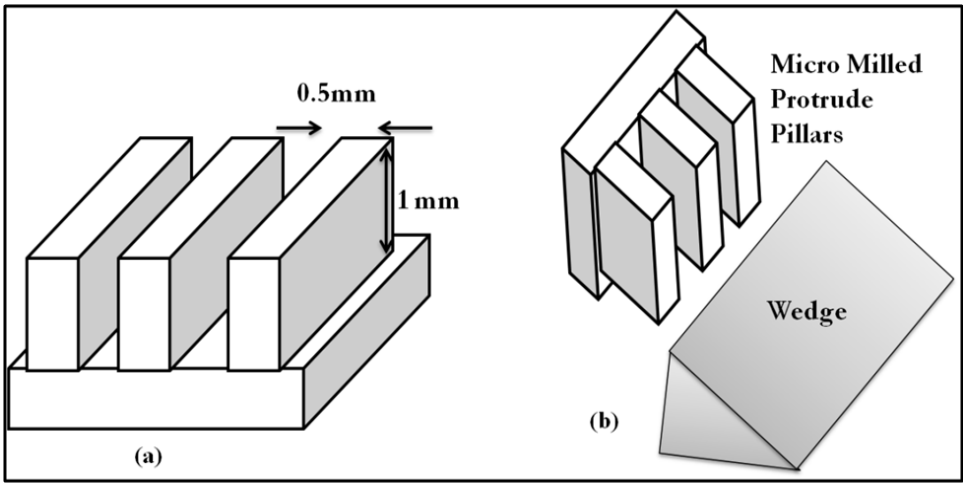

Figure 7.1: Preparation of micro-pillar specimen; (a) expected protrude pillars, (b) Use of micro-pillars in wedge based mechanical exfoliation technique

the separated layers. Therefore, application of oscillation is another possible future direction to be taken to improve the wedge-based exfoliation technique.

- Processing the HOPG specimen

  The HOPG specimen can be patterned before the exfoliation process. It provides opportunity to cleave various sizes of nano-ribbons as indicated in fig.7.1.

- In-situ observation of the cleaving process

  Monitoring the process online provides a better understanding of the process. This may be possible by designing a customized setup and mounting it inside a scanning electron microscope.

- Use of wedge type of indenter

  Indentation process can be carried out with a customized indenter with geometry is very close to the wedge used in the wedge based mechanical exfoliation.

- Extend this exfoliation process to other 2-D materials

  This technique can be extend to separate other layered materials such as mica,

molybdenum disulphide, etc. Such mechanical separation may yield interesting edge structures and material properties.

Author's Publications

Journal Papers

- **B. Jayasena** and S. Subbiah., "A novel mechanical cleavage method for synthesizing few layer graphenes", Nanoscale Res. Lett., vol 6, 95, 2011.

- **B. Jayasena**, C. D. Reddy, and S. Subbiah., "Separation, folding and shearing of graphene layers during wedge-based mechanical exfoliation", Nanotechnology, vol. 24, p. 205301, 2013.

- **B. Jayasena**, S. Subbiah, C. D. Reddy., "Formation of Carbon Nanoscrolls During Wedge-Based Mechanical Exfoliation of HOPG",J. Micro Nano-Manuf., vol 2, 2014

- **B. Jayasena**, and S. Subbiah., "Characteristics of ultra-thin graphitic layers produced by oriented sectioning of highly ordered pyrolytic graphite parallel to the basal plane", (under preparation)

Conference Papers

- **B. Jayasena**, S. Subbiah, C. D. Reddy, "Wedge Radius Effects in Mechanical Exfoliation of HOPG: A Molecular Simulation Study", The International Conference on American Society of Mechanical Engineers (ASME) International Manufacturing Science and Engineering Conference, June 9-13, 2014.
- **B. Jayasena**, S. Subbiah, "Indentation of Highly Oriented Pyrolitic Graphite Parallel to Basal Plane", The International Conference on MicroManufacturing, 25 -28 March 2013, Victoria,Canada.
- **B. Jayasena**, S. Subbiah, C. D. Reddy, " Few Layer Graphene by Wedge Based Mechanical Exfoliation", Material for Tomorrow-UK- Singapore workshop, 6-7 December 2012, Singapore (poster)
- **B. Jayasena**, S. Subbiah, C. D. Reddy, "A mechanical route to carbon nanoscrolls", The International Conference on IEEE Nanotechnology, 20 -23 August 2012, United Kingdom.
- **B. Jayasena**, S. Subbiah, "Ultra thin layers with transverse vibration assisted machining", The International Conference on MicroManufacturing, 7 - 10 March 2011, Tokyo, Japan.
- **B. Jayasena**, S. Subbiah, "A novel mechanical cleavage method for producing few layer graphenes", The International Conference on Recent Advances in Graphene and Related Materials, 1 - 6 August 2010, Singapore.

Summer School Programs

- Selected participant for International Energy Agency Green House Gas (IEAGHG) International Interdisciplinary Carbon Capturing and Storage (CCS) Summer

School, University of Nottingham, United Kingdom, 21st-26th July 2013

- Selected participant for School on Modern Topics in Condensed Matter Physics, 28 Jan-08 Feb 2013, Singapore

Appendix

A sample molecular dynamics code:

The code is written with LAMMPS. The customized metal unit system is used. The atom coordinates are read through the external file. The system temperature is kept fixed at 300K. The AIREBO, potential function is used with appreciate cut off marks.

```
units metal
echo  both
dimension  3
atom-style  atomic
boundary   p  s  s
pair-style hybrid airebo 3.4 1 1 lj/cut 3.4
read-data  SysDef3-D5.0.dat
mass   *  12.0
group  bottom  type  1
group  thermostat  type  2
group  newtonion  type  3
group  wedge  type  4
group mobile  union  thermostat  newtonion
```

pair-coeff * * airebo ./CH.airebo C C C NULL

pair-coeff * 4 lj/cut 0.00284 3.4 3.4

communicate multi

neighbor 2.0 bin

neigh-modify every 100 delay 0 check yes

neigh-modify exclude type 4 4

neigh-modify exclude type 1 4

neigh-modify exclude type 2 4

fix 1 wedge rigid single

fix 2 mobile nve

compute new mobile temp

compute force2 mobile group/group wedge

velocity mobile create 300.0 4928459 dist gaussian units box

fix 3 bottom setforce 0.0 0.0 0.0

fix 5 wedge setforce 0.0 0.0 0.0

fix 6 mobile temp/rescale 1 300 300 0.01 1.0

fix 7 mobile store/force

velocity wedge set -1 0 0 sum yes units box

compute force-1 mobile reduce sum f-7[1] f-7[2] f-7[3]

fix 8 mobile store/state xu yu zu

compute dis mobile displace/atom

thermo 100

thermo-style custom step temp etotal pe press vol f5[1] f5[2] f_5[3]

$thermo - modify\ temp\ new$

$dump$ 1 $all\ custom$ 1000 $SysDef3D5.0.atom\ id\ type\ x\ y\ z$

$dump - modify$ 1 $sort\ id$

$timestep$ 0.001

run50000

Wedge oscillation command

fix 1 wedge move wiggle 0.0 20.0 0.0 25000000.0 units box

variable V equal -5.0

variable x equal vdisplace(0.0,V)

fix 2 *wedge move variable vx* $NULL$ $NULL$ vV $NULL$ $NULL$

Bibliography

[1] M. Terrones, A. R. Botello-Mndez, J. Campos-Delgado, F. Lpez-Uras, Y. I. Vega-Cant, F. J. Rodrguez-Macas, A. L. Elas, E. Muoz-Sandoval, A. G. Cano-Mrquez, J.-C. Charlier, and H. Terrones, "Graphene and graphite nanoribbons: Morphology, properties, synthesis, defects and applications," *Nano Today*, vol. 5, pp. 351–372, 2010.

[2] K. S. Novoselov, A. K. Geim, S. V. Morozov, D. Jiang, Y. Zhang, S. V. Dubonos, I. V. Grigorieva, and A. A. Firsov, "Electric field effect in atomically thin carbon films," *Science*, vol. 306, pp. 666–669, 2004.

[3] A. K. Geim and K. S. Novoselov, "The rise of graphene," *Nat Mater*, vol. 6, pp. 183–191, 2007.

[4] Y. Zhang, Y.-W. Tan, H. L. Stormer, and P. Kim, "Experimental observation of the quantum hall effect and berry's phase in graphene," *Nature*, vol. 438, pp. 201–204, 2005.

[5] K. S. Novoselov, V. I. Falko, L. Colombo, P. R. Gellert, M. G. Schwab, and K. Kim, "A roadmap for graphene," *Nature*, vol. 490, no. 7419, pp. 192–200, 2012.

[6] R. Ruoff, "Graphene: Calling all chemists," *Nat Nano*, vol. 3, pp. 10–11, 2008.

[7] B. Z. Jang and A. Zhamu, "Processing of nanographene platelets (ngps) and ngp nanocomposites: a review," *Journal of Materials Science*, 2008.

[8] S. Stankovich, D. A. Dikin, G. H. B. Dommett, K. M. Kohlhaas, E. J. Zimney, E. A. Stach, R. D. Piner, S. T. Nguyen, and R. S. Ruoff, "Graphene-based composite materials," *Nature*, vol. 442, pp. 282–286, 2006.

[9] Z. Ni, Y. Wang, T. Yu, and Z. Shen, "Raman spectroscopy and imaging of graphene," *Nano Research*, vol. 1, pp. 273–291, 2008.

[10] M. J. Allen, V. C. Tung, and R. B. Kaner, "Honeycomb carbon: A review of graphene," *Chemical Reviews*, vol. 110, pp. 132–145, 2010.

[11] B.-J. Lee, H.-Y. Yu, and G.-H. Jeong, "Controlled synthesis of monolayer graphene toward transparent flexible conductive film application," *Nanoscale Research Letters*, vol. 5, no. 11, pp. 1768–1773, 2010.

[12] S. Park and R. S. Ruoff, "Chemical methods for the production of graphenes," *Nat Nano*, vol. 4, no. 4, pp. 217–224, 2009.

[13] I. Janowska, O. Ersen, T. Jacob, P. Venngues, D. Bgin, M.-J. Ledoux, and C. Pham-Huu, "Catalytic unzipping of carbon nanotubes to few-layer graphene sheets under microwaves irradiation," *Applied Catalysis A: General*, vol. 371, no. 12, pp. 22 – 30, 2009.

[14] Z.-S. Wu, W. Ren, L. Gao, J. Zhao, Z. Chen, B. Liu, D. Tang, B. Yu, C. Jiang, and H.-M. Cheng, "Synthesis of graphene sheets with high electrical conductivity and good thermal stability by hydrogen arc discharge exfoliation," *ACS Nano*, vol. 3, pp. 411–417, 2009.

[15] G. Sun, X. Li, Y. Qu, X. Wang, H. Yan, and Y. Zhang, "Preparation and characterization of graphite nanosheets from detonation technique," *Materials Letters*, vol. 62, pp. 703 – 706, 2008.

[16] M. Jin, H.-K. Jeong, T.-H. Kim, K. P. So, Y. Cui, W. J. Yu, E. J. Ra, and Y. H. Lee, "Synthesis and systematic characterization of functionalized graphene sheets generated by thermal exfoliation at low temperature," *Journal of Physics D: Applied Physics*, vol. 43, p. 275402, 2010.

[17] N.-W. Pu, C.-A. Wang, Y. Sung, Y.-M. Liu, and M.-D. Ger, "Production of few-layer graphene by supercritical co2 exfoliation of graphite," *Materials Letters*, vol. 63, pp. 1987 – 1989, 2009.

[18] K. S. Novoselov, A. K. Geim, S. V. Morozov, D. Jiang, Y. Zhang, S. V. Dubonos, I. V. Grigorieva, and A. A. Firsov, "Electric field effect in atomically thin carbon films," *Science*, vol. 306, pp. 666–669, 2004.

[19] X. Lu, M. Yu, H. Huang, and R. S. Ruoff, "Tailoring graphite with the goal of achieving single sheets," *Nanotechnology*, vol. 10, pp. 269–272, 1999.

[20] Y. B. Zhang, J. P. Small, W. V. Pontius, and P. Kim, "Fabrication and electric-field-dependent transport measurements of mesoscopic graphite devices," *Appl. Phys. Lett.*, vol. 86, pp. 073 104–3, 2005.

[21] S. Gilje, S. Han, M. Wang, K. L. Wang, and R. B. Kaner, "A chemical route to graphene for device applications," *Nano Letters*, vol. 7, pp. 3394–3398, 2007.

[22] P. Blake, P. D. Brimicombe, R. R. Nair, T. J. Booth, D. Jiang, F. Schedin, L. A. Ponomarenko, S. V. Morozov, H. F. Gleeson, E. W. Hill, A. K. Geim, and K. S. Novoselov, "Graphene-based liquid crystal device," *Nano Letters*, vol. 8, pp. 1704–1708, 2008.

[23] D. Li, M. B. Muller, S. Gilje, R. B. Kaner, and G. G. Wallace, "Processable aqueous dispersions of graphene nanosheets," *Nat Nano*, vol. 3, pp. 101–105, 2008.

[24] Studer and Gnaegi, "Minimal compression of ultrathin sections with use of an oscillating diamond knife," *Journal of Microscopy*, vol. 197, pp. 94–100, 2000.

[25] Q. Xu, J. Bao, R. M. Rioux, R. Perez-Castillejos, F. Capasso, and G. M. Whitesides, "Fabrication of large-area patterned nanostructures for optical applications by nanoskiving," *Nano Lett.*, vol. 7, no. 9, pp. 2800–2805, 2007.

[26] J. C. Slonczewski and P. R. Weiss, "Band structure of graphite," *Physical Review*, vol. 109, no. 2, pp. 272–279, 1958, pR.

[27] G. H. Kinchin, "The electrical properties of graphite," *P. Roy. Soc. Lond. A. Mat.*, vol. 217, pp. 9–26, 1953, 10.1098/rspa.1953.0043.

[28] T. Noda, "Graphitization of carbon under high pressure," *Carbon*, vol. 6, pp. 125–133, 1968.

[29] R. E. Franklin, "On the structure of carbon," *J. Chim. Phys. Phys.- Chim. Biol.*, vol. 47, pp. 573–575, 1950, times Cited: 17 Franklin, re.

[30] R. Franklin, "Crystallite growth in graphitizing and non-graphitizing carbons," *Proceedings of the Royal Society of London. Series A. Mathematical and Physical Sciences*, vol. 209, pp. 196–218, 1951.

[31] H. M. J. Griffiths, "High resolution electron microscopy study of graphitization of graphitizable carbons,," in *Conference*, 1982.

[32] J. Hass, W. A. de Heer, and E. H. Conrad, "The growth and morphology of epitaxial multilayer graphene," *Journal of Physics: Condensed Matter*, vol. 20, p. 323202, 2008.

[33] C. Oshima and A. Nagashima, "Ultra-thin epitaxial films of graphite and hexagonal boron nitride on solid surfaces," *Journal of Physics: Condensed Matter*, vol. 9, p. 1, 1997.

[34] X. Sciences, "About xgnp graphene nanoplatelets," 2013.

[35] G. Chen, D. Wu, W. Weng, and C. Wu, "Exfoliation of graphite flake and its nanocomposites," *Carbon*, vol. 41, pp. 619–621, 2003.

[36] P. W. Sutter, P. M. Albrecht, and E. A. Sutter, "Graphene growth on epitaxial ru thin films on sapphire," *Applied Physics Letters*, vol. 97, pp. 213 101–3, 2010.

[37] J.-H. Gao, K. Sagisaka, M. Kitahara, M.-S. Xu, S. Miyamoto, and D. Fujita, "Graphene growth on a pt(111) substrate by surface segregation and precipitation," *Nanotechnology*, vol. 23, p. 055704, 2012.

[38] S. Nie, A. L. Walter, N. C. Bartelt, E. Starodub, A. Bostwick, E. Rotenberg, and K. F. McCarty, "Growth from below: Graphene bilayers on ir(111)," *ACS Nano*, vol. 5, pp. 2298–2306, 2011.

[39] C. Berger, Z. Song, T. Li, X. Li, A. Y. Ogbazghi, R. Feng, Z. Dai, A. N. Marchenkov, E. H. Conrad, P. N. First, and W. A. de Heer, "Ultrathin epitaxial graphite: 2d electron gas properties and a route toward graphene-based nanoelectronics," *The Journal of Physical Chemistry B*, vol. 108, pp. 19 912–19 916, 2004.

[40] W. A. de Heer, C. Berger, X. Wu, P. N. First, E. H. Conrad, X. Li, T. Li, M. Sprinkle, J. Hass, M. L. Sadowski, M. Potemski, and G. Martinez, "Epitaxial graphene," *Solid State Communications*, vol. 143, pp. 92 – 100, 2007.

[41] H. Zhang and P. X. Feng, "Fabrication and characterization of few-layer graphene," *Carbon*, vol. 48, pp. 359–364, 2010.

[42] M. Terrones, "Materials science: Nanotubes unzipped," *Nature*, vol. 458, pp. 845–846, 2009.

[43] L. Jiao, L. Zhang, X. Wang, G. Diankov, and H. Dai, "Narrow graphene nanoribbons from carbon nanotubes," *Nature*, vol. 458, pp. 877–880, 2009.

[44] D. V. Kosynkin, A. L. Higginbotham, A. Sinitskii, J. R. Lomeda, A. Dimiev, B. K. Price, and J. M. Tour, "Longitudinal unzipping of carbon nanotubes to form graphene nanoribbons," *Nature*, vol. 458, pp. 872–876, 2009.

[45] A. G. Cano-Marquez, F. J. Rodrguez-Macias, J. Campos-Delgado, C. G. Espinosa-Gonzalez, F. Tristan-Lopez, D. Ramrez-Gonzaez, D. A. Cullen, D. J. Smith, M. Terrones, and Y. I. Vega-Cantu, "Ex-mwnts: Graphene sheets and ribbons produced by lithium intercalation and exfoliation of carbon nanotubes," *Nano Letters*, vol. 9, pp. 1527–1533, 2009.

[46] Z.-S. Wu, W. Ren, L. Gao, J. Zhao, Z. Chen, B. Liu, D. Tang, B. Yu, C. Jiang, and H.-M. Cheng, "Synthesis of graphene sheets with high electrical conductivity and good thermal stability by hydrogen arc discharge exfoliation," *ACS Nano*, vol. 3, pp. 411–417, 2009.

[47] C. Wu, G. Dong, and L. Guan, "Production of graphene sheets by a simple helium arc-discharge," *Physica E: Low-dimensional Systems and Nanostructures*, vol. 42, pp. 1267 – 1271, 2010.

[48] D. R. Dreyer, S. Park, C. W. Bielawski, and R. S. Ruoff, "The chemistry of graphene oxide," *Chem. Soc. Rev.*, vol. 39, pp. 228–240, 2010.

[49] X. Wang, S. M. Tabakman, and H. Dai, "Atomic layer deposition of metal oxides on pristine and functionalized graphene," *Journal of the American Chemical Society*, vol. 130, no. 26, pp. 8152–8153, 2008.

[50] L. Wang, J. J. Travis, A. S. Cavanagh, X. Liu, S. P. Koenig, P. Y. Huang, S. M. George, and J. S. Bunch, "Ultrathin oxide films by atomic layer deposition on graphene," *Nano Letters*, vol. 12, pp. 3706–3710, 2012.

[51] L. Ci, Z. Xu, L. Wang, W. Gao, F. Ding, K. Kelly, B. Yakobson, and P. Ajayan, "Controlled nanocutting of graphene," *Nano Research*, vol. 1, no. 2, pp. 116–122, 2008.

[52] L. Ci, L. Song, D. Jariwala, A. L. Elas, W. Gao, M. Terrones, and P. M. Ajayan, "Graphene shape control by multistage cutting and transfer," *Advanced Materials*, vol. 21, pp. 4487–4491, 2009.

[53] S. Park, J. An, I. Jung, R. D. Piner, S. J. An, X. Li, A. Velamakanni, and R. S. Ruoff, "Colloidal suspensions of highly reduced graphene oxide in a wide variety of organic solvents," *Nano Letters*, vol. 9, no. 4, pp. 1593–1597, 2009, pMID: 19265429.

[54] P. K. Ang, S. Wang, Q. Bao, J. T. L. Thong, and K. P. Loh, "High-throughput synthesis of graphene by intercalationexfoliation of graphite oxide and study of ionic screening in graphene transistor," *ACS Nano*, vol. 3, pp. 3587–3594, 2009.

[55] D. A. Dikin, S. Stankovich, E. J. Zimney, R. D. Piner, G. H. B. Dommett, G. Evmenenko, S. T. Nguyen, and R. S. Ruoff, "Preparation and characterization of graphene oxide paper," *Nature*, vol. 448, pp. 457–460, 2007.

[56] L. M. Viculis, J. J. Mack, and R. B. Kaner, "A chemical route to carbon nanoscrolls," *Science*, vol. 299, pp. 1361–1361, 2003, 649DU Times Cited:159 Cited References Count:6.

[57] M. Dresselhaus and G. Dresselhaus, "Intercalation compounds of graphite," *Advances in Physics*, vol. 30, pp. 139–326, 1981.

[58] M. S. Dresselhaus and G. Dresselhaus, "Intercalation compounds of graphite," *Advances in Physics*, vol. 51, pp. 1–186, 2002.

[59] D. Zhan, L. Sun, Z. H. Ni, L. Liu, X. F. Fan, Y. Wang, T. Yu, Y. M. Lam, W. Huang, and Z. X. Shen, "Fecl3-based few-layer graphene intercalation compounds: Single linear dispersion electronic band structure and strong charge transfer doping," *Advanced Functional Materials*, vol. 20, no. 20, pp. 3504–3509, 2010.

[60] M. J. McAllister, J.-L. Li, D. H. Adamson, H. C. Schniepp, A. A. Abdala, J. Liu, M. Herrera-Alonso, D. L. Milius, R. Car, R. K. Prud'homme, and I. A. Aksay, "Single sheet functionalized graphene by oxidation and thermal expansion of graphite," *Chemistry of Materials*, vol. 19, pp. 4396–4404, 2007.

[61] A. Al-Amoudi, D. Studer, and J. Dubochet, "Cutting artefacts and cutting process in vitreous sections for cryo-electron microscopy," *Journal of Structural Biology*, vol. 150, pp. 109 – 121, 2005.

[62] R. Phillips, "Diamond knife ultra microtomy of metals and the structure of microtomed sections," *British Journal of Applied Physics*, vol. 12, p. 554, 1961.

[63] K. Richter, "Cutting artefacts on ultrathin cryosections of biological bulk specimens," *Micron*, vol. 25, pp. 297 – 308, 1994.

[64] J. W. Obreimoff, "The splitting strength of mica," *Proceedings of the Royal Society of London. Series A, Containing Papers of a Mathematical and Physical Character*, vol. 127, pp. pp. 290–297, 1930.

[65] H. Fernandez-Moran, "Applications of a diamond knife for ultrathin sectioning to the study of the fine structure of biological tissues and metals," *Biohysical and Biochemical Cytology*, vol. 2, no. 4, pp. 29–30, 1956.

[66] I. M. Dawson and E. A. C. Follett, "An electron microscope study of synthetic graphite," *Proceedings of the Royal Society of London. Series A, Mathematical and Physical Sciences*, vol. 253, pp. pp. 390–402, 1959.

[67] D. Clinton and G. Kaye, "Characterization of bonded carbons by ultra-thin sectioning," *Carbon*, vol. 2, no. 4, pp. 341–348, 1965.

[68] F. J. M. Rietmeijer, "Mixed layering in disordered sri lanka graphite," *Carbon*, vol. 29, pp. 669–675, 1991.

[69] K. Wen, J. Marrow, and B. Marsden, "Microcracks in nuclear graphite and highly oriented pyrolytic graphite (hopg)," *J. Nucl. Mater.*, vol. 381, pp. 199–203, 2008.

[70] Y. D. Yan, T. Sun, Y. C. Liang, and S. Dong, "Effects of scratching directions on afm-based abrasive abrasion process," *Tribol. Int.*, vol. 42, pp. 66–70, 2009.

[71] N. Ikawa, S. Shimada, H. Tanaka, and G. Ohmori, "An atomistic analysis of nanometric chip removal as affected by tool-work interaction in diamond turning," *CIRP Annals - Manufacturing Technology*, vol. 40, pp. 551–554, 1991.

[72] S. Shimada and N. Ikawa, "Molecular dynamics analysis as compared with experimental results of micromachining," *CIRP Ann.-Manuf. Techn.*, vol. 41, pp. 117–120, 1992.

[73] M. J. Jackson, *Micro and Nanomanufacturing*. Springer US, 2007, pp. 591–634.

[74] M. M. Ernst H, "Chip formation, friction and high quality machined surfaces, surface treatment of metals," *Am. Soc. Met.*, vol. 29, p. 229, 1941.

[75] S. Subbiah, "Some investigations of scaling effects in micro-cutting," Ph.D. dissertation, G. W. Woodruff School of Mechanical Engineering Georgia Institute of Technology, 2006.

[76] E. Merchant, "Mechanics of the metal cutting process. i. orthogonal cutting and a type 2 chip," *Journal of Applied Physics*, vol. 16, pp. 267–275, 1945.

[77] M. E. Merchant, "Mechanics of the metal cutting process. i. orthogonal cutting and a type 2 chip," *Journal of Applied Physics*, vol. 16, pp. 267–275, 1945.

[78] S. Subbiah and S. N. Melkote, "The constant force component due to material separation and its contribution to the size effect in specific cutting energy," *Journal of Manufacturing Science and Engineering*, vol. 128, pp. 811–815, 2006.

[79] R. Komanduri, N. Chandrasekaran, and L. M. Raff, "Effect of tool geometry in nanometric cutting: a molecular dynamics simulation approach," *Wear*, vol. 219, pp. 84–97, 1998.

[80] D. E. Brehl and T. A. Dow, "Review of vibration-assisted machining," *Precision Engineering*, vol. 32, pp. 153–172, 2008.

[81] A. S. Adnan and S. Subbiah, "Experimental investigation of transverse vibration-assisted orthogonal cutting of al-2024," *International Journal of Machine Tools and Manufacture*, vol. 50, pp. 294–302, 2010.

[82] E. Martelloti and H. Ernst, *Physics of Metal Cutting*, ser. Technical Papers. American Gear Manufacturers Association, 1942.

[83] J. Rotberg, A. Ber, and R. Wertheim, "Chip control in cut-off tools," {*CIRP*} *Annals - Manufacturing Technology*, vol. 40, no. 1, pp. 73 – 77, 1991.

[84] M. Shaw, *Metal Cutting Principles 2E C*, ser. Oxford Series on Advanced Manufacturing. Oxford University Press, Incorporated, 2005.

[85] R. Komanduri, S. Varghese, and N. Chandrasekaran, "On the mechanism of material removal at the nanoscale by cutting," *Wear*, vol. 269, pp. 224 – 228, 2010.

[86] A. G. Atkins, "Toughness and cutting: a new way of simultaneously determining ductile fracture toughness and strength," *Engineering Fracture Mechanics*, vol. 72, pp. 849–860, 2005.

[87] T. Atkins, *The Science and Engineering of Cutting: The Mechanics and Processes of Separating and Puncturing Biomaterials, Metals and Non-metals*. Elsevier Science, 2009.

[88] J. G. Williams, "Friction and plasticity effects in wedge splitting and cutting fracture tests," *Journal of Materials Science*, vol. 33, no. 22, pp. 5351–5357, 1998.

[89] Y. Patel, B. R. K. Blackman, and J. G. Williams, "Determining fracture toughness from cutting tests on polymers," *Engineering Fracture Mechanics*, vol. 76, pp. 2711–2730, 2009.

[90] D. Wyeth and A. Atkins, "Mixed mode fracture toughness as a separation parameter when cutting polymers," *Engineering Fracture Mechanics*, vol. 76, pp. 2690 – 2697, 2009.

[91] M. J. Blumer, P. Gahleitner, T. Narzt, C. Handl, and B. Ruthensteiner, "Ribbons of semithin sections: an advanced method with a new type of diamond knife," *Journal of Neuroscience Methods*, vol. 120, pp. 11 – 16, 2002.

[92] D. Mayerich, L. Abbott, and B. Mccormick, "Knife-edge scanning microscopy for imaging and reconstruction of three-dimensional anatomical structures of the mouse brain," *Journal of Microscopy*, vol. 231, pp. 134–143, 2008.

[93] M. L. Ericson and H. Lindberg, "Design and potential of instrumented ultramicrotomy," *Polymer*, vol. 38, pp. 4485 – 4489, 1997.

[94] D. J. Lipomi, M. A. Kats, P. Kim, S. H. Kang, J. Aizenberg, F. Capasso, and G. M. Whitesides, "Fabrication and replication of arrays of single- or multicomponent nanostructures by replica molding and mechanical sectioning," *ACS Nano*, vol. 4, pp. 4017–4026, 2010.

[95] D. J. Lipomi, R. V. Martinez, R. M. Rioux, L. Cademartiri, W. F. Reus, and G. M. Whitesides, "Survey of materials for nanoskiving and influence of the cutting process on the nanostructures produced," *ACS Applied Materials & Interfaces*, vol. 2, pp. 2503–2514, 2010.

[96] D. J. Lipomi, R. V. Martinez, and G. M. Whitesides, "Use of thin sectioning (nanoskiving) to fabricate nanostructures for electronic and optical applications," *Angewandte Chemie International Edition*, vol. 50, pp. 8566–8583, 2011.

[97] H. Gnaegi, D. Studer, E. Bos, P. Peters, and J. Pierson, "Ultramicrotomy in biology and materials science: an overview," in *EMC 2008 14th European Microscopy Congress 15 September 2008, Aachen, Germany*, M. Luysberg, K. Tillmann, and T. Weirich, Eds. Springer Berlin Heidelberg, 2008, pp. 797–798.

[98] M. Ericson and H. Lindberg, "A method of measuring energy dissipation during crack propagation in polymers with an instrumented ultramicrotome," *Journal of Materials Science*, vol. 31, pp. 655–662, 1996.

[99] J. C. Meyer, A. K. Geim, M. I. Katsnelson, K. S. Novoselov, T. J. Booth, and S. Roth, "The structure of suspended graphene sheets," *Nature*, vol. 446, pp. 60–63, Mar. 2007.

[100] W. Regan, N. Alem, B. Aleman, B. Geng, C. Girit, L. Maserati, F. Wang, M. Crommie, and A. Zettl, "A direct transfer of layer-area graphene," *Applied Physics Letters*, vol. 96, pp. 113 102–113 105, 2010.

[101] A. Reina, H. Son, L. Jiao, B. Fan, M. S. Dresselhaus, Z. Liu, and J. Kong, "Transferring and identification of single- and few-layer graphene on arbitrary substrates," *The Journal of Physical Chemistry C*, vol. 112, pp. 17 741–17 744, 2008.

[102] M. J. Allen, V. C. Tung, L. Gomez, Z. Xu, L.-M. Chen, K. S. Nelson, C. Zhou, R. B. Kaner, and Y. Yang, "Soft transfer printing of chemically converted graphene," *Advanced Materials*, vol. 21, no. 20, pp. 2098–2102, 2009.

[103] S. Bae, H. Kim, Y. Lee, X. Xu, J.-S. Park, Y. Zheng, J. Balakrishnan, T. Lei, H. Ri Kim, Y. I. Song, Y.-J. Kim, K. S. Kim, B. Ozyilmaz, J.-H. Ahn, B. H. Hong, and S. Iijima, "Roll-to-roll production of 30-inch graphene films for transparent electrodes," *Nat Nano*, vol. 5, pp. 574–578, 2010.

[104] X. Liang, V. Giacometti, A. Ismach, B. D. Harteneck, D. L. Olynick, and S. Cabrini, "Roller-style electrostatic printing of prepatterned few-layer-graphenes," *Applied Physics Letters*, vol. 96, p. 013109, 2010.

[105] M. V. Stoitsov and I. Z. Petkov, "Density functional theory at finite temperatures," *Annals of Physics*, vol. 184, pp. 121 – 147, 1988.

[106] T. Hickel, B. Grabowski, F. Krmann, and J. Neugebauer, "Advancing density functional theory to finite temperatures: methods and applications in steel design," *Journal of Physics: Condensed Matter*, vol. 24, p. 053202, 2012.

[107] S. Zhang, W. K. Liu, and R. S. Ruoff, "Atomistic simulations of double-walled carbon nanotubes (dwcnts) as rotational bearings," *Nano Letters*, vol. 4, no. 2, pp. 293–297, 2004.

[108] N. V. Prodanov and A. V. Khomenko, "Computational investigation of the temperature influence on the cleavage of a graphite surface," *Surface Science*, vol. 604, no. 78, pp. 730–740, 2010.

[109] S. Plimpton, "Fast parallel algorithms for short-range molecular dynamics," *Journal of Computational Physics*, vol. 117, no. 1, pp. 1–19, 1995.

[110] H. Zhao, K. Min, and N. R. Aluru, "Size and chirality dependent elastic properties of graphene nanoribbons under uniaxial tension," *Nano Letters*, vol. 9, pp. 3012–3015, 2009, pMID: 19719113.

[111] A. P. Awasthi, D. C. Lagoudas, and D. C. Hammerand, "Modeling of graphene-polymer interfacial mechanical behavior using molecular dynamics," *Modelling and Simulation in Materials Science and Engineering*, vol. 17, p. 015002, 2009.

[112] I. Shabib and R. E. Miller, "Deformation characteristics and stressstrain response of nanotwinned copper via molecular dynamics simulation," *Acta Materialia*, vol. 57, pp. 4364 – 4373, 2009.

[113] G. W. Slater, C. Holm, M. V. Chubynsky, H. W. de Haan, A. Dub, K. Grass, O. A. Hickey, C. Kingsburry, D. Sean, T. N. Shendruk, and L. Zhan, "Modeling the separation of macromolecules: A review of current computer simulation methods," *Electrophoresis*, vol. 30, pp. 792–818, 2009.

[114] X. Zhang, A. S. Kumar, M. Rahman, and K. Liu, "Modeling of the effect of tool edge radius on surface generation in elliptical vibration cutting," *The International Journal of Advanced Manufacturing Technology*, vol. 65, pp. 35–42, 2013.

[115] Z. Deng, A. Smolyanitsky, Q. Li, X.-Q. Feng, and R. J. Cannara, "Adhesion-dependent negative friction coefficient on chemically modified graphite at the nanoscale," *Nat Mater*, vol. 11, pp. 1032–1037, Dec. 2012.

[116] Q. Pei, C. Lu, and H. Lee, "Large scale molecular dynamics study of nanometric machining of copper," *Comp Mater Sci*, vol. 41, pp. 177 – 185, 2007.

[117] J. J. Zhang, T. Sun, Y. D. Yan, Y. C. Liang, and S. Dong, "Molecular dynamics simulation of subsurface deformed layers in afm-based nanometric cutting process," *Applied Surface Science*, vol. 254, pp. 4774–4779, 2008.

[118] R. Narulkar, S. Bukkapatnam, L. M. Raff, and R. Komanduri, "Graphitization as a precursor to wear of diamond in machining pure iron: A molecular dynamics investigation," *Computational Materials Science*, vol. 45, pp. 358–366, 2009.

[119] S. Goel, X. Luo, and R. L. Reuben, "Molecular dynamics simulation model for the quantitative assessment of tool wear during single point diamond turning of cubic silicon carbide," *Comp. Mater. Sci.*, vol. 51, pp. 402–408, 2012.

[120] T.-H. Fang and C.-I. Weng, "Three-dimensional molecular dynamics simulation of nanostructure for reciprocating nanomachining process," *J. Vac. Sci. Technol. B*, vol. 27, p. 1536, 2009.

[121] S. Shimada, N. Ikawa, H. Tanaka, G. Ohmori, and J. Uchikoshi, "Feasibility study on ultimate accuracy in microcutting using molecular dynamics simulation," *Ann CIRP*, vol. 42, pp. 117 – 120, 1993.

[122] Z.-C. Lin and J.-C. Huang, "A nano-orthogonal cutting model based on a modified molecular dynamics technique," *Nanotechnology*, vol. 15, p. 510, 2004.

[123] P. Zhu, Y. Hu, T. Ma, and H. Wang, "Study of afm-based nanometric cutting process using molecular dynamics," *Appl Surf Sci*, vol. 256, pp. 7160 – 7165, 2010.

[124] N. Sasaki, H. Okamoto, S. Masuda, K. Miura, and N. Itamura, "Simulated nanoscale peeling process of monolayer graphene sheet: effect of edge structure and lifting position," *J. Nanomaterials*, vol. 2010, pp. 10:1–10:4, 2010.

[125] V. B. Shenoy, C. D. Reddy, and Y.-W. Zhang, "Spontaneous curling of graphene sheets with reconstructed edges," *ACS Nano*, vol. 4, no. 8, pp. 4840–4844, 2010.

[126] A. Smolyanitsky, J. P. Killgore, and V. K. Tewary, "Effect of elastic deformation on frictional properties of few-layer graphene," *Phys. Rev. B*, vol. 85, p. 035412, 2012.

[127] A. Omeltchenko, J. Yu, R. K. Kalia, and P. Vashishta, "Crack front propagation and fracture in a graphite sheet: A molecular-dynamics study on parallel computers," *Physi. Rev. Lett.*, vol. 78, pp. 2148–2151, 1997.

[128] V. B. Shenoy, C. D. Reddy, A. Ramasubramaniam, and Y. W. Zhang, "Edge-stress-induced warping of graphene sheets and nanoribbons," *Phys. Rev. Lett.*, vol. 101, p. 245501, 2008.

[129] M. Jafary-Zadeh, C. D. Reddy, and Y.-W. Zhang, "A chemical route to control molecular mobility on graphene," *Phys. Chem. Chem. Phys.*, vol. 14, pp. 10 533–10 539, 2012.

[130] I. Structure Probe, "Highly ordered pyrolytic graphite," 2009.

[131] E. M. Sciences, "Electron microscopy sciences," 2010.

[132] J. Kuo, *Electron Microscopy Methods and Protocols*, 2nd ed. Humana Press, 2007.

[133] T. Jawhari, A. Roid, and J. Casado, "Raman spectroscopic characterization of some commercially available carbon black materials," *Carbon*, vol. 33, pp. 1561 – 1565, 1995.

[134] F. Tuinstra and J. L. Koenig, "Raman spectrum of graphite," *The Journal of Chemical Physics*, vol. 53, pp. 1126–1130, 1970.

[135] F. Tuinstra and J. Koenig, "Characterization of graphite fiber surfaces with raman spectroscopy," *Journal of Composite Materials*, vol. 4, no. 4, pp. 492–499, 1970.

[136] A. C. Ferrari and J. Robertson, "Interpretation of raman spectra of disordered and amorphous carbon," *Physical Review B*, vol. 61, p. 14095, 2000.

[137] L. G. Cancado, K. Takai, T. Enoki, M. Endo, Y. A. Kim, H. Mizusaki, A. Jorio, L. N. Coelho, R. Magalhaes-Paniago, and M. A. Pimenta, "General equation for the determination of the crystallite size la of nanographite by raman spectroscopy," *Applied Physics Letters*, vol. 88, no. 16, pp. 163 106–3, 2006.

[138] L. C. Nistor, J. Landuyt, V. G. Ralchenko, T. V. Kononenko, E. D. Obraztsova, and V. E. Strelnitsky, "Direct observation of laser-induced crystallization of a-c:h films," *Applied Physics A: Materials Science & Processing*, vol. 58, pp. 137–144, 1994.

[139] O. Beyssac, Goff, B., C. Chopin, and J. N. Rouzaud, "Raman spectra of carbonaceous material in metasediments: a new geothermometer," *Journal of Metamorphic Geology*, pp. 859–871, 2002.

[140] J. D. Wood, S. W. Schmucker, A. S. Lyons, E. Pop, and J. W. Lyding, "Effects of polycrystalline cu substrate on graphene growth by chemical vapor deposition," *Nano Letters*, vol. 11, pp. 4547–4554, 2011.

[141] P. Zhao, A. Kumamoto, S. Kim, X. Chen, B. Hou, S. Chiashi, E. Einarsson, Y. Ikuhara, and S. Maruyama, "Self-limiting chemical vapor deposition growth of monolayer graphene from ethanol," *The Journal of Physical Chemistry C*, vol. 117, no. 20, pp. 10 755–10 763, 2013. [Online]. Available: http://pubs.acs.org/doi/abs/10.1021/jp400996s

[142] A. Ismach, C. Druzgalski, S. Penwell, A. Schwartzberg, M. Zheng, A. Javey, J. Bokor, and Y. Zhang, "Direct chemical vapor deposition of graphene on dielectric surfaces," *Nano Letters*, vol. 10, no. 5, pp. 1542–1548, 2010. [Online]. Available: http://pubs.acs.org/doi/abs/10.1021/nl9037714

[143] Z. H. Ni, H. M. Wang, Y. Ma, J. Kasim, Y. H. Wu, and Z. X. Shen, "Tunable stress and controlled thickness modification in graphene by annealing," *ACS Nano*, vol. 2, pp. 1033–1039, 2008.

[144] H. Chang and A. J. Bard, "Observation and characterization by scanning tunneling microscopy of structures generated by cleaving highly oriented pyrolytic graphite," *Langmuir*, vol. 7, pp. 1143–1153, 1991.

[145] S. Roddaro, P. Pingue, V. Piazza, V. Pellegrini, and F. Beltram, "The optical visibility of graphene: Interference colors of ultrathin graphite on sio_2," *Nano Lett.*, vol. 7, pp. 2707–2710, 2007.

[146] A. Reina, X. Jia, J. Ho, D. Nezich, H. Son, V. Bulovic, M. S. Dresselhaus, and J. Kong, "Large area, few-layer graphene films on arbitrary substrates by chemical vapor deposition," *Nano Letters*, vol. 9, pp. 30–35, 2009.

[147] C. Soldano, A. Mahmood, and E. Dujardin, "Production, properties and potential of graphene," *Carbon*, vol. 48, pp. 2127 – 2150, 2010.

[148] C. Roscoe and J. M. Thomas, "The identification and some physico-chemical consequences of non-basal edge and screw dislocations in graphite," *P. Roy. Soc. Lond. A. Mat.*, vol. 297, pp. 397–407, 1967.

[149] Z. Liu, Q.-s. Zheng, and J. Z. Liu, "Stripe/kink microstructures formed in mechanical peeling of highly orientated pyrolytic graphite," *Appl. Phys. Lett.*, vol. 96, pp. 201 909–201 912, 2010.

[150] M. W. Barsoum, A. Murugaiah, S. R. Kalidindi, T. Zhen, and Y. Gogotsi, "Kink bands, nonlinear elasticity andnanoindentations in graphite," *Carbon*, vol. 42, pp. 1435–1445, 2004.

[151] M. W. Barsoum, L. Farber, and T. El-Raghy, "Dislocations, kink bands, and room-temperature plasticity of ti3sic2," *Metall. Mater. Trans. A*, vol. 30, pp. 1727–1738, 1999.

[152] F. C. Frank and A. N. Stroh, "On the theory of kinking," *Proc. Phys. Soc. London, Sect. B*, vol. 65, pp. 811–821, 1952.

[153] Z. Sun, Z. Zhang, H. Hashimoto, and T. Abe, "Ternary compound ti3sic2: Part ii. deformation and fracture behavior at different temperatures," *Mater. Trans., JIM*, vol. 43, pp. 432 – 435, 2002.

[154] X. Xie, L. Ju, X. Feng, Y. Sun, R. Zhou, K. Liu, S. Fan, Q. Li, and K. Jiang, "Controlled fabrication of high-quality carbon nanoscrolls from monolayer graphene," *Nano Lett.*, vol. 9, no. 7, pp. 2565–2570, 2009.

[155] J. Zheng, H. Liu, B. Wu, Y. Guo, T. Wu, G. Yu, Y. Liu, and D. Zhu, "Production of high-quality carbon nanoscrolls with microwave spark assistance in liquid nitrogen," *Advanced Materials*, no. 21, pp. 2460–2463, 2011.

[156] K. Nakada, M. Fujita, G. Dresselhaus, and M. S. Dresselhaus, "Edge state in graphene ribbons: Nanometer size effect and edge shape dependence," *Physical Review B*, vol. 54, pp. 17 954–17 961, 1996.

[157] S. J. Stuart, A. B. Tutein, and J. A. Harrison, "A reactive potential for hydrocarbons with intermolecular interactions," *J Chem Phys*, vol. 112, no. 14, pp. 6472–6486, 2000.

[158] W. Humphrey, A. Dalke, and K. Schulten, "Vmd: Visual molecular dynamics," *Journal of Molecular Graphics*, vol. 14, pp. 33–38, 1996.

[159] C. Lee, X. Wei, J. W. Kysar, and J. Hone, "Measurement of the elastic properties and intrinsic strength of monolayer graphene," *Science*, vol. 321, pp. 385–388, 2008.

[160] F. Liu, P. Ming, and J. Li, "Ab initio calculation of ideal strength and phonon instability of graphene under tension," *Physical Review B*, vol. 76, p. 064120, 2007.

[161] G. Van Lier, C. Van Alsenoy, V. Van Doren, and P. Geerlings, "Ab initio study of the elastic properties of single-walled carbon nanotubes and graphene," *Chemical Physics Letters*, vol. 326, pp. 181–185, 2000.

[162] E. Konstantinova, S. O. Dantas, and P. M. V. B. Barone, "Electronic and elastic properties of two-dimensional carbon planes," *Physical Review B*, vol. 74, p. 035417, 2006.

[163] S. Gupta, K. Dharamvir, and V. K. Jindal, "Elastic moduli of single-walled carbon nanotubes and their ropes," *Physical Review B*, vol. 72, p. 165428, 2005.

[164] M. Meo and M. Rossi, "Prediction of young's modulus of single wall carbon nanotubes by molecular-mechanics based finite element modelling," *Composites Science and Technology*, vol. 66, pp. 1597–1605, 2006.

[165] P. Qing-Xiang, Z. Yong-Wei, and B. S. Vivek, "Mechanical properties of methyl functionalized graphene: a molecular dynamics study," *Nanotechnology*, vol. 21, p. 115709, 2010.

[166] L. Xu, T.-b. Ma, Y.-z. Hu, and H. Wang, "Molecular dynamics simulation of the interlayer sliding behavior in few-layer graphene," *Carbon*, vol. 50, pp. 1025–1032, 2012.

[167] S. V. Rotkin, I. Zharov, and K. Hess, "Zipping of graphene edge as a mechanism for nt nucleation," *AIP Conference Proceedings*, vol. 591, pp. 454–457, 2001.

[168] Z. Xu and M. J. Buehler, "Geometry controls conformation of graphene sheets: Membranes, ribbons, and scrolls," *ACS Nano*, vol. 4, no. 7, pp. 3869–3876, 2010.

[169] S. Cranford and M. J. Buehler, "Twisted and coiled ultralong multilayer graphene ribbons," *Modelling Simul. Mater. Sci. Eng.*, vol. 19, p. 054003, 2011.

[170] S. V. Hosseini and M. Vahdati, "Modeling the effect of tool edge radius on contact zone in nanomachining," *Computational Materials Science*, vol. 65, pp. 29–36, 2012.

[171] K. Woon and M. Rahman, "The effect of tool edge radius on the chip formation behavior of tool-based micromachining," *The International Journal of Advanced Manufacturing Technology*, vol. 50, pp. 961–977, 2010.

[172] M. Lai, X. Zhang, and F. Fang, "Study on critical rake angle in nanometric cutting," *Appl Phys A-Mater*, vol. 108, pp. 809 – 818, 2012.

[173] N. Ikawa, R. R. Donaldson, R. Komanduri, W. Knig, T. H. Aachen, P. A. McKeown, T. Moriwaki, and I. F. Stowers, "Ultraprecision metal cutting the past, the present and the future," *CIRP Annals - Manufacturing Technology*, vol. 40, pp. 587–594, 1991.

[174] N. Ikawa, S. Shimada, and H. Tanaka, "Minimum thickness of cut in micromachining," *Nanotechnology*, vol. 3, p. 6, 1992.

[175] D. A. Lucca, Y. W. Seo, and R. Komanduri, "Effect of tool edge geometry on energy dissipation in ultraprecision machining," *CIRP Annals - Manufacturing Technology*, vol. 42, pp. 83–86, 1993.

[176] F. Fang, H. Wu, and Y. Liu, "Modeling and experimental investigation on nanometric cutting of monocrystalline silicon," *Int J Mach Tools Manu*, vol. 45, pp. 1681 – 1686, 2005.

[177] C. K. Ng, S. N. Melkote, M. Rahman, and A. Senthil Kumar, "Experimental study of micro- and nano-scale cutting of aluminum 7075-t6," *International Journal of Machine Tools and Manufacture*, vol. 46, pp. 929–936, 2006.

[178] G. Hongyan, Z. Junwei, F. Santiago, and Z. Shiping, "Controlled chatteringa new 'cutting-edge' technology for nanofabrication," *Nanotechnology*, vol. 21, no. 35, p. 355302, 2010.

[179] H. Gu, J. Zhang, S. Faucher, and S. Zhu, "Controlled chattering on pmma and epoxy: Effect of crosslinking and cutting speed on pattern formation," *Polymer*, vol. 52, no. 9, p. 2025, 2010.

[180] T. Li and Z. Zhang, "Carbon nanotube initiated formation of carbon nanoscrolls," *Applied Physics Letters*, vol. 97, no. 8, 2010.

[181] Q. L. Li, X. Xie, L. Ju, X. F. Feng, Y. H. Sun, R. F. Zhou, K. Liu, S. S. Fan, and K. L. Jiang, "Controlled fabrication of high-quality carbon nanoscrolls from monolayer graphene," *Nano Letters*, vol. 9, no. 7, pp. 2565–2570, 2009.

[182] B. V. C. Martins and D. S. Galvo, "Curved graphene nanoribbons: structure and dynamics of carbon nanobelts," *Nanotechnology*, vol. 21, p. 075710, 2010.

[183] X. Shi, Y. Cheng, N. M. Pugno, and H. Gao, "Tunable water channels with carbon nanoscrolls," *Small*, vol. 6, pp. 739–744, 2010.

[184] J. L. Li, Q. S. Peng, G. Z. Bai, and W. Jiang, "Carbon scrolls produced by high energy ball milling of graphite," *Carbon*, vol. 43, no. 13, pp. 2830–2833, 2005.

[185] R. Bacon, "Growth, structure and properties of graphite whiskers," *Journal of Applied Physics*, vol. 31, pp. 283–290, 1960.

[186] H. Shioyama and T. Akita, "A new route to carbon nanotubes," *Carbon*, vol. 41, pp. 179–181, 2003.

[187] M. V. Savoskin, V. N. Mochalin, A. P. Yaroshenko, N. I. Lazareva, T. E. Konstantinova, I. V. Barsukov, and I. G. Prokofiev, "Carbon nanoscrolls produced from acceptor-type graphite intercalation compounds," *Carbon*, vol. 45, no. 14, pp. 2797–2800, 2007.

[188] N. Patra, B. Wang, and P. Kral, "Nanodroplet activated and guided folding of graphene nanostructures," *Nano Letters*, vol. 9, pp. 3766–3771, 2009.

[189] S. F. Braga, V. R. Coluci, S. B. Legoas, R. Giro, D. S. Galvo, and R. H. Baughman, "Structure and dynamics of carbon nanoscrolls," *Nano Letters*, vol. 4, pp. 881–884, 2004.

[190] C. Girit, J. C. Meyer, R. Erni, M. D. Rossell, C. Kisielowski, L. Yang, C.-H. Park, M. F. Crommie, M. L. Cohen, S. G. Louie, and A. Zettl, "Graphene at the edge: stability and dynamics," *Science*, vol. 323, pp. 1705–1708, 2009.

[191] C. D. Reddy, A. Ramasubramaniam, V. B. Shenoy, and Y.-W. Zhang, "Edge elastic properties of defect-free single-layer graphene sheets," *Applied Physics Letters*, vol. 94, pp. 101 904–101 907, 2009.

[192] X. Shi, Y. Cheng, N. M. Pugno, and H. Gao, "A translational nanoactuator based on carbon nanoscrolls on substrates," *Applied Physics Letters*, vol. 96, pp. 053 115–053 119, 2010.

[193] A. Fischer-Cripps, "A review of analysis methods for sub-micron indentation testing," *Vacuum*, vol. 58, no. 4, pp. 569 – 585, 2000.

[194] J. i. Jang, D. Son, Y. H. Lee, Y. Choi, and D. Kwon, "Assessing welding residual stress in a335 p12 steel welds before and after stress-relaxation annealing through instrumented indentation technique," *Scripta Materialia*, vol. 48, no. 6, pp. 743–748, 2003.

[195] A. Warren, Y. Guo, and M. Weaver, "The influence of machining induced residual stress and phase transformation on the measurement of subsurface mechanical behavior using nanoindentation," *Surface and Coatings Technology*, vol. 200, pp. 3459 – 3467, 2006.

[196] K. J. Weinmann, "On wedge indentation and its relationship with incipient plastic deformation in metal cutting," *Journal of Engineering for Industry*, vol. 99, pp. 702–707, 1977.

[197] V. Madhavan and a. T. N. F. S. Chandrasekar, "Machining as a wedge indentation," *Journal of Applied Mechanics*, vol. 67, pp. 128–139, 1998.

[198] B. J. Hockey and R. W. Rice, Eds., *The Science of Ceramic Machining and Surface Finishing II: Proceedings of a Symposium Held at the National Bureau of Standards*. U.S. Department of Commerce, National Bureau of Standards, November 13-15 1979.

[199] I. M. Hutchings, "Deformation of metal surfaces by the oblique impact of square plates," *International Journal of Mechanical Sciences*, vol. 19, pp. 45–52, 1977.

[200] L. Zhang, H. Huang, H. Zhao, Z. Ma, Y. Yang, and X. Hu, "The evolution of machining-induced surface of single-crystal fcc copper via nanoindentation," *Nanoscale Research Letters*, vol. 8, pp. 1–13, 2013.

[201] B. R. Lawn and A. G. Evans, "A model for crack initiation in elastic/plastic indentation fields," *Journal of Materials Science*, vol. 12, pp. 2195–2199, 1977.

[202] F. Daz, C. Mammana, and A. Guidobono, "Modern mechanical engineering," modern mechanical engineering," *Modern Mechanical Engineering*, vol. 2, pp. 143–150, 2012.

[203] A. Richter, R. Ries, R. Smith, M. Henkel, and B. Wolf, "Nanoindentation of diamond, graphite and fullerene films," *Diamond and Related Materials*, vol. 9, pp. 170–184, 2000.

[204] X. Tan, J. Wu, K. Zhang, X. Peng, L. Sun, and J. Zhong, "Nanoindentation models and young's modulus of monolayer graphene: A molecular dynamics study," *Applied Physics Letters*, vol. 102, pp. 071 908–4, 2013.

[205] M. Neek-Amal and F. M. Peeters, "Nanoindentation of a circular sheet of bilayer graphene," *Physical Review B*, vol. 81, p. 235421, 2010.

[206] E. Bucholz, X. Zhao, S. Sinnott, and S. Perry, "Friction and wear of pyrophyllite on the atomic scale," *Tribology Letters*, vol. 46, no. 2, pp. 159–165, 2012.

[207] D. Chrobak, K. Nordlund, and R. Nowak, "Nondislocation origin of gaas nanoindentation pop-in event," *Physical Review Letters*, vol. 98, p. 045502, 2007.

[208] B. Haberl, J. E. Bradby, M. V. Swain, J. S. Williams, and P. Munroe, "Phase transformations induced in relaxed amorphous silicon by indentation at room temperature," *Applied Physics Letters*, vol. 85, pp. 5559–5561, 2004.

[209] S. Ruffell, J. E. Bradby, N. Fujisawa, and J. S. Williams, "Identification of nanoindentation-induced phase changes in silicon by in situ electrical characterization," *J. Appl. Phys.*, vol. 101, p. 083531, 2007.

[210] R. Nowak, D. Chrobak, S. Nagao, D. Vodnick, M. Berg, A. Tukiainen, and M. Pessa, "An electric current spike linked to nanoscale plasticity," *Nat Nano*, vol. 4, pp. 287–291, 2009.

[211] A. C. Lund, A. M. Hodge, and C. A. Schuh, "Incipient plasticity during nanoindentation at elevated temperatures," *Applied Physics Letters*, vol. 85, pp. 1362–1364, 2004.

[212] C. A. Schuh, J. K. Mason, and A. C. Lund, "Quantitative insight into dislocation nucleation from high-temperature nanoindentation experiments," *Nature Mater.*, pp. 617–621, 2005.

[213] C. Bates, F. Dachille, and R. Roy, "High-pressure transitions of germanium and a new high-pressure form of germanium," *Science*, vol. 147, pp. 860 – 862, 1963.

[214] W. Xu, Y. Wang, and T.-Y. Zhang, "Nanoindentation of highly oriented pyrolytic graphite," 11th International Conference on Fracture, 2005.

[215] G. Katagiri, H. Ishida, and A. Ishitani, "Raman spectra of graphite edge planes," *Carbon*, vol. 26, pp. 565 – 571, 1988.

Vita

Buddhika Jayasena was born on 6th November 1981, in the suburbs of Kandy, the hill capital of Sri Lanka. His schooling was at Sri Sumangala College, Kandy. During his schooling he was among the top 5% performers in the class and actively engaged in several extra circular activities. He was a member of under-15 rugby team that won the all island tournament in 1996. In addition to that, he represented both junior and senior prefect boards in his school. He started his tertiary education at University of Peradeniya, Sri Lanka in 2003, and completed his bachelors degree in Production Engineering in 2007. He held number of key positions in production engineering student society during this period. He won the Colombo Dockyard prize for the overall best performance in Production Engineering. He joined Ceylon Oxygen Limited (Sri Lanka) in early 2007 as Project Engineer. One and half years later he started his masters degree in Computer Integrated Manufacturing at Nanyang Technological University, Singapore. His dissertation thesis; An Experimental Investigation of Edge Profiling of Aerospace Alloys was supervised by Dr. Sathayan Subbiah. He won the certificate of excellence for achieving best academic results in Master of Science (2009). Immediately after completion of his M.Sc, he joined the School of Mechanical and Aerospace Engineering at NTU to pursue his PhD under Dr. Sathyan Subbiah. He was awarded a full scholarship during this course of study. His research focuses on mechanical exfoliation of carbon nanosheets. He attended a number of seminars and workshops within and outside NTU and including a full travel grant to participate in the IEAGHG international CCS summer school program in Nottingham, United Kingdom in 2013. During this program he was a member of the group that won the best presentation award in the summer school. He married Erandi Govinna in June 2011.